Lawrence Berkeley Laboratory
UNIVERSITY OF CALIFORNIA

Physics, Computer Science & Mathematics Division

INCLUSIVE LEPTON PRODUCTION IN HADRONIC EVENTS FROM e^+e^- ANNIHILATION AT 29 GeV

M.E. Nelson
(Ph.D. Thesis)

October 1983

Prepared for the U.S. Department of Energy under Contract DE-AC03-76SF00098

DISCLAIMER

LBL-16724

Inclusive Lepton Production in Hadronic Events from e^+e^- Annihilation at 29 GeV

By

Mark Everett Nelson

(Ph.D. Thesis)

Department of Physics
and
Lawrence Berkeley Laboratory

University of California
Berkeley, California 94720

October 1983

This work was supported by the Director, Office of Energy Research, Office of High Energy and Nuclear Physics Division of High Energy Physics of the U. S. Department of Energy under Contract No. DE-AC03-76SF00098.

Inclusive Lepton Production in Hadronic Events from e^+e^- Annihilation at 29 GeV

Mark Everett Nelson

ABSTRACT

We have measured the production rates of prompt electrons and muons in hadronic events from e^+e^- annihilation at 29 GeV. The inclusive rate per hadronic event for leptons with total momenta greater than 2 GeV/c is determined to be $(0.033 \pm 0.003 \pm 0.012)$ for electrons and $(0.037 \pm 0.005 \pm 0.008)$ for muons. We measure the longitudinal and transverse momentum spectra of these leptons. The harder transverse momentum spectrum of leptons from bottom quark decays relative to charm decays allows us to separate the bottom and charm quark contributions to the prompt lepton signal. The longitudinal momentum distributions allow us to study the fragmentation properties of these heavy quarks. For charm quarks we find average semileptonic branching ratios of $(6.4 \pm 1.3 \pm 2.8)\%$ into electrons and $(8.1 \pm 1.6 \pm 1.8)\%$ into muons. For bottom quarks we find average branching ratios of $(12.9 \pm 2.5 \pm 2.0)\%$ into electrons and $(12.2 \pm 5.0 \pm 3.0)\%$ into muons. The fragmentation function for bottom quarks is determined to be peaked at large z with $\langle z \rangle_b \simeq 0.75$.

George H. Trilling

ACKNOWLEDGEMENTS

The success of the Mark II experiment is the result of the dedicated efforts of all the members of the SLAC-LBL-Harvard collaboration and the contributions of the talented engineering and technical staff. The analysis presented in this thesis relies on a well established foundation of hardware and software components which have been developed over many years by many members of the collaboration. Special acknowledgement is due Alain Blondel in this regard for his insightful development of the electron identification algorithm which was central to much of this analysis.

I would like to thank my advisor, George Trilling, for his perceptive guidance and direction. His many comments and suggestions were valuable contributions to all phases of the analysis presented here. Perhaps more important was the implicit direction he provided over the entire course of my graduate career which has shaped much of my current understanding and appreciation of physics.

Finally, I would like to thank my family, my friends, and especially Kathy Collins for unwavering support and encouragement and for the happiness and balance they have brought to my life.

CONTENTS

Chapter 1. INTRODUCTION 1
1.1 Heavy Quark Production in e^+e^- Annihilation 2
1.2 Quark fragmentation 5
1.3 Parameterization of Heavy Quark Fragmentation Functions . . . 6
1.4 Decays of Heavy Hadrons 11
1.5 Analysis Objective and Motivation 23

Chapter 2. THE MARK II DETECTOR 28
2.1 Beam Pipe 28
2.2 Pipe Counter 32
2.3 Trigger Chamber 32
2.4 Vertex Chamber 33
2.5 Main Drift Chamber 33
2.6 Time of Flight System 34
2.7 Magnet Coil 34
2.8 Endcap calorimeters 35
2.9 Small Angle Tagging System 35
2.10 Liquid Argon Calorimeter 37
2.11 Muon System 40
2.12 Event Trigger 42

Chapter 3. ELECTRON IDENTIFICATION 47
3.1 General philosophy 47
3.2 Implementation 51
3.3 Identification efficiency 55
3.4 Hadron misidentification 55
Hadron interactions 57
Track overlap 65
3.5 Electrons from γ conversions and Dalitz decays 71

Chapter 4. MUON IDENTIFICATION 81
4.1 General philosophy 81
4.2 Implementation 82
4.3 Muon identification efficiency 87
4.4 Hadron misidentification probability 92
Muon system noise 92
Hadron punchthrough 95
Hadron decay in flight 111

Chapter 5. ANALYSIS PROCEDURE 120
5.1 Hadronic Event Selection 120
5.2 Event backgrounds 120

$e^+e^- \rightarrow \tau^+\tau^-$ 121
$e^+e^- \rightarrow e^+e^-$ + hadrons 122
Beam-gas events 129
5.3 Electron results 130
Raw signal 130
Misidentified hadron subtraction 130
Pair subtraction 130
Net signal 132
5.4 Muon results 133
Raw signal 133
Hadron punchthrough subtraction 133
π and K decay subtraction 133
Net signal 135

Chapter 6. PROMPT LEPTON CROSS SECTIONS 136
6.1 Fiducial acceptance 136
6.2 Identification Efficiency 138
6.3 Inclusive Cross Sections 138

Chapter 7. PROPERTIES OF HEAVY QUARKS 146
7.1 Fit to the lepton $p,p_\perp$ spectra 146
Monte Carlo simulation 146
Semileptonic decays in the Monte Carlo 147
Parameterization of the fit 151
7.2 Fit results 154
7.3 Quality of Fits 156
7.4 Composition of the lepton signal 159
7.5 Fit using another parameterization of D_Q^H 164
7.6 Conclusions 165

Appendix A: Monte Carlo $p,p_\perp$ Distributions 170

Appendix B: Detailed Results of Fits 178

References 190

FIGURES

1.1 Hadronic event production in e^+e^- annihilation. 3
1.2 Hadronization via quark fragmentation. 8
1.3 Fragmentation functions as parameterized by Eq. (1.1). 9
1.4 D* production cross sections in e^+e^- annihilation 10
1.5 Charged current weak decays 14
1.6 Spectator diagrams for charm and bottom decays 15
1.7 Rearrangement of color flow in the spectator diagram. 19
1.8 Non-spectator diagrams for D^0, D^+, and F^+ decays. 22
1.9 Transverse lepton momentum distributions 25

2.1 A cross sectional view of the MARK II detector at PEP. 29
2.2 An isometric view of the MARK II detector at PEP 30
2.3 A view of the MARK II detector showing the SAT system. 36
2.4 Ganging pattern in LA calorimeter modules 39
2.5 A cross sectional view of a muon proportional tube module 41
2.6 Definitions of hardware track processor curvature roads. 45

3.1 Identification efficiency vs. misidentification probability . . . 53
3.2 Typical E_{min}/p distributions 54
3.3 Electron identification efficiency vs. momentum 56
3.4 Pion momentum spectrum from $\psi \to 2(\pi^+\pi^-)\pi^0$ 58
3.5 E_{min}/p for pions from $\psi \to 2(\pi^+\pi^-)\pi^0$ 59
3.6 E_{min}/p for pions from the test beam data 62
3.7 Pion misidentification vs. momentum 63
3.8 Definitions of pair finding variables 74
3.9 Distributions of pair finding variables 75
3.10 Radius of conversion (R_{xy}) 77

4.1 MUSTAT distribution for muon fiducial volume tracks 84
4.2 Measured deviation from extrapolated position divided by sigma . 86
4.3 MUSTAT distribution for muons from $e^+e^- \to \mu^+\mu^-$ 89
4.4 MUSTAT distribution from random background. 93
4.5 MUSTAT distribution for "flipped" tracks 94
4.6 Pion range data from the SLAC 20 GeV spectrometer 96
4.7 Fraction of incident pions surviving 98
4.8 Pions from K_s^0 decay. (a) momentum (b) MUSTAT. 104
4.9 Pions from $\tau \to 3\pi\nu$ decay. (a) momentum (b) MUSTAT. 105
4.10 Hadron punchthrough probabilities in several momentum bins . . 108
4.11 Pion and Kaon μ_2 decay probabilities 113
4.12 p_μ vs. p_{had} in π and K μ_2 decays 115
4.13 Decay angle times p_{had} for π and K μ_2 decays 116
4.14 Charged particle spectra for (a) data and (b) Monte Carlo . . 118

5.1 Order α^4 contributions to $e^+e^- \to e^+e^-$ + hadrons 123
5.2 Large Q^2 two-photon background event. 126
5.3 Inelastic Compton scatter background event. 127
5.4 Comparison of of (a) prompt and (b) background momenta 128

6.1 Fiducial acceptance for electrons and muons. 137
6.2 Differential total momentum cross sections. 143
6.3 Differential transverse momentum cross sections. 144

7.1 Comparison of DELCO data and MARK II Monte Carlo. 148
7.2 Comparison of CLEO data and MARK II Monte Carlo. 149
7.3 Prompt electron momentum spectra. 162
7.4 Prompt muon momentum spectra. 163
7.5 Comparison of charm and bottom fragmentation functions. 166

TABLES

1.1 Charm and bottom mesons and baryons 4
1.2 Heavy hadron semileptonic branching ratios 16
1.3 Typical $(p,p_\perp)$ table. 27

2.1 MARK II detector configurations. 31
2.2 Muon system configuration 40

3.1 Values of W_{shower} and W_{gang} in units of strip widths 52
3.2 Prompt electron detection efficiency 57
3.3 Pion misidentification probabilities. 61
3.4 Misidentification probability estimates including overlap. . . . 70
3.5 Overall Pion misidentification probability 70
3.6 Hadrons (non-electrons) in electron fiducial volume. 71
3.7 Expected electron background from misidentified hadrons. 71
3.8 Electrons belonging to real pairs. 76
3.9 Electrons removed with less than 2 VC cells. 79
3.10 Expected background electrons from unidentified pairs. 79

4.1 Muon identification efficiency 91
4.2 Determination of hadron punchthrough probabilities 101
4.3 Measured punchthrough probabilities from various sources. . . . 107
4.4 Calculation of hadron punchthrough probabilities 110
4.5 Hadrons in muon fiducial volume 112
4.6 Hadron punchthrough probabilities 112
4.7 Background to muon signal from hadron punchthrough 112
4.8 Background to muon signal from decays in flight. 119

5.1 Raw prompt electron signal. 131
5.2 Expected electron background from misidentified hadrons. . . . 131
5.3 Expected background from non-prompt electrons. 131
5.4 Net prompt electron signal. 132
5.5 Raw prompt muon signal. 134
5.6 Background to muon signal from hadron punchthrough 134
5.7 Expected background contribution from π and K μ_2 decays. . . . 134
5.8 Net prompt muon signal. 135

6.1 Prompt electron detection efficiency. 139
6.2 Prompt muon identification efficiency. 139
6.3 Efficiency corrected prompt electron signal. 140
6.4 Efficiency corrected prompt muon signal. 141
6.5 Prompt Lepton rates per hadronic event. 145
6.6 Prompt Lepton cross sections. 145

7.1 Results of the fit 154
7.2 Electron fit - Fit prediction vs. Observed signal 157
7.3 Muon fit - Fit prediction vs. Observed signal 158
7.4 Background and heavy quark contributions 159

7.5 Electron fit - Contributions to the observed signal. 160
7.6 Muon fit - Contributions to the observed signal. 161
7.7 Results of a fit using $D(z) \propto z^{\alpha}(1-z)$ 164
7.8 Results of the fit 165

A.1 Electron $p,p_{\perp}$ distributions for $c \rightarrow eX$. 172
A.2 Electron $p,p_{\perp}$ distributions for $b \rightarrow eX$. 173
A.3 Electron $p,p_{\perp}$ distributions for $b \rightarrow c \rightarrow eX$. 174
A.4 Muon $p,p_{\perp}$ distributions for $c \rightarrow \mu X$. 175
A.5 Muon $p,p_{\perp}$ distributions for $b \rightarrow \mu X$. 176
A.6 Muon $p,p_{\perp}$ distributions for $b \rightarrow c \rightarrow \mu X$. 177

B.1 Electron fit - nominal results 178
B.2 Muon fit - nominal results 179
B.3 Electron fit - systematic check - $z^{\alpha}(1-z)$ parameterization . . 180
B.4 Muon fit - systematic check - $z^{\alpha}(1-z)$ parameterization 181
B.5 Electron fit - systematic check - 50% more pion background . . 182
B.6 Muon fit - systematic check - 50% more pion background 183
B.7 Electron fit - systematic check - 50% less pion background . . 184
B.8 Muon fit - systematic check - 50% less pion background 185
B.9 Electron fit - systematic check - harder charm fragmentation . 186
B.10 Muon fit - systematic check - harder charm fragmentation . . . 187
B.11 Electron fit - systematic check - softer charm fragmentation . 188
B.12 Muon fit - systematic check - softer charm fragmentation . . . 189

1. INTRODUCTION

The discoveries of the J/ψ(3100) in 1974 [1] and the Υ(9460) in 1977 [2] marked the beginnings of the experimental investigations of particles which are interpreted as containing charm (c) and bottom (b) quarks. The J/ψ is interpreted as a bound state of a charm quark and its antiquark ($c\bar{c}$) and the Υ is assumed to be a bound state of bottom and its antiquark ($b\bar{b}$). The J/ψ and Υ have net charm and bottom quantum numbers of zero since they contain both a quark and an antiquark of the same flavor. Thus they can decay via the electromagnetic and strong interactions which conserve the flavor quantum number. A full understanding of the properties of c and b quarks requires the investigation of their weak decay properties as well. This can be accomplished through the study of particles which contain only one c or b quark and which therefore have nonzero c or b quantum numbers. The lowest lying mass states of these charm and bottom particles can only decay via the flavor changing weak interaction.

Since the discoveries of the J/ψ and Υ, several particles with nonzero charm or bottom quantum numbers have been observed. Table 1.1 lists these particles, along with some which have not yet been observed, but which are predicted by the standard quark model. These charm and bottom particles can be produced in electron-positron annihilations at high energies. In this thesis we will investigate some of the production and decay properties of such particles by studying the leptons which are produced in semileptonic weak decays.

In this chapter we begin by discussing the production mechanism for c and b quarks (heavy quarks) in e^+e^- annihilations. We then discuss

the phenomenology of the hadronization process, in which these initial heavy quarks produce observable final state hadrons. Next we explore the semileptonic weak decay process, in which heavy hadrons decay into final states containing leptons. We end this introductory chapter with a discussion of the experimental method we will use to study these processes. In Chapter 2 we will discuss the details of the Mark II detector. Chapters 3 and 4 will describe the identification algorithms used to find electron and muon candidates and will discuss the backgrounds arising from the more numerous pions, kaons and protons in hadronic events. Chapter 5 will detail the analysis procedure which leads to the determination of the inclusive lepton rates and cross sections. These rates and cross sections will be presented in Chapter 6. In Chapter 7 we will interpret these measured lepton cross sections in terms of the production and decay properties of c and b quarks.

1.1 Heavy Quark Production in e^+e^- Annihilation

Hadronic event production in e^+e^- annihilations is mediated by the quark pair production diagram shown in Figure 1.1. At a center of mass energy of 29 GeV, five quark flavors can be produced. These flavors are denoted u (up), d (down), s (strange), c (charm), and b (bottom). A sixth flavor t (top) is also predicted by the standard model but its mass is apparently too large for it to be pair produced in e^+e^- annihilations at presently available center of mass energies. Since quarks are not observed as free particles, the definition of a quark mass is somewhat model dependent, especially for light quarks. Models which predict "constituent quark masses" typically predict the following magnitudes: $m_u = m_d \simeq 0.3$ GeV/c^2, $m_s \simeq 0.5$ GeV/c^2, $m_c \simeq 1.7$ GeV/c^2, m_b

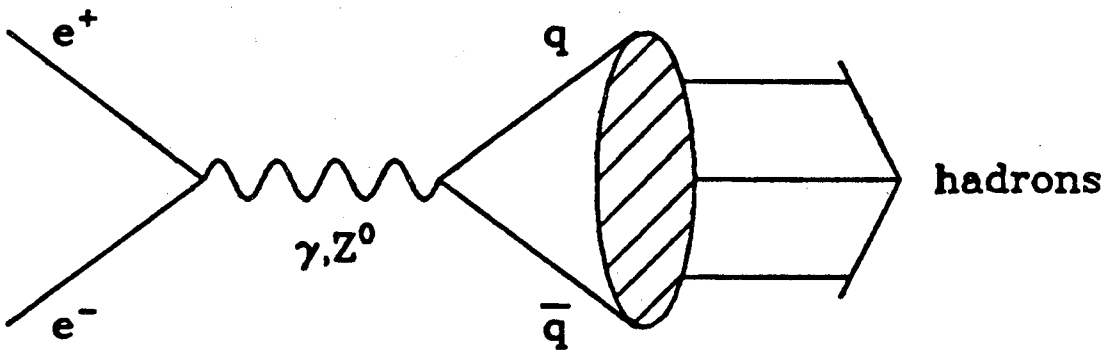

Figure 1.1: Hadronic event production in e^+e^- annihilation.

Name	Quark Content	J^p	Mass (MeV/c2)
	C H A R M E D	M E S O N S	
D^+	$(c\bar{d})$	0^-	1869
D^{*+}	$(c\bar{d})$	1^-	2010
D^0	$(c\bar{u})$	0^-	1865
D^{*0}	$(c\bar{u})$	1^-	2010
F^+	$(c\bar{s})$	0^-	1970
F^{*+}	$(c\bar{s})$	1^-	
	C H A R M E D	B A R Y O N S	
Λ_c^+	$c(ud)_a$	$\frac{1}{2}^+$	2282
Σ_c^{++}	$c(uu)$	$\frac{1}{2}^+$	2450
Σ_c^+	$c(ud)_s$	$\frac{1}{2}^+$	2450
Σ_c^0	$c(dd)$	$\frac{1}{2}^+$	
	B O T T O M	M E S O N S	
B_u^-	$(b\bar{u})$	0^-	5272
B_u^{*-}	$(b\bar{u})$	1^-	
B_d^0	$(b\bar{d})$	0^-	5276
B_d^{*0}	$(b\bar{d})$	1^-	
B_s^0	$(b\bar{s})$	0^-	
B_s^{*0}	$(b\bar{s})$	1^-	

Table 1.1: Charm and bottom mesons and baryons
Particles which have no entry in the "Mass" column have not yet been observed, but should be produced with rates comparable to the observed states.

$\simeq$ 5.0 GeV/c^2. The u, d, and s quarks are referred to as light quarks while the more massive c, and b quarks are considered heavy quarks.

The cross section for producing a pair of point-like spin $\frac{1}{2}$ particles via the single intermediate virtual photon of Figure 1.1 is:

$$\sigma = \frac{4\pi\alpha^2 q^2}{3s} \beta \left[\frac{3-\beta^2}{2} \right] C$$

Here q is the magnitude of the charge of the produced particles, β is their velocity, s is the square of the center of mass energy, and C is a color factor. C = 1 for charged lepton-antilepton pairs (e^+e^-, $\mu^+\mu^-$, and $\tau^+\tau^-$) and C = 3 for quark-antiquark pairs ($q\bar{q}$). At energies sufficiently above the production thresholds ($\beta \simeq 1$), quark pairs of different flavors are thus produced in proportion to their charge squared. At 29 GeV we expect the charge -1/3 quarks (d,s, and b) each to contribute 1/11 to the total quark pair production cross section while the charge +2/3 quarks (u and c) should each contribute 4/11 to the total. These quarks do not appear in the final state as free particles, but instead appear in bound states as mesons (by combining with an antiquark) or baryons (by combining with two other quarks). The process in which these quarks are transformed into observable particles is called quark fragmentation.

1.2 Quark fragmentation

One way to characterize the quark fragmentation process is to define a phenomenological fragmentation function $D_q^H(z)$. This function is defined to be the probability that a quark q with energy E_q will result in a hadron H of energy zE_q via the fragmentation process. Here the variable z, $0<z<1$, is the fractional energy carried by the hadron.

Many models for the fragmentation process, such as the Feynman-Field [3] or color potential [4] model, involve the production of secondary quark-antiquark pairs as illustrated in Figure 1.2. In these models, the primary and secondary quarks combine to form final state hadrons. In such models, the probability for pair producing secondary heavy quarks is suppressed relative to light quarks. Thus heavy quarks are assumed to be either primary quarks which carry the energy of the incident beam or to be the weak decay products of heavier quarks (e.g. b→c decay).

Although the details of the actual fragmentation process may involve complicated dynamical effects, simple kinematical considerations suggest that, as quark masses increase, hadrons containing the heavy quark should carry an increasing fraction of its energy [5]. There is at present experimental evidence that the charm quark to charmed meson fragmentation does lead to a harder momentum spectrum than is the case for the light quark fragmentation [6-8].

1.3 Parameterization of Heavy Quark Fragmentation Functions

Peterson et al. [9] have proposed a parameterization of the heavy quark fragmentation function which is based on simple kinematic and quantum mechanical arguments. Their derivation is outlined below. Consider a process such as that shown in Figure 1.2(b), in which a heavy quark Q fragments into a heavy hadron H = ($Q\bar{q}$) and light quark q. The initial heavy quark momentum is p, and the final state momenta are zp and (1-z)p for the heavy hadron and light quark respectively. There is an energy transfer in the process $\Delta E = E_Q - E_H - E_q$, which is in general non-zero. The quantum mechanical amplitude for this process, ignoring

dynamical vertex functions is proportional to ΔE^{-1}. The energies for each of the three particles in Figure 1.2(b) are:

$$E_Q = \sqrt{m_Q^2 + p^2} \simeq p + m_Q^2/2p$$

$$E_H = \sqrt{m_Q^2 + z^2p^2} \simeq zp + m_Q^2/2zp$$

$$E_q = \sqrt{m_q^2 + (1-z)^2p^2} \simeq (1-z)p + m_q^2/2(1-z)p$$

Thus the energy transfer ΔE is given by:

$$\Delta E = E_Q - E_H - E_q \simeq (m_Q^2/2p)[1 - 1/z - \epsilon_Q/(1-z)]$$

where ϵ_Q is m_q^2/m_Q^2 and where we have assumed that $m_H = m_Q$. Since the amplitude goes as ΔE^{-1}, the transition probability is proportional to ΔE^{-2}. If we ignore the small transverse momentum components (typically 300 MeV/c w.r.t the direction of Q) then the transition probability is also proportional to the longitudinal phase space factor $dp_{\parallel}/E$ (as opposed to d^3p/E for three-dimensional phase space). Since $dp/E = \beta dp/p \simeq dz/z$ for $\beta \simeq 1$, the factor of $1/z$ is included and the following ansatz for the fragmention function is proposed:

$$D_Q^H(z) \propto \frac{1}{z(\Delta E)^2} \propto \frac{1}{z[1 - 1/z - \epsilon_Q/(1-z)]^2} \qquad (1.1)$$

Figure 1.3 shows the resulting shapes of the fragmentation function for several different values of ϵ_Q. Note that the average z of the distribution increases as ϵ_Q is reduced. It has been shown by Schlatter [10] that the existing experimental data on charm quark fragmentation can be satisfactorily described by Eq. (1.1) with $\epsilon_Q \simeq 0.25$. This value of ϵ_Q results in an average $z \simeq 0.55$. Figure 1.4 shows the D^* production cross section in e^+e^- annihilation as measured by several experiments including the Mark II. The solid curve is Eq. (1.1) with $\epsilon_Q = 0.25$. A similar analysis by Kleinknecht and Renk [11] finds a best

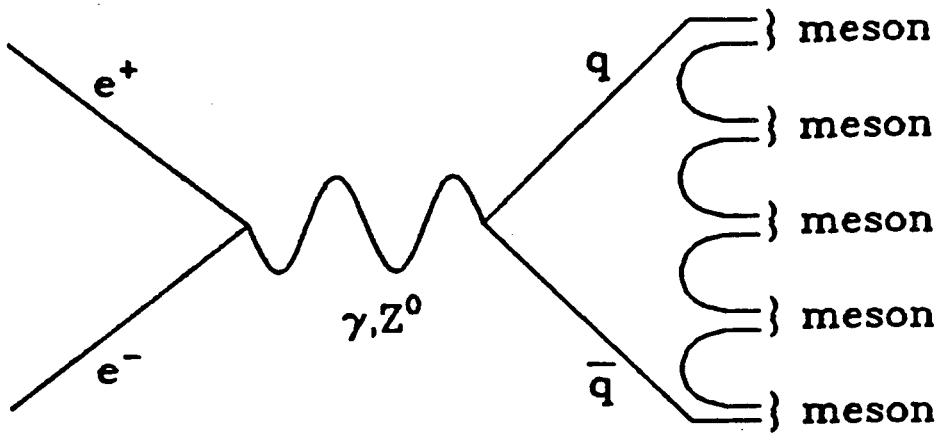

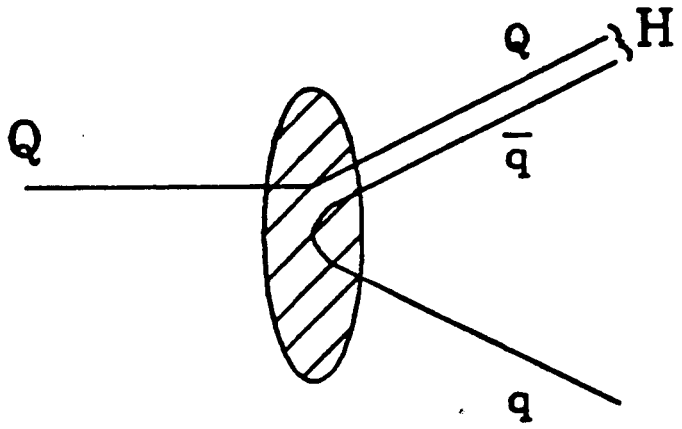

Figure 1.2: Hadronization via quark fragmentation. (a) Hadronization via secondary production of quark-antiquark pairs. (b) Fragmentation of a heavy quark Q into heavy hadron H.

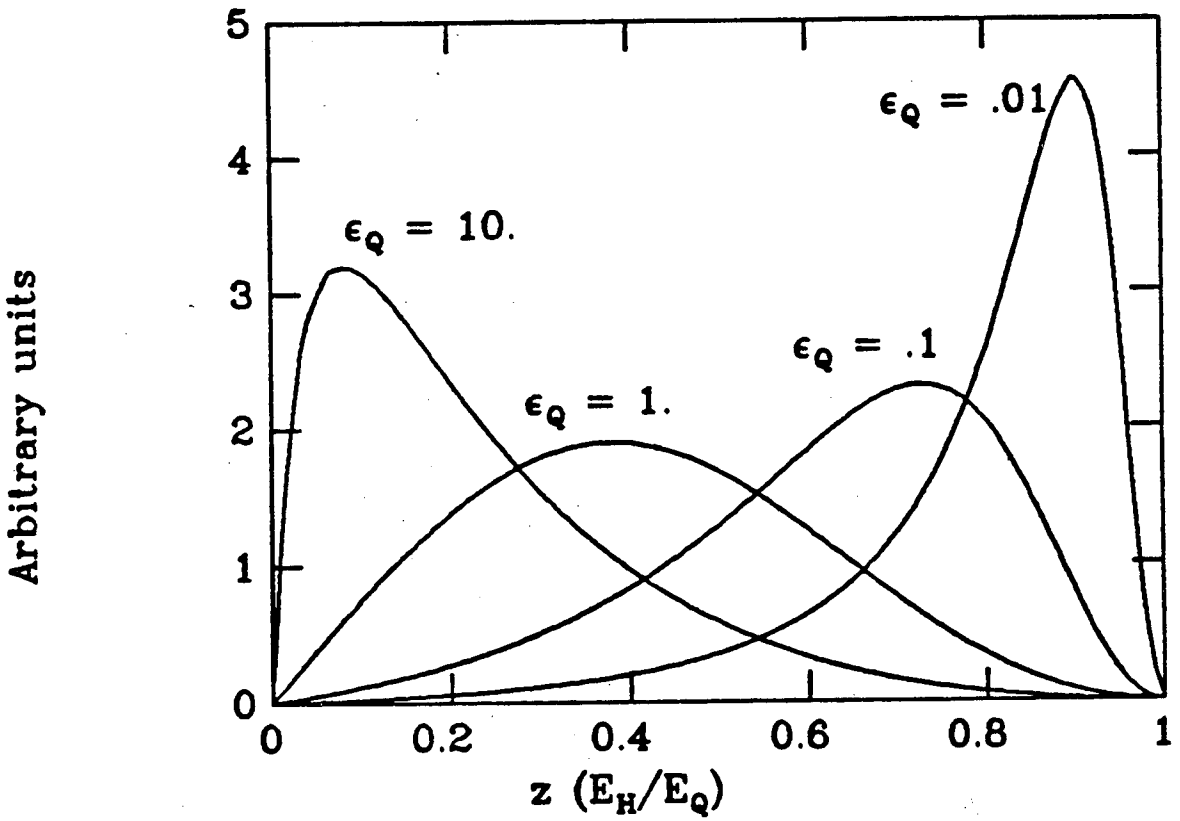

Figure 1.3: Fragmentation functions as parameterized by Eq. (1.1).
The curve with ϵ_Q = 10.00 has $\langle z \rangle$ = 0.23.
" " " " 1.00 " 0.41.
" " " " 0.10 " 0.63.
" " " " 0.01 " 0.80.

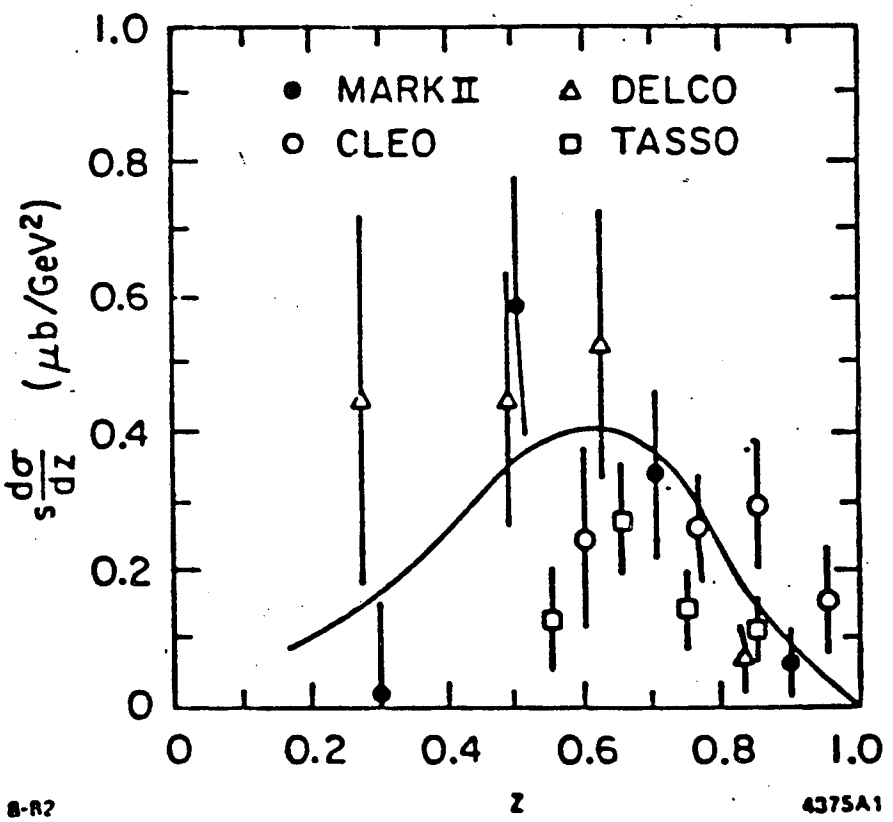

Figure 1.4: D* production cross sections in e^+e^- annihilation
This figure was taken from Ref. [10]. The solid curve is Eq. (1.1) with $\epsilon_Q = 0.25$.

value of $\epsilon_Q \simeq 0.11$ resulting in an average $z \simeq 0.62$. The data from the Mark II D* analysis [6] is consistent with both fits but favors the $\epsilon_Q \simeq 0.25$ value.

1.4 Decays of Heavy Hadrons

Thus far we have described the process that leads from the initial annihilation of an electron-positron pair, through the intermediate pair production of heavy quarks, to the production of observable heavy hadrons which carry non-zero charm or bottom quantum numbers. These heavy hadrons are not stable. The lowest lying mass states decay via the weak interaction with lifetimes that are typically in the range of 10^{-13} to 10^{-12} sec [12]. Even if these heavy hadrons carried the full original quark energy (14.5 GeV in our experiment), they would typically travel less than two millimeters in our detector before decaying into more stable particles.

The decays of these particles can be understood in terms of the standard Weinberg-Salam SU(2) × U(1) gauge theory of weak interactions [13] combined with the Kobayashi-Maskawa (K-M) six quark model [14]. In this model, quarks and leptons are grouped into doublets as follows:

$$\begin{pmatrix}\nu_e\\ e\end{pmatrix}\ \begin{pmatrix}\nu_\mu\\ \mu\end{pmatrix}\ \begin{pmatrix}\nu_\tau\\ \tau\end{pmatrix}\ \begin{pmatrix}u\\ d'\end{pmatrix}\ \begin{pmatrix}c\\ s'\end{pmatrix}\ \begin{pmatrix}t\\ b'\end{pmatrix}$$

where d′, s′, and b′ are mixtures of the d, s, and b quarks. This mixing can be described by a unitary matrix U as follows:

$$\begin{pmatrix}d'\\ s'\\ b'\end{pmatrix} = U \begin{pmatrix}d\\ s\\ b\end{pmatrix}$$

The charged weak current which couples leptons to their neutrinos and charge -1/3 quarks to the charge 2/3 quarks is written as:

$$J_c^{\alpha} = (\bar{\nu}_e\ \bar{\nu}_\mu\ \bar{\nu}_\tau)\left[\gamma^{\alpha}\frac{(1-\gamma_5)}{2}\right]\begin{pmatrix} e^- \\ \mu^- \\ \tau^- \end{pmatrix}$$

$$+ (\bar{u}\ \ \bar{c}\ \ \bar{t}\ )\left[\gamma^{\alpha}\frac{(1-\gamma_5)}{2}\right]\begin{pmatrix} d' \\ s' \\ b' \end{pmatrix}$$

The mixing matrix U has been parameterized by Kobayashi-Maskawa:

$$U = \begin{pmatrix} c_1 & s_1c_3 & s_1s_3 \\ -s_1c_2 & c_1c_2c_3 - s_2s_3e^{i\delta} & c_1c_2s_3 + s_2c_3e^{i\delta} \\ -s_1s_2 & c_1s_2c_3 + c_2s_3e^{i\delta} & c_2s_2s_3 - c_2c_3e^{i\delta} \end{pmatrix}$$

where $c_i \equiv \cos\theta_i$ and $s_i \equiv \sin\theta_i$. Thus there are four angles $\theta_1, \theta_2, \theta_3$ and δ which completely describe the mixing in this six quark model. In the limit of $\theta_2 = \theta_3 = \delta = 0$, this reduces to the following matrix where θ_c is the more familiar Cabibbo angle of the four quark Glashow-Iliopoulos-Maiani (GIM) model [15]:

$$U = \begin{pmatrix} \cos\theta_c & \sin\theta_c & 0 \\ -\sin\theta_c & \cos\theta_c & 0 \\ 0 & 0 & -1 \end{pmatrix}$$

In this limit, the b quark does not mix with the d and s quarks. If this were the case, the b quark would only couple to the more massive t quark via the charged weak current J_c. Since the decay of b into t would be kinematically forbidden, the b quark would be stable. Recent results on b decay from the CESR storage ring at Cornell indicate that this is not the case [16]. They find the relative rate for b→c relative to b→u (the two kinematically allowed couplings) [12]:

$$\frac{\Gamma(b\to u)}{\Gamma(b\to c)} < 0.10\ (90\%\ C.L.)$$

There is also information on charm decays from the Mark II at SPEAR [17] which yield:

$$\frac{\Gamma(c\to d)}{\Gamma(c\to s)} \simeq .05 - .10$$

These charm decay results are about the same as would be expected from the four quark model which predicts this ratio to be $\tan^2\theta_c \simeq 0.05$. These results can be combined to define a preferred decay hierarchy for flavor changing weak decays, namely:

$$b \to c \to s \to u$$

In the following discussion, decays which follow the above sequence will be called "K-M favored" and those which do not (e.g. b→u or c→d) will be referred to as "K-M suppressed".

In the simplest decay model for charm and bottom hadrons, the weak decays proceed via the diagram in Figure 1.5(a). In this figure, the charged weak current J_c is mediated by a charged weak vector boson $W^{\pm}$. This diagram is called a "spectator" diagram since the light quark $\bar{q}$ is a spectator in the sense that it does not directly participate in the weak decay process. In this spectator model, the heavy quark is treated as a free particle and the decay rate can be calculated in analogy to the muon decay process shown in Figure 1.5(b).

The spectator diagrams for charm and bottom meson decay are shown explicitly in Figures 1.6 (a) and (b). The product of the color factors (1 for leptons, 3 for quarks) and the phase space factors are shown for each decay mode. A simple calculation based on these factors predicts semileptonic branching ratios of ≃ 20% (1/5) for $c\to X\ell\bar{\nu}_\ell$ and ≃ 17% (1/5.8) for $b\to X\ell\bar{\nu}_\ell$ where ℓ = e or μ. The spectator model also predicts

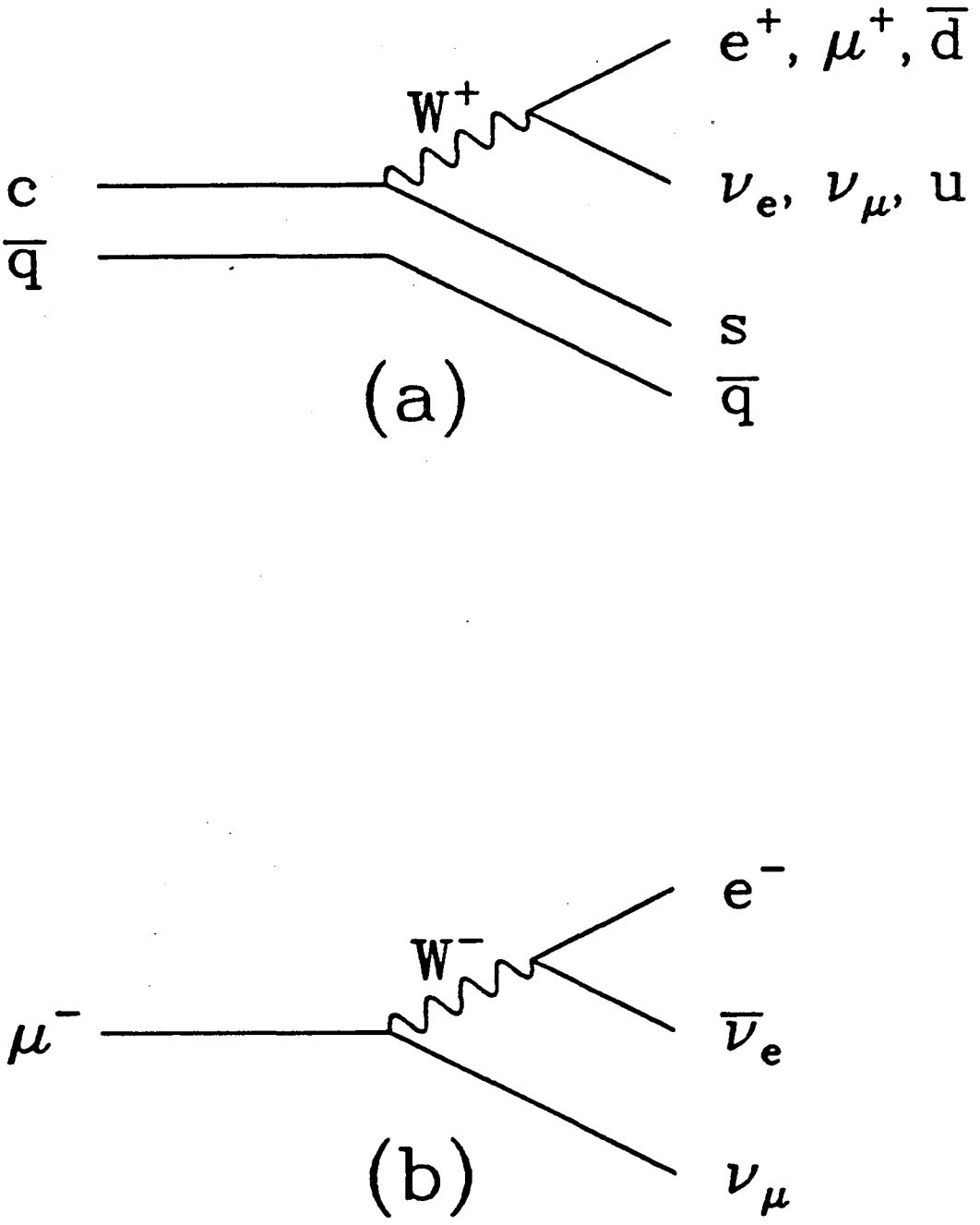

Figure 1.5: Charged current weak decays
(a)Spectator diagram for heavy hadron decays. (b) Diagram for muon decay.

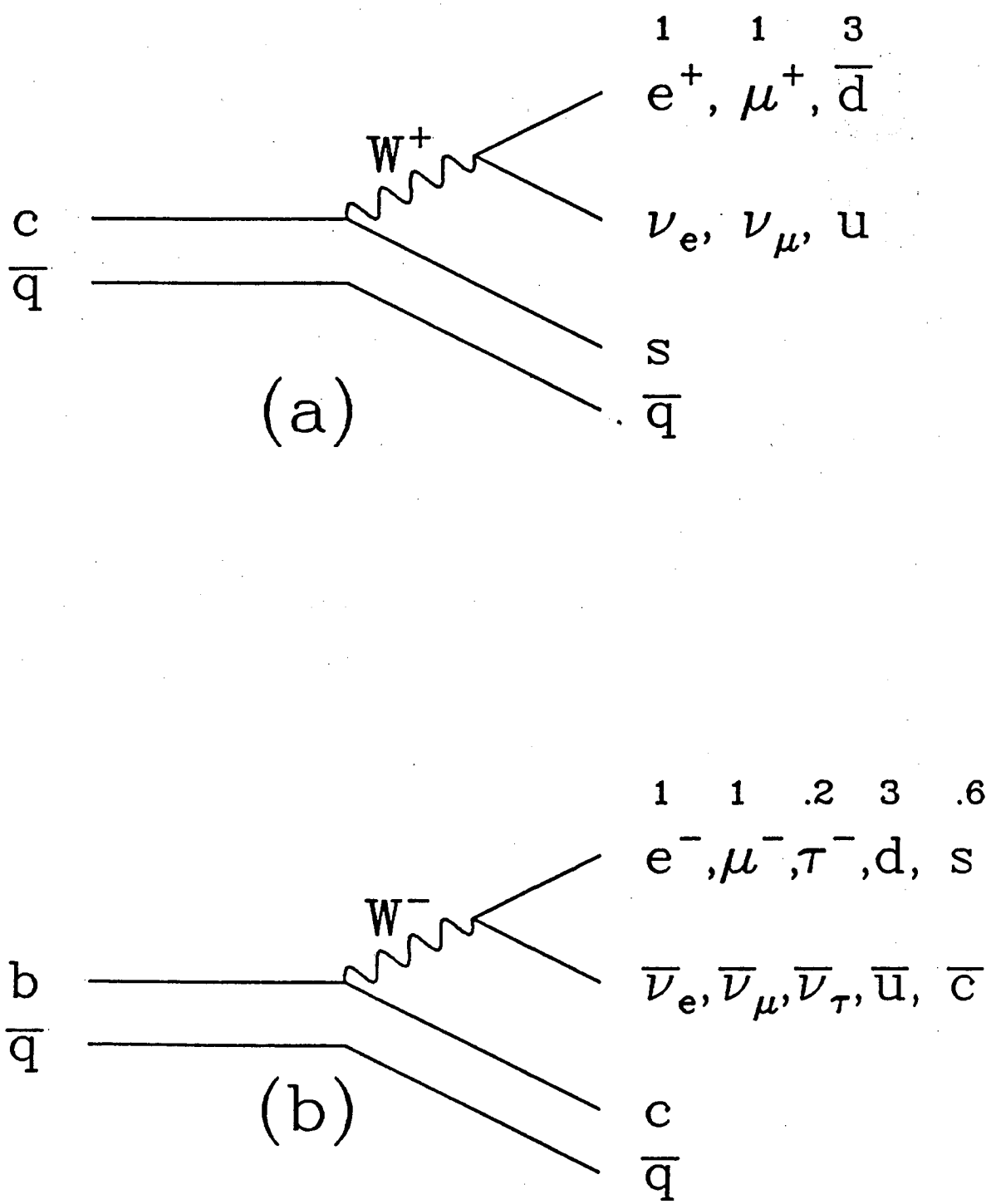

Figure 1.6: Spectator diagrams for charm and bottom decays (a) Charm meson decay. (b) Bottom meson decay. The numbers above the W decay products represent the product of the color factor and phase space factors for each mode.

Heavy Hadron Composition	E_{cm} (GeV)	Mode (e or μ)	Branching Ratio (%)	Reference
A V E R A G E C H A R M R E S U L T S				
56% D^0; 44% D^+	3.77	e	8.0 ± 1.5	DELCO [18]
56% D^0; 44% D^+	3.77	e	7.2 ± 2.8	LGW [19]
D^0, D^+, F^+	3.99–4.08	e	8.0 ± 3.0	DASP [20]
$D^0, D^+, F^+, \Lambda_c^+$	3.9–7.4	e	8.2 ± 1.9	LGW [21]
I N D I V I D U A L C H A R M R E S U L T S				
D^+	3.77	e	16.8 ± 6.4	MARKII [17]
D^0			5.5 ± 3.7	
D^+	3.77	e	22.0 + 4.4 − 2.2	DELCO [22]
D^0			<4 (95% C.L.)	
Λ_c^+	4.5–6.8	e	4.5 ± 1.7	MARKII [23]
A V E R A G E B O T T O M R E S U L T S				
50% B^0; 50% B^+	10.55	e	12.7 ± 1.7 ± 1.3	CLEO [24]
50% B^0; 50% B^+	10.55	μ	12.4 ± 1.7 ± 3.1	CLEO [24]
50% B^0; 50% B^+	10.55	e	13.6 ± 2.5 ± 3.0	CUSB [25]

Table 1.2: Heavy hadron semileptonic branching ratios

equal semileptonic branching ratios for D^+ ($c\bar{d}$) and D^0 ($c\bar{u}$) since the light quark does not take part in the decay process. These predictions, however, do not agree very well with the experimental results summarized in Table 1.2. Here we see that the D^+ and D^0 semi-electronic branching ratios are not equal. The D^+ branching ratio seems to be larger than that for D^0 by a factor of 3-5. In addition, the average charm branching ratios are in the 7-10% range, whereas the simple spectator model predicts $\simeq$ 20%. There is no experimental information on the individual B^0 and B^+ branching ratios, but the average results of 12-13% are somewhat lower than the $\simeq$ 17% predicted by the simple spectator model.

The failure of the simple spectator model to correctly predict the charm semileptonic branching ratios has prompted many theoretical extensions and alternative approaches. The current theoretical situation for charm decays and the extension to bottom decays has been reviewed by Leveille [26]. The major points will be outlined below.

There are basically two improvements which can be made to the simple model: (1) strong interaction effects can be included in the spectator diagrams and (2) non-spectator diagrams can be included. There are two types of strong interaction corrections which can be made. The first type involves the radiation of gluons by the quarks, in analogy to the radiation of photons in muon decay. The corrections for single gluon radiation in semileptonic charm decays have been calculated by Cabibbo and Maiani, and Cabibbo, Corbo, and Maiani [27]. The uncorrected rate Γ_0 for semileptonic charm decay (neglecting phase space corrections and strong interaction corrections) is related to the rate for muon decay by:

$$\Gamma_0 = \left(\frac{M_c}{M_\mu}\right)^5 \Gamma(\mu \to e\nu\bar{\nu}) = \frac{G^2 M_c^5}{192\ \pi^3}$$

The corrected rate Γ can be expressed in terms of the uncorrected rate Γ_0 as:

$$\Gamma/\Gamma_0 = g(\epsilon)\left[1 - \frac{2\alpha_s}{3\pi} f(\epsilon)\right]$$

where $g(\epsilon)$ is a phase space factor

$$g(\epsilon)=1 - 8\epsilon^2 - 24\epsilon^4 \ln(\epsilon) + 8\epsilon^6 - \epsilon^8$$

$f(\epsilon)$ is the strong correction coefficient, $\epsilon = M_s/M_c$ is the ratio of the strange and charm quark masses, and α_s is the strong coupling constant evaluated at the heavy quark mass,

$$\alpha_s(M_Q) = \frac{12\pi}{(33-2N_f)\ \ln(M_Q^2/\Lambda^2)}$$

with M_Q the heavy quark mass, Λ the QCD scale parameter ($\simeq$ 0.3 GeV) and N_f the number of quark flavors that can be produced. The function $f(\epsilon)$ is a smoothly decreasing function of ϵ which varies between $\simeq$ 3.62 at ϵ=0 and 1.5 at ϵ=1. α_s decreases as M_Q increases. The total corrections to Γ_0 are on the order of 50% for charm decay and 15% for b decay. Although this correction is quite large for charm decay, the effect on the charm semileptonic branching ratio not as substantial because most of the corrections in the semileptonic decays exactly cancel with similar corrections in the nonleptonic decays. The net effect however is to slightly decrease the semileptonic branching ratio.

There is a second type of strong corrections to the non-leptonic spectator diagrams which can be sizable. These corrections are generally termed "short distance enhancements" [28]. For the simple

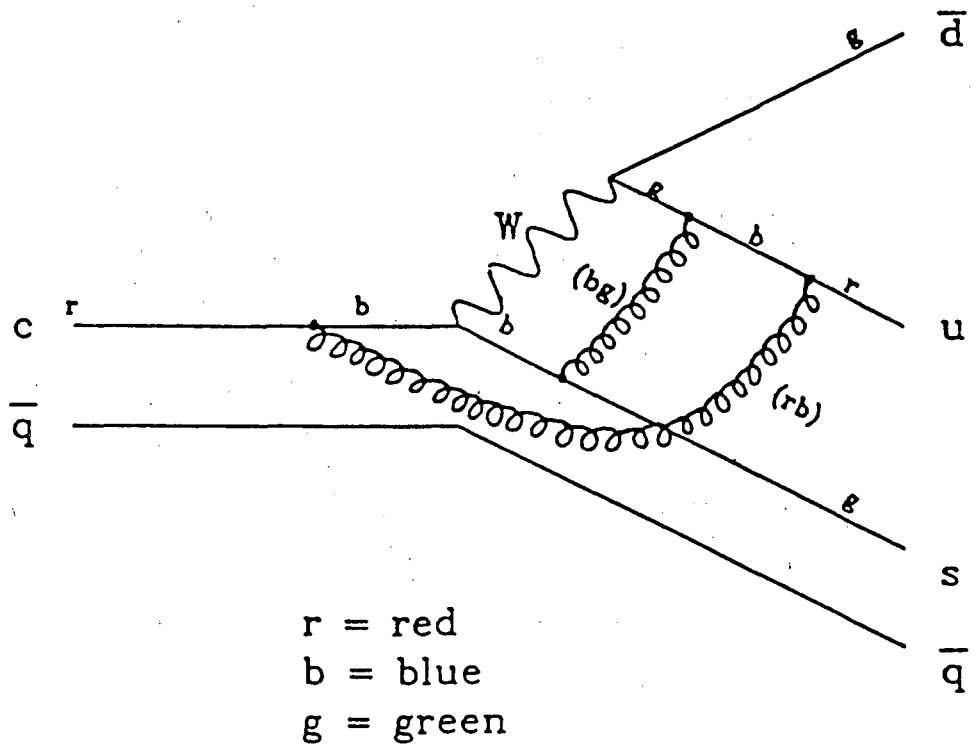

Figure 1.7: Rearrangement of color flow in the spectator diagram.

spectator diagram for non-leptonic charm decay (Figure 1.6 (a) with $c \to su\bar{d}$), the interaction Hamiltonian can be expressed in an abbreviated form (neglecting γ matrices) as:

$$H_W = \frac{G_f}{\sqrt{2}} \cos^2\theta_c (\bar{s}c \cdot \bar{u}d)$$

Since the W boson does not carry color, the strange quark must carry the same color as the charm quark and the up quark carries the same color as the down antiquark. For any given color of the charm quark, there are three possible colors for the $u\bar{d}$ pair. Gluons can alter the flow of color in the diagram. An example of a spectator diagram with rearranged color flow is shown in Figure 1.7. The net effect of including such diagrams is to give rise to two terms in the Hamiltonian [28]:

$$H_W = \frac{G_f}{\sqrt{2}} \cos^2\theta_c \left[\frac{f_+ + f_-}{2} (\bar{s}c \cdot \bar{u}d) + \frac{f_+ - f_-}{2} (\bar{s}d \cdot \bar{u}c) \right]$$

The coefficients f_+ and f_- are given by:

$$f_- = f_+^{-2} = [\alpha_s(M_Q)/\alpha_s(M_W)]^{(12/(33-2N_f))}$$

The first term has the same color arrangement as the original Hamiltonian while in the second term the up quark carries the color of the charm quark and the strange quark carries the same color as the down antiquark. In order to compute rates using this model one must also take the K-M mixing angles and the phase space factors into account. As an example, Leveille calculates the charm semileptonic branching ratio in the approximation of $m_u=m_d=m_s=0$, $m_c=1.5$ Gev/c^2 and m_W =80 Gev/c^2. With these masses, $f_+ \simeq 0.69$ and $f_- \simeq 2.09$. The nonleptonic rates are enhanced by a factor of $(2f_+^2 + f_-^2) \simeq 5.32$, compared to a factor of 3 in the simple model. This results in a semileptonic branching ratio prediction of:

$$B(c \to X \ell \bar{\nu}_\ell) = 1/(2 + 2f_+^2 + f_-^2) \simeq 13\%$$

as compared to 20% predicted by the simple spectator model. If the single gluon radiative corrections discussed earlier are also included, the semileptonic branching ratio decreases from 13% to about 10% in reasonable agreement with the experimental data in Table 1.2

These improvements to the simple spectator model do not explain the differences in the D^0 and D^+ semileptonic branching ratios. This difference must arise from non-spectator diagrams in which the light quark also participates in the decay. The possible non-spectator diagrams for D^0, D^+ and F^+ decays are shown in Figure 1.8. Important points to note are: (1) the D^0 non-spectator diagrams are purely non-leptonic; (2) the D^+ diagram is K-M suppressed; (3) the F^+ diagram is K-M favored; (4) all non-spectator diagrams are helicity suppressed (in analogy to pion decay in which $\pi \to e\nu$ is suppressed relative to $\pi \to \mu\nu$). In order for these diagrams to contribute significantly, the helicity suppression mechanism must be overcome. This can be accomplished by including the effects of gluons. These gluons can either be included in the charmed meson wave function or can be emitted before the decay interaction, leaving the meson in a spin 1 state. With the proper choice of certain phenomenological parameters, the contributions from the non-spectator D^0 diagrams can be comparable to those of the spectator diagrams. Since there are no corresponding K-M favored diagrams for the D^+ decays, the difference in the D^0 and D^+ semileptonic branching ratios can be explained.

All of the enhancements to the simple spectator model for charm decays also apply to bottom decays. The strong interaction corrections

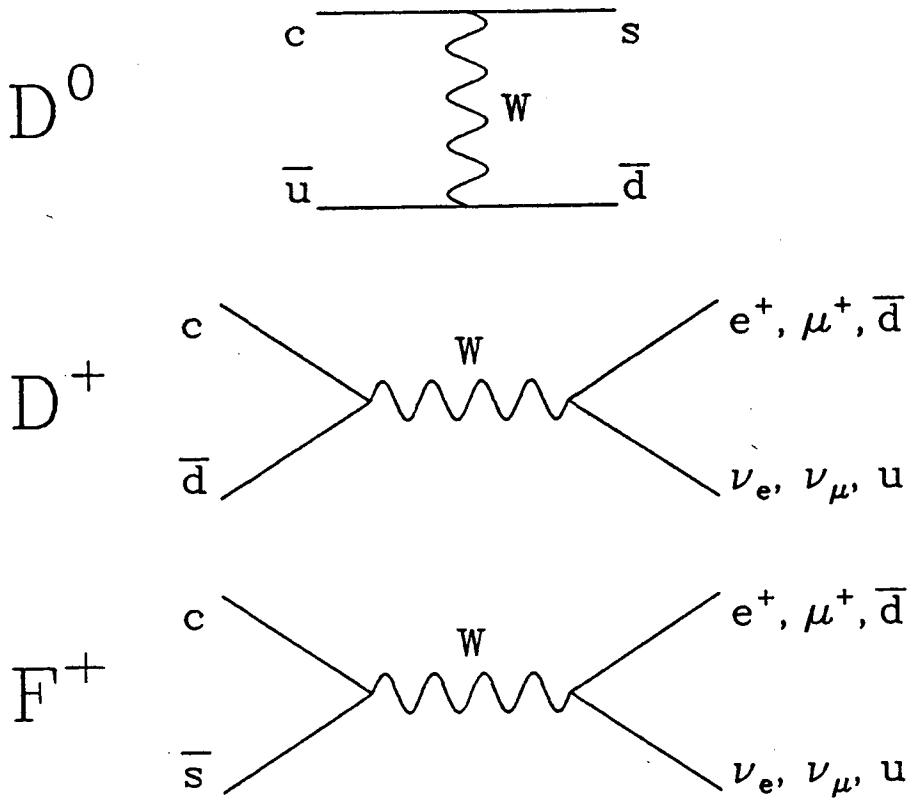

Figure 1.8: Non-spectator diagrams for D^0, D^+, and F^+ decays. Strong interaction corrections (gluons) are not included in the diagrams

should be smaller for bottom decays than charm because the strong coupling constant α_s is smaller at larger mass scales. In Table 1.2 we saw that experimental results on the semileptonic branching ratios of bottom hadrons were in the 12-13% range whereas the simple spectator model predicted $\simeq$ 17%. Leveille has calculated the semileptonic branching ratio for bottom decays, including strong interaction corrections, to be 11-13%, in good agreement with the experimental results.

1.5 Analysis Objective and Motivation

The goal of this thesis is to study the inclusive production of prompt leptons arising from the semileptonic decays of heavy quarks. This study will be carried out using data from the Mark II detector at the PEP storage ring to investigate hadronic events from e^+e^- annihilations at 29 GeV. We are particularly interested in investigating the properties of the recently discovered bottom hadrons as well as in furthering the understanding of the charmed hadrons. There are two properties of these heavy particles which we will investigate in this analysis.

The first such property is the average semileptonic branching ratio. This quantity has been measured for bottom quarks at the $\Upsilon(4S)$ at the CESR storage ring (see Table 1.2). At the CESR energy (10.55 GeV), only the lowest lying B meson states (B_d^0, B_u^-) can be produced. At a center-of-mass energy of 29 GeV, other bottom flavored hadrons, such as the B_s^0 meson or bottom baryons can also be produced. The semileptonic branching ratio measured at 29 GeV will thus be an average over all weakly decaying bottom mesons and baryons, weighted by their

relative populations. If the branching ratio measured at 29 GeV were significantly different from that measured at CESR, it might be an indication of the presence of a bottom hadron species that has a substantially different semileptonic branching ratio.

This point concerning the measurement of a "weighted" average branching ratio is also particularly relevant to the charmed mesons which are known to have different semileptonic branching ratios for D^+ and D^0 (see Table 1.2). Recent measurements of the D^* production cross-section in e^+e^- annihilations at 29 GeV [6] indicate that D^* production may comprise a significant fraction of the total charm cross-section. Since $\simeq$ 64% of D^{*+} decays and 100% of D^{*0} decays result in a D^0, the production of D^*'s can lead to a D^0 to D^+ ratio that is significantly greater than 1. In this case, one would expect to measure an average charm semileptonic branching ratio that is smaller than the averages measured at the ψ'' (see Table 1.2) where the ratio of D^0 to D^+ is $\simeq$ 1.27. In addition, as in the case of bottom, any significant production of other hadron species (e.g. F^+, Λ_c^+) could also affect the measured average.

The second property of interest is the fragmentation functions for charm and bottom quarks. As we have already discussed in section 1.3, the charm quark fragmentation is harder than that of light quarks. The theoretical expectation is that the bottom quark fragmentation will be even harder (i.e. peaked near z=1) than that for charm. In this thesis we will obtain the first experimental information on the b-quark fragmentation function.

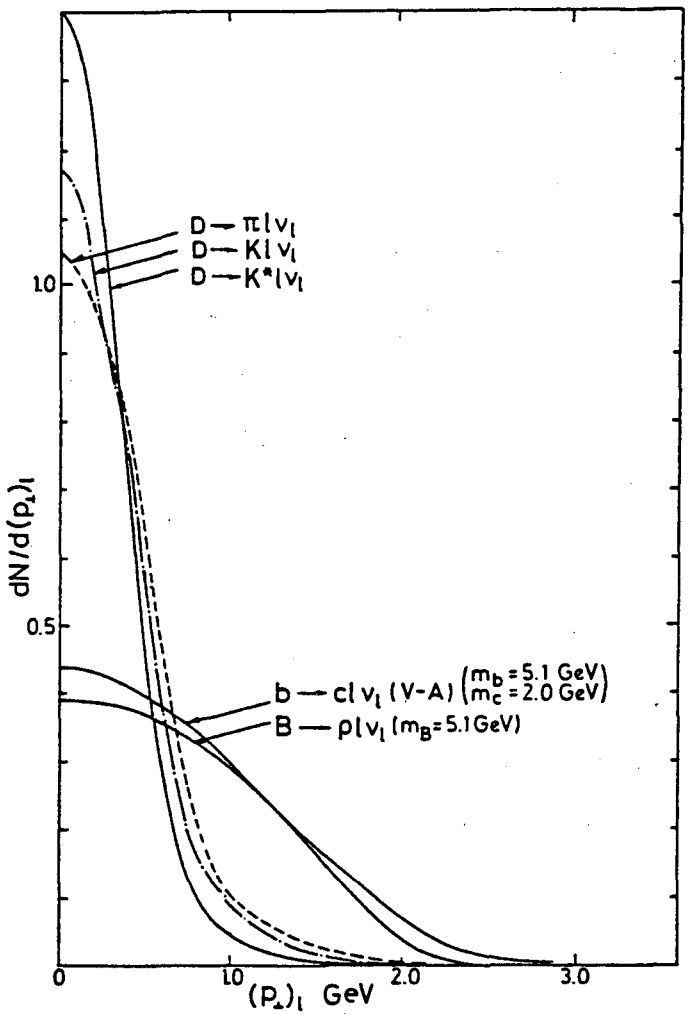

Figure 1.9: Transverse lepton momentum distributions
This figure is taken from Ref. [30].

In order to investigate these properties of charm and bottom quarks, we need a way to distinguish the leptons which arise from their semileptonic decays. The contribution from bottom decays can be enhanced by selecting events in which the lepton has a relatively large transverse momentum $p_\perp$ with respect to the event jet axis. This approach was first suggested by Barger et al. [29] and extensive discussions of its applications in e^+e^- annihilations at PEP and PETRA energies have been presented by Ali [30] and by Puhala et al. [31]. Figure 1.9 shows typical lepton transverse momentum distributions for a few heavy quark decay models. The fact that the signal above $p_\perp$ of $\simeq$ 1 GeV/c is largely from bottom decays will allow us to distinguish between the contributions from charm and bottom.

In this thesis we will measure both the total momentum (p) and transverse momentum ($p_\perp$) spectra of prompt electrons and muons in hadronic events. The transverse momentum $p_\perp$ will be measured with respect to the thrust axis defined by all the charged particles in the event. Due to the limitations of our electron and muon identification algorithms we will not be able to identify electrons with $p < 1$ GeV/c or muons with $p < 2$ GeV/c. In the following chapters, the data will typically be presented in a two-dimensional matrix, binned in 1 GeV/c bins of p and 0.5 GeV/c bins of $p_\perp$, as illustrated in Table 1.3 below.

P\PT	0.00	0.50	1.00	1.50
1.0 2.0 3.0 4.0 5.0 6.0				

Table 1.3: Typical (p,$p_\perp$) table.
The headings to the left of each row indicate the value of the low edge of the momentum bins in units of GeV/c. The headings at the top of each column indicate the low edge of the transverse momentum bins. The last bin in a row or column contains all overflows (e.g. $p > 6$ GeV/c or $p_\perp > 1.5$ GeV/c).

2. THE MARK II DETECTOR

The MARK II detector is a multi-purpose magnetic detector, designed to detect both charged and neutral particles produced in e^+e^- annihilations. The Mark II was installed in the SPEAR storage ring at the Stanford Linear Accelerator Center (SLAC) in the winter of 1977-1978. Data on e^+e^- annihilations at center of mass energies between 3.0 and 7.4 GeV were collected from the spring of 1978 until the summer of 1979. The detector was moved out of SPEAR in the summer of 1979 and installed in the PEP storage ring at SLAC. The detector configuration at PEP differed only slightly from that at SPEAR. Thus the detector performance and characteristics were well understood from the outset of the PEP data analysis.

The data to be discussed in this thesis were collected at PEP at a center of mass energy of 29 GeV from the winter of 1980 until the summer of 1982 and correspond to a total integrated luminosity of 32 pb^{-1}. Figures 2.1 and 2.2 show cross sectional and isometric views of the detector as it was configured at PEP. For the data analyzed in this thesis, there were three slightly different detector configurations. These three configurations are summarized in Table 2.1. The details of the individual detector components will be discussed in the following sections.

2.1 Beam Pipe

For configuration 1, the vacuum around the interaction region was contained by a 2 mm thick aluminum pipe. It was 8.0 cm in radius and had a length of 1.5 m. For configurations 2 and 3, the vacuum was contained by a 1.4 mm thick beryllium pipe which also served as the

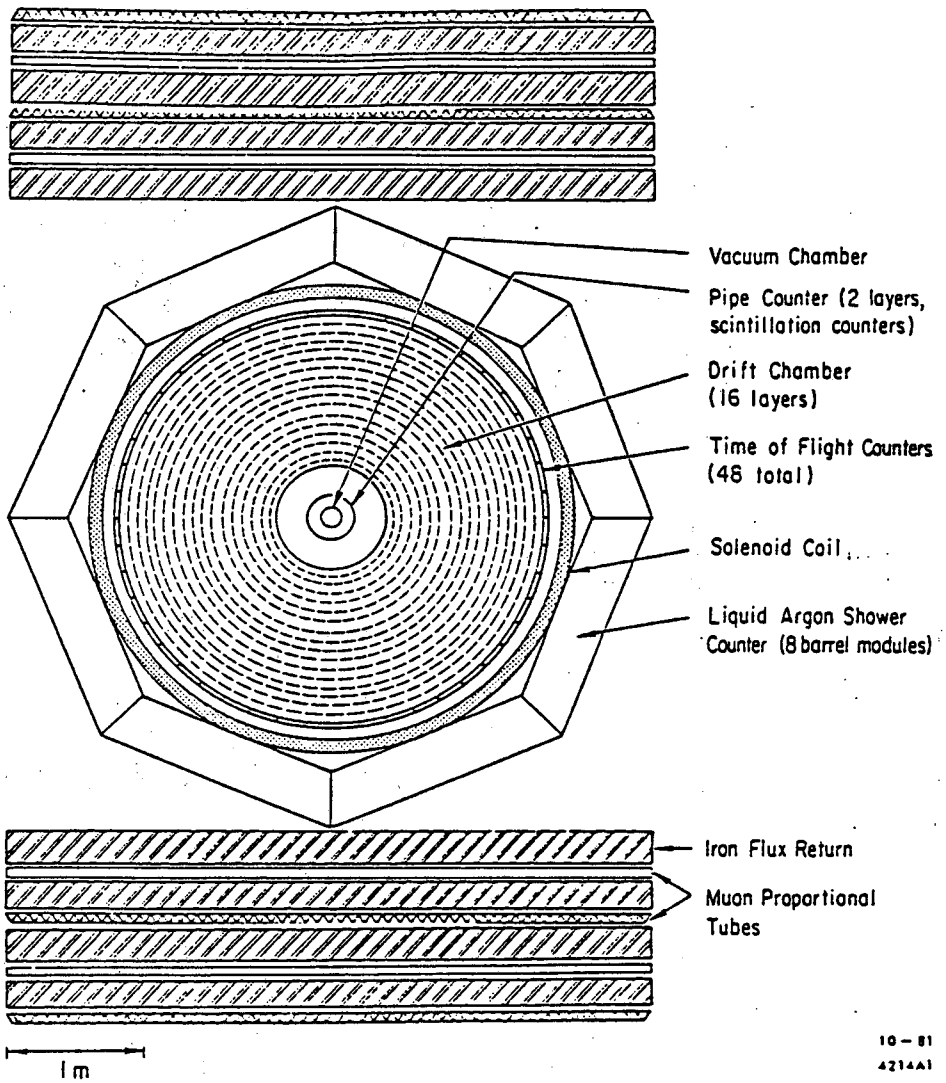

Figure 2.1: A cross sectional view of the MARK II detector at PEP.

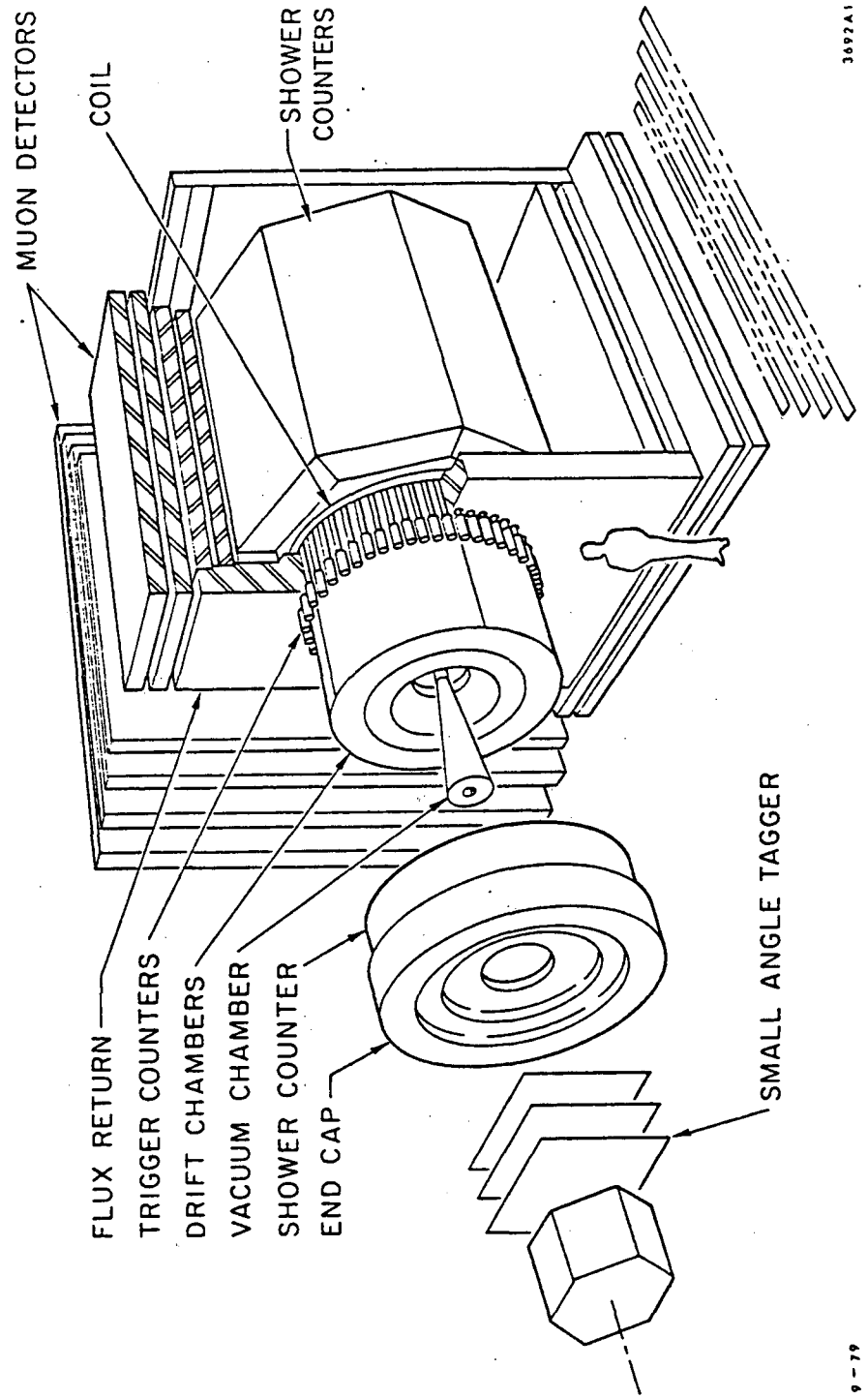

Figure 2.2: An isometric view of the MARK II detector at PEP

Detector Element	Mean Radius (cm)	Thickness (cm)	Thickness (gm/cm^2)	Radiation Length	Comments
CONFIGURATION 1					
Integrated Luminosity ≈ 15.4 pb^{-1}					
Momentum resolution $(\sigma_p/p)^2 \approx (.01)^2 + (0.01p)^2$					
Vacuum pipe	8.0	0.2	0.5	0.023	Aluminum
Pipe counter	12.1	3.8	1.6	0.035	
Trig. chmbr.	18.5	7.3	0.7	0.025	
Lexan window	37.3	0.3	0.4	0.009	
Drift chmbr.	94.0	113.0	0.2	0.009	
Outer can	151.0	0.6	1.7	0.071	
TOF counters	152.0	2.6	2.7	0.064	96 PM tubes
Magnet Coil	155.0	12.0	35.0	1.300	B=4.6 kG
Calorimeter	190.0	40.0	135.0	16.500	
Muon system	350.0	105.0	800.0	60.000	
CONFIGURATION 2					
Integrated Luminosity ≈ 3.4 pb^{-1}					
Momentum resolution $(\sigma_p/p)^2 \approx (.01)^2 + (0.01p)^2$					
* Vacuum pipe	7.7	0.2	0.3	0.006	Beryllium
* Vertex chmbr.	21.0	26.0	0.4	0.022	
Lexan window	37.3	0.3	0.4	0.009	
Drift chmbr.	94.0	113.0	0.2	0.009	
Outer can	151.0	0.6	1.7	0.071	
TOF counters	152.0	2.6	2.7	0.064	
Magnet Coil	155.0	12.0	35.0	1.300	
Calorimeter	190.0	40.0	135.0	16.500	
Muon system	350.0	105.0	800.0	60.000	
CONFIGURATION 3					
Integrated Luminosity ≈ 18.4 pb^{-1}					
Momentum resolution $(\sigma_p/p)^2 \approx (.02)^2 + (0.01p)^2$					
Vacuum pipe	7.7	0.2	0.3	0.006	
Vertex chmbr.	21.0	26.0	0.4	0.022	
Lexan window	37.3	0.3	0.4	0.009	
Drift chmbr.	94.0	113.0	0.2	0.009	
Outer can	151.0	0.6	1.7	0.071	
* TOF counters	152.0	2.6	2.7	0.064	93 PM tubes
* Magnet Coil	155.0	12.0	35.0	1.300	B=2.3 kG
Calorimeter	190.0	40.0	135.0	16.500	
Muon system	350.0	105.0	800.0	60.000	

Table 2.1: MARK II detector configurations.
* denotes a change from previous configuration.

inner wall of the vertex drift chamber. This pipe was at a radius of 7.7 cm and was 1.4 m in length. A 50 μm thick titanium foil cylinder was inserted inside the beryllium tube to absorb synchrotron radiation. The outside of the tube was wrapped with a 50 μm sheet of mylar to insulate it from a 25 μm sheet of aluminum foil which served as a ground shield for the vertex chamber. The beam pipe was constructed from beryllium in order to minimize the multiple scattering contribution to the track extrapolation error.

2.2 Pipe Counter

Four hemi-cylindrical scintillation counters formed two concentric cylinders around the beam pipe in configuration 1. The inner radii of the two cylinders were 11.0 and 12.5 cm and they were each 81 cm in length. Signals from photomultiplier tubes which viewed the counters were used in the primary trigger logic to reduce the background from cosmic ray events. There was no pipe counter in configurations 2 and 3.

2.3 Trigger Chamber

The trigger chamber was a cylindrical drift chamber that occupied the space between the pipe counter and the main drift chamber in configuration 1. The 86 cm long chamber consisted of four layers each containing 64 drift cells. The inner and outer layers were at radii of 17 and 20 cm. The resolution was about 300 microns at each layer. Signals from this chamber were used in both the primary and secondary trigger. Because of its small radius and short length relative to the main drift chamber, the trigger chamber provided a factor of 2 reduction in trigger rate by rejecting background tracks originating at large r and z. The information from this chamber was not used in the charged

track reconstruction in this analysis. The trigger chamber was replaced by the vertex chamber for configurations 2 and 3.

2.4 Vertex Chamber

The vertex chamber is a high precision drift chamber which was designed to accurately measure the position of secondary vertices resulting from particle decays. It replaced the trigger chamber and pipe counter in configurations 2 and 3. The vertex chamber consists of seven layers of sense wires grouped into two bands. The inner band contains four layers of 60-75 sense wires each at radii between 10 and 13 cm from the beamline. The outer band contains three layers of 180-190 sense wires each at radii between 30 and 32 cm. The distance between sense wires and field wires is 0.53 cm. The spatial resolution per layer is $\simeq$ 110 μm. The rms error on the position of a track extrapolated to the interaction point is given by $\sigma_t^2 \simeq (95\mu m)^2 + (95\mu m/p)^2$. The second term is the contribution from multiple scattering in the 0.6% radiation length beryllium beam pipe.

2.5 Main Drift Chamber

The main drift chamber consists of sixteen cylindrical layers at radii between 41 and 145 cm enclosed in a common gas volume. Six layers are parallel to the incident beams and the other 10 are skewed at ± 3° relative to the beams. The per layer spatial resolution is typically 200 μm. For configuration 3 (half-field), the rms momentum resolution in the plane transverse to the incident beams is given by:

$$(\delta p_\perp/p_\perp)^2 \simeq (0.02)^2 + (0.01p)^2$$

where p is in units of GeV/c. In this analysis the momentum measurement is combined with information from the liquid argon calorimeter to select

electron candidates and with information from the muon system to identify muon candidates.

2.6 Time of Flight System

The time of flight (TOF) system consists of 48 Pilot F scintillators surrounding the main drift chamber at a radius of 1.5 m. Each 1 inch thick scintillator is 3.4 m long and viewed at each end by a 2 inch XP2230 photomultiplier tube. The output of each phototube is processed to obtain both timing (TDC) and pulse height (ADC) information. In addition, a time-compensated latch signal for each scintillator is provided for use in the primary and secondary trigger. The ADC information is used to perform pulse-height slewing corrections to the TDC information for each tube. The time of flight for a particle traversing a scintillator is calculated from an average of the two corrected phototube times. If two charged particles traverse a single scintillator (as determined from the drift chamber information) then the time of flight for each particle is calculated using the information from the phototube which is unobstructed by the other track. If three or more particles traverse a single scintillator then the time of flight information is considered unusable. The overall resolution of the TOF system for the single hit case is approximately 350 ps. In this analysis, the TOF information is used to identify low momentum electron candidates belonging to potential photon conversion or Dalitz decay pairs.

2.7 Magnet Coil

The aluminum coil of the solenoid magnet lies just beyond the TOF counters at a radius of 1.6 m. The magnet consists of two layers of

water cooled aluminum conductor with insulating material between the two layers. In configurations 1 and 2, the magnet provided a nominal longitudinal field of 4.64 kG. Configuration 3 resulted from an electrical short which developed between the two layers of the magnet windings. In order to operate the magnet in this condition it was necessary to power only the outer winding while letting the inner one float. This was accomplished by cutting the aluminum conductor at the end of the detector where the inner and outer windings joined. As a result, three of the TOF phototube assemblies also had to be removed from that end of the detector. In the new configuration the magnet provided a nominal 2.32 kG field.

2.8 Endcap calorimeters

At each end of the Mark II detector are proportional chamber calorimeters which cover the polar angular region from $\simeq$ 15° - 40° except for cutouts in ϕ to accommodate the door keyways. Each endcap consist of two layers of proportional chambers, each preceded by about 2.3 radiation lengths of lead. The rms energy resolution for photons and electrons is approximately $\sigma(E)/E \simeq 50\%/\sqrt{E(GeV)}$.

2.9 Small Angle Tagging System

The small angle tagging (SAT) system provides charged particle tracking and calorimetry in the angular region from 21-82 mrad with respect to the beamline. The SAT system was designed to detect the scattered electrons resulting from either small angle Bhabha events or two-photon interactions. The measurement of the small angle Bhabha cross section results in a $\pm$ 5% determination of the luminosity.

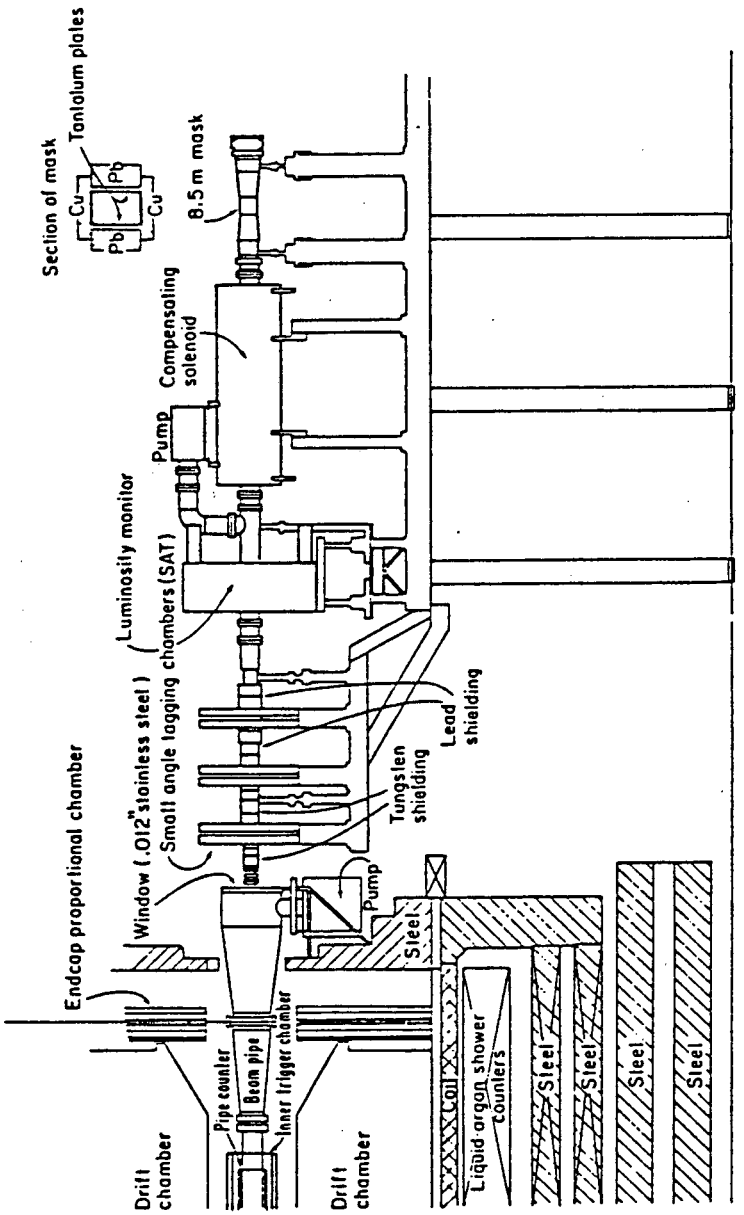

Figure 2.3: A view of the MARK II detector showing the SAT system.

Figure 2.3 shows the details of the SAT system. Each SAT counter system consisted of three layers of planar drift chambers, three layers of acceptance defining scintillation counters, and a shower counter. Each drift chamber layer contained three pairs of 20 μm sense wires. Each pair of sense wires is placed above an inductive delay line. This combination provides a spatial resolution of ≃ 300 μm in the drift coordinate and ≃ 0.5 cm in the delay line coordinate. The acceptance scintillators are arranged in such a way as to define four axes along which the colinear electrons from a bhabha event would travel. These counters are used in the luminosity measurement. The shower counters consist of eighteen layers of 1/4 inch lead sheets followed by NE114 plastic scintillator. Light from the scintillators was transfered to 2 inch phototubes via plastic sheets doped with a wavelength shifting compound BBQ. The energy resolution of the calorimeters is $\sigma(E)/E \simeq 15.5\%/\sqrt{E}$.

2.10 Liquid Argon Calorimeter

The Mark II liquid argon (LA) calorimeter system has been described in reference [32]. The details that are relevant to the understanding of the electron identification algorithm (Chapter 3) will be described here. The LA calorimeter system consists of 8 modules (3.8 m long × 1.8 m wide × 0.3 m deep) in an octagonal array surrounding the magnet coil. At the front of each module is a "massless" gap consisting of three aluminum planes separated by 8 mm LA gaps. The central plane is segmented into 3.8 cm wide readout strips running parallel to the incident beams. This "massless" gap was designed to identify showers which begin in the 1.25 radiation length magnetic coil which precedes

the calorimeter modules. The remaining sensitive volume of each module consists of 37 planes of 2 mm thick antimony strengthened lead planes separated by 3 mm LA gaps. The lead planes and LA gaps are arranged in the following pattern:

1) A solid plane at ground potential
2) A liquid argon gap
3) A segmented readout plane at +3.5 kV
4) A liquid argon gap

This arrangement results in 18 readout layers in depth, each of which contains a central segmented readout plane to measure the ionization in two LA gaps. Each of the 18 readout layers is $\simeq$ 0.8 radiation length thick resulting in a total calorimeter thickness of $\simeq$ 14.5 radiation lengths. About 20% of the energy is deposited in the liquid argon. The readout planes are segmented into strips as follows:

1) F strips: 9 of the 18 layers have 3.8 cm wide strips running parallel to the beam direction and thus measure the azimuthal angle ϕ.

2) T strips: 6 of the layers have 3.8 cm wide strips running perpendicular to the F strips and thus measure the polar angle θ.

3) U strips: The remaining 3 layers have 5.4 cm wide strips running at 45° with respect to the F and T strips. These layers help resolve multi-hit ambiguities.

In order to reduce the amount of readout electronics, some layers with the same strip orientation were grouped together to form six ganged readout layers (F1, T1, U, F2, T2, and F3) as shown in Figure 2.4.

The overall rms energy resolution is $\sigma(E)/E \simeq 12\%/\sqrt{E}$. The sensitive area of the calorimeter system which is used in the electron identification procedure covers $\simeq$ 64% of the 4π solid angle.

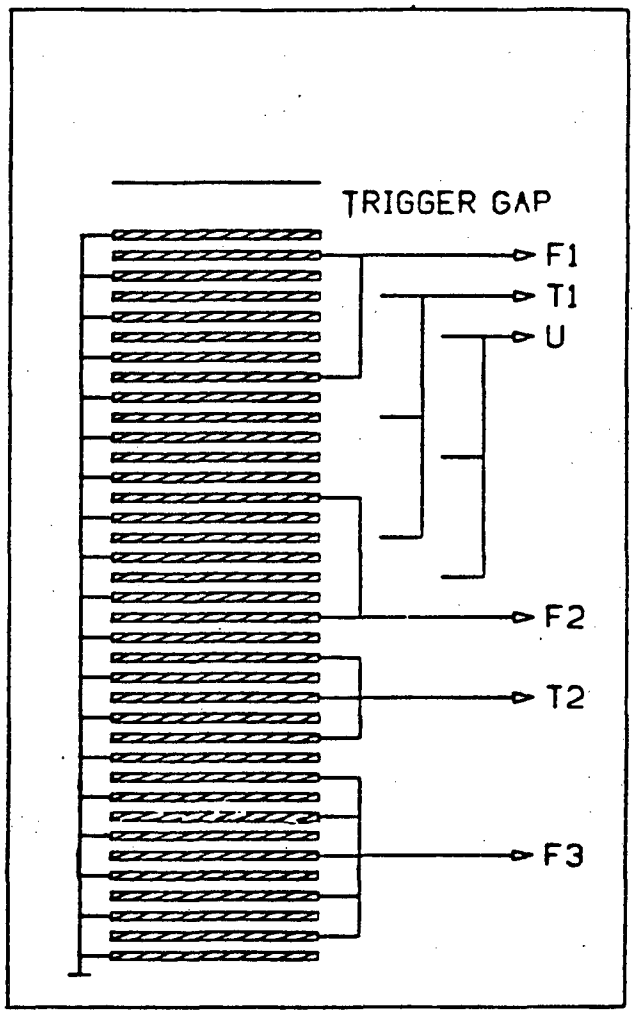

Figure 2.4: Ganging pattern in LA calorimeter modules
In this view, incident particles would enter from the top (i.e. the first layer encountered would be the Trigger Gap.

2.11 Muon System

The Mark II muon system at SPEAR has been described in detail in reference [33]. The muon system at PEP consists of 4 walls located above, below, and on either side of the central detector. Each wall consists of alternating layers of steel hadron absorber plates and layers of proportional tubes. At PEP there are four such layers in each wall. The properties of each wall are shown in Table 2.2. The proportional tubes in the first level of each wall are oriented so that they measure the polar coordinate θ while the second through fourth levels measure the azimuthal coordinate ϕ. The fourth level of the muon system covers $\simeq$ 45% of the 4π solid angle.

	East Wall		Top Wall		West Wall		Bottom Wall	
Level	D (m)	T (gm/cm^2)	D (m)	T (gm/cm^2)	D (m)	T (gm/cm^2)	D (m)	T (gm/cm^2)
1	3.2	182	2.5	182	3.2	182	2.5	182
2	3.6	184	2.8	184	3.6	184	2.8	184
3	4.0	244	3.2	239	4.0	244	3.2	244
4	4.5	196	3.6	184	4.5	196	3.6	244
Total		806		789		806		854

Table 2.2: Muon system configuration
D is the perpendicular distance from the center of the absorber to the interaction point. T is the absorber thickness.

A cross sectional view of a proportional tube module is shown in Figure 2.5. Each extruded aluminum module contains 8 triangular tubes which run the full length of the absorber layer. The 45 μm sense wires

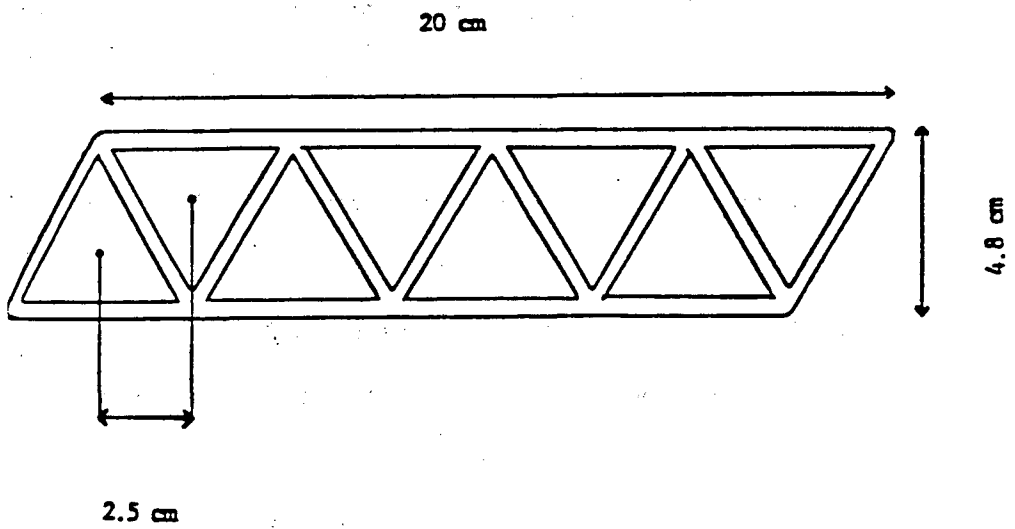

Figure 2.5: A cross sectional view of a muon proportional tube module

are spaced 2.5 cm apart. This spacing is well matched to the typical extrapolation errors arising from the drift chamber tracking error and multiple Coulomb scattering.

2.12 Event Trigger

The Mark II trigger system at SPEAR has been described in detail in reference [34]. The changes to the system since the move to PEP will be described below.

Overview:

The time between beam crossings at PEP is 2.4 μsec compared to 780 nsec at SPEAR. The event trigger is implemented as a two level process. At the first level (primary trigger) a decision to keep or reject the detector information is made with ≃ 1 μsec after beam crossing. If there is no evidence of a potentially interesting event the detector electronics is reset in time to accept data from the next beam crossing. Thus there is no associated deadtime from the primary trigger. If there is evidence of an interesting event, the primary trigger logic sends a signal to the Master Interrupt Controller (MIC). The MIC module transmits a signal (WAIT) to the detector electronics to prevent data collection from subsequent beam crossings. MIC sends another signal (START) to the Master Clock (MC) module which controls the hardware track finding electronics. During the 30 μsec hardware track finding process, the MC sends a signal (BUSY) to MIC. This 30 μsec delay introduces a deadtime of 3% per kHz primary rate. When the hardware track finding is complete, MIC makes a final trigger decision (secondary trigger) based on the information from the hardware track processor and from other detector components. If a secondary trigger is initiated,

the MIC module sends an interrupt to a VAX 11/780 computer which then reads the detector data and writes the data to tape. At the end of the data transfer, or if a secondary trigger was not initiated, MIC removes the WAIT signal and the detector electronics are reset to enable data collection from the next beam crossing.

Primary Trigger:

The charged particle primary trigger requires a coincidence of a beam crossing signal (BX), a drift chamber majority (DCM) requirement for layers in the inner and main drift chambers, and a time-compensated latch from at least one time-of-flight scintillator (TOF). In configuration 1, a pipe counter signal was also used to further reduce the background from cosmic ray events. The primary trigger rate is typically less than 1 kHz, resulting in less than 3% deadtime from the secondary trigger.

The BX signal is derived from a signal induced on a beam pickup electrode located inside the PEP vacuum pipe near the Mark II interaction point. The DCM signal is derived from a set of inner and main drift chamber signals called "LAYER OR". Each layer (7 vertex chamber, 16 main drift chamber) has an associated signal which is true if any sense wire within the layer had a hit. These signals are connected to a programmable memory logic module (MLM) which forms a majority signal based on pre-programmed requirements. A typical majority requirement was:

	≥ 2/4	Inner	vertex chamber layers
and	≥ 1/3	Outer	" " "
and	≥ 2/4	Innermost	main chamber layers
and	≥ 1/3	Mid-inner	" " "
and	≥ 1/3	Mid-outer	" " "
and	≥ 2/4	Outermost	" " "

The programmability of the majority requirement made it easy to maintain a high DCM efficiency (> 99%) for good events even when some drift chamber layers were operating at low efficiency. This was accomplished by simply excluding these layers from the programmable majority requirement.

In addition to the charged particle primary trigger described above, there were also primary triggers associated with a total energy trigger derived from the calorimeters and a small angle bhabha trigger derived from the SAT system.

Hardware Track Finding:

The hardware track finding electronics is identical to that at SPEAR [34]. The only changes have been in the "shapes" of the programmable curvature masks in the Curvature Modules and in the programmable requirements on the track definition criteria. Figure 2.6(a) illustrates how the curvature module "roads" were defined at SPEAR. Figure 2.6(b) shows an enlargement of a single road. All tracks with radii of curvature ρ between ρ_1 and ρ_2 which originate from the beamline can be contained within this road. This is also true of the new road illustrated in Figure 2.6(c). The roads in 2.6(b) and (c) are equivalent when the intersection point R_{int} is equal to R_{max}. The curvature roads at PEP were defined by first constructing the roads as defined at SPEAR (Fig. 2.6(a)). The intersection point of each road was then moved from R_{max} to $0.25 \times R_{max}$. This definition results in roads with smaller angular widths $\delta\phi$ at small radii (i.e. for vertex chamber and trigger chamber layers). This results in an improved rejection of background tracks originating at large radii from the beamline.

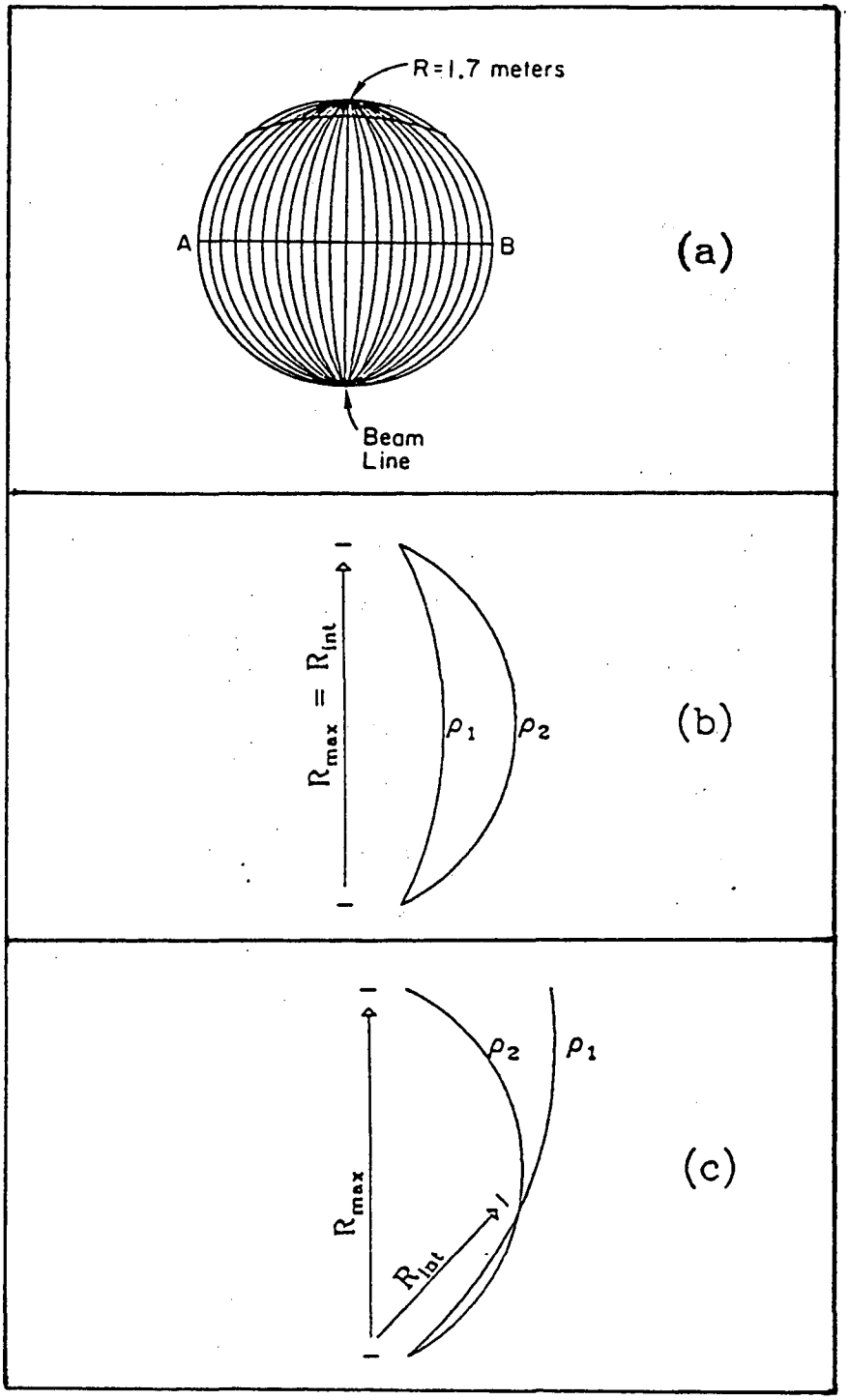

Figure 2.6: Definitions of hardware track processor curvature roads. (a) Original (SPEAR) definition. (b) Enlargement of an old road (SPEAR). (c) Enlargement of new road (PEP).

The typical track definition requirements ("A" track definition) at PEP required the following number of channels within a curvature road:

≥ 2/4 inner vertex chamber layers
and ≥ 5/7 main drift chamber layers
and ≥ 1/3 outer main drift chamber layers
and an associated TOF counter.

Secondary Trigger:

The secondary trigger typically required one or more of the following conditions to be satisfied:

(a) ≥ 2 tracks found by the hardware track processor

The hardware track processor required these tracks to have momenta greater than ≃ 100-200 MeV/c and to be within the central ≃ 67% of the detector solid angle.

(b) At least 1 GeV of energy deposited in the front half of 2 or more of the 8 barrel LA calorimeters.

(c) A small angle bhabha event in the SAT counter system.

Because of the high rate for this topology, this trigger was typically prescaled by a factor of 16.

3. ELECTRON IDENTIFICATION

3.1 General philosophy

Electrons can be distinguished from other stable charged particles by the nature of their interaction with matter. The difference arises primarily from the bremsstrahlung process in which the electron loses energy by radiating photons. Bremsstrahlung is the dominant energy loss process for electrons above the critical energy ($\simeq$ 7 MeV in lead). This mechanism of energy loss is suppressed for heavier particles by a factor of $\simeq (m_e/m)^2$ where m is the particle mass. It is negligible for other stable charged particles (muons, pions, kaons and protons) which are hundreds of times more massive than the electron.

The bremsstrahlung process results in a unique pattern of energy loss for electrons which is called an electromagnetic cascade shower. The energy distribution for the bremsstrahlung photons is almost constant from zero up to the full energy of the electron. These photons most often interact with matter to either create an electron-positron pair or to eject a single electron from an atom via Compton scattering. In either case, the resulting electrons have energies comparable to the incident photon. These new electrons then radiate more photons which produce more electrons, thus creating a cascade process. This process initially results in an increasing number of particles with increasing depth in the material. The average energy of these particles is decreasing and at some depth will reach the critical energy where ionization energy loss will dominate and the cascade process will terminate. If the material is thick enough, then the full incident electron energy will be deposited in the matter via the cascade process.

A natural first step in developing an electron identification algorithm is to make use of the fact that a high momentum electron will deposit almost all of its incident energy in an appropriately designed calorimeter whereas a typical hadron of the same momentum will only lose a small fraction of its energy. If the energy E_{dep} deposited by a particle with momentum p could be accurately measured, then electrons would have $E_{dep}/p \simeq 1$ and most hadrons would have $E_{dep}/p \ll 1$. A practical electron identification algorithm must also take the finite energy resolution of a real calorimeter into account ($\sigma(E)/E \simeq (10\text{-}15)\%/\sqrt{E(GeV)}$). In order to maintain a high efficiency for electrons above 1 GeV/c, such an algorithm might require $E_{dep}/p > 0.7$ for electron candidates. In practice, however, the misidentification probability of such a method is too large for our purposes. There are two aspects of this standard method that lead to a relatively large misidentification probability. First, in order to obtain good energy resolution, a relatively wide region around the track projection in the calorimeter must be searched to efficiently collect the deposited energy. This results in a sizable probability for mis-measuring E_{dep} by accidently collecting additional energy from nearby particles. Second, in order to properly reconstruct E_{dep}, a sharing algorithm must be implemented which divides the energy deposited on a calorimeter strip among all the photons and charged tracks which could have deposited energy on that strip. This can increase the misidentification probability because the sharing algorithm sometimes mis-assigns energy from photons to nearby charged tracks. It can also decrease the electron identification efficiency by mis-assigning energy from a real electron to other particles in the jet.

One must therefore devise an electron identification algorithm which is less sensitive to these overlap and sharing effects. This can be accomplished by a procedure which does not attempt to accurately reconstruct the deposited energy but which only checks that it is consistent with that expected from an electron shower. An electron will deposit most of its energy in a narrow core around the track projection. This new algorithm will only search for energy in this narrow region. Since some of the deposited energy will fall outside this search region, one might expect that the energy resolution, and thus the electron-hadron separation would be degraded. In practice, however, this approach dramatically improves electron-hadron separation by reducing the contributions from track overlap. In order to alleviate the need to implement sharing schemes, the electron identification algorithm will not reject a candidate if it seems to deposit too much energy. Although this may result in a slightly higher misidentification probability, it has the great advantage of making the identification efficiency insensitive to the patterns of nearby and overlapping energy deposits.

The LA modules are ganged in depth as shown in Figure 2.4. This ganging scheme provides some information on the longitudinal shower development which can be used in the identification algorithm. We will define the "F" energy to be that collected on the strips labelled F1 and F2 in Fig. 2.4. Similarly, we will define the "T" and "U" energies to be those collected on the T1 and U strips. Note that we have excluded the T2 and F3 strips from these groupings. In addition, the "FRONT" energy will be the sum of F1,F2,T1, and U. The "FRONT" grouping

comprises the first ≃ 7 radiation lengths (X_0) of the calorimeter. The algorithm monitors the longitudinal shower development by checking the deposited energy in each of these "coordinates" for consistency with an electron shower. In addition, the algorithm checks the transverse shower properties by searching a narrow region around the track projection.

In order for a track with momentum p to be considered an electron candidate, the energy found within the search region at each layer must be at least as much as would be expected from an electron shower. This expected energy scales approximately with the momentum of the incident track. Minimum ionizing hadrons with p > 1 GeV/c will not deposit enough energy in the calorimeter to lead to misidentification. Some hadrons, however, will interact in the calorimeter and deposit a large fraction of their energy. Many of these interacting hadrons will not be misidentified as electrons because of the specificity of the identification algorithm for the electromagnetic shower topology. This distinction is possible because the interaction length in the calorimeter is much longer than the radiation length. Thus the average hadron shower starts deeper in the calorimeter and tends to be less uniform in both the transverse and longitudinal directions. For example, a hadron that interacts relatively late in the calorimeter will not deposit much energy in the front layers. A hadron interaction which produces high momentum charged secondaries will likely deposit energy relatively far from the track projection, leaving little or none within narrow search region. Such an interaction may also deposit a lot of energy in one layer of the calorimeter, but leave hardly any in another.

Showering hadrons with the above patterns of energy loss are not likely to be misidentified as electron candidates by the algorithm. The interactions that are most likely to be misidentified as electron showers are charge exchange interactions that occur either in the magnetic coil or early in the calorimeter module. These interactions are of the form:

$$\pi^+ + n \rightarrow \pi^0 + p$$
$$\pi^- + p \rightarrow \pi^0 + n$$

The π^0's decay into two photons which then shower electromagnetically, giving uniform longitudinal and transverse showers.

3.2 Implementation

The details of the electron identification algorithm as it is actually implemented are provided below. The following steps are performed for each charged track in an event:

1) The projected coordinates and angles of the track at each LA coordinate (F1, F2, T, and U) are obtained from the drift chamber tracking information.

2) The deposited energy in each coordinate is associated with the incident track in the following manner:

2a) A search width is calculated using the formula:

$$W_{search} = W_{shower} + W_{gang} \times |\tan(\delta)|$$

where W_{search} is the calculated search width, W_{shower} reflects the typical width of an electromagnetic shower ($\simeq$ 3 cm), W_{gang} reflects the additional width arising from the separation ($\simeq$ 4-7 cm) of the front and back of a ganged layer, and δ is the angle between the track projection and the normal to the layer. This angle is measured in the plane which contains the strip coordinate and the normal. Thus for F strips, $\delta \equiv \phi$, and for T strips $\delta \equiv \pi/2-\theta$. W_{shower} actually has an angular dependence given by $W_0/\cos(\delta)$ where W_0 is the width at normal incidence, but this effect is approximately handled by the W_{gang} term. Table 3.1 below shows the values of W_{shower} and W_{gang} that were actually used in the algorithm. The calculated width typically contains $\simeq$ 80-90% of the deposited energy from an electromagnetic shower.

Strip coordinate	W_{shower}	W_{gang}
F1, F2	0.75	0.9
T1	0.75	1.5
U	0.70	1.5

Table 3.1: Values of W_{shower} and W_{gang} in units of strip widths

2b) If the center of a strip lies within the search region, then the energy from that strip is associated with the projected track.

3) The energy associated in each coordinate is designated E_f ($\equiv E_{f1} + E_{f2}$), E_t, and E_u. The sum of E_f, E_t, and E_u is designated E_{front}. We postulate that an electron candidate with momentum p should have:

$$\begin{aligned} & E_f > \alpha_f \times p \quad (\alpha_f = 0.14) \\ \text{and } & E_t > \alpha_t \times p \quad (\alpha_t = 0.10) \\ \text{and } & E_u > \alpha_u \times p \quad (\alpha_u = 0.10) \\ \text{and } & E_{front} > \alpha_{front} \times p \quad (\alpha_{front} = 0.50,\ p < 4;\ \alpha_{front} = 0.40,\ p > 4) \end{aligned}$$

where p is the track momentum and the α parameters are chosen such that most electrons (70%-95%, depending on momentum) will satisfy these four energy requirements.

4) A test of the four requirements stated in 3) above is implemented by defining a variable E_{min} as:
E_{min} = minimum of (F/α_f, T/α_t, U/α_u, $FRONT/\alpha_{front}$)
The four requirements can now be concisely stated as $E_{min}/p > 1$.

In practice, the value of E_{min}/p which is actually used to define electron candidates can be varied. If the cut on E_{min}/p were moved higher, the misidentification probability would decrease as would the electron efficiency. Figure 3.1 illustrates this effect. The figure is based on a sample of known electrons ($p \simeq 1.5$ GeV/c) and pions ($p \simeq 1$ GeV/c) from SPEAR data. The E_{min}/p distributions for these two samples are shown in Figure 3.2

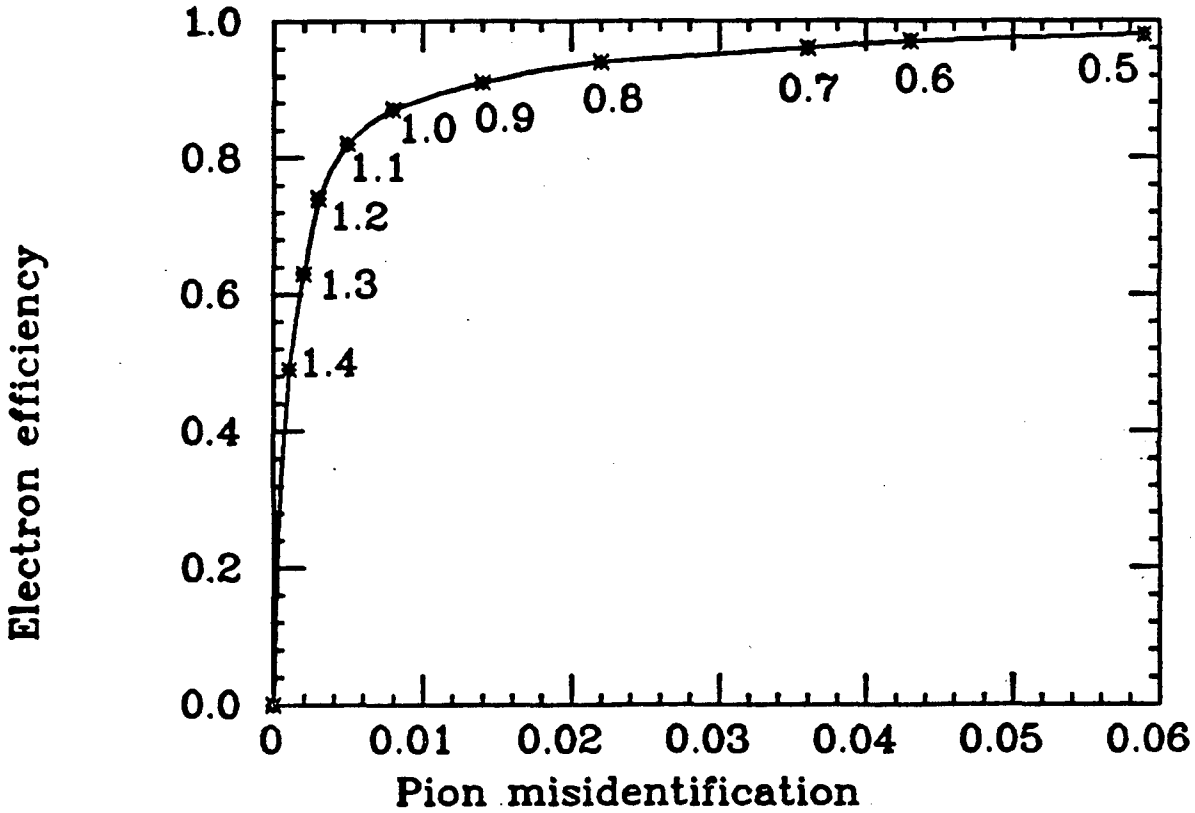

Figure 3.1: Identification efficiency vs. misidentification probability The points on the curve are values of the cut on (E_{min}/p).

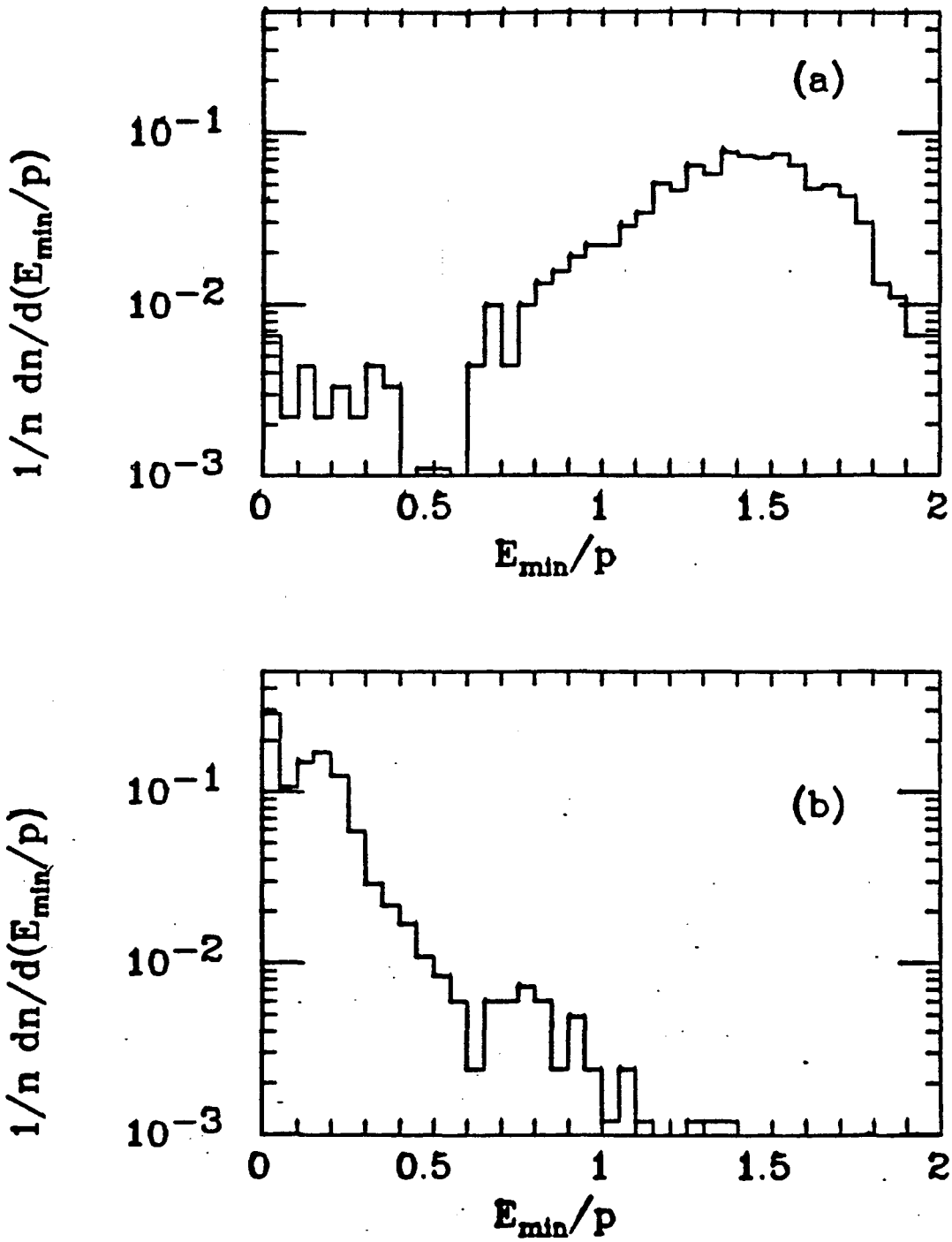

Figure 3.2: Typical E_{min}/p distributions for (a) electrons and (b) pions.

3.3 Identification efficiency

In this analysis, electron candidates are taken to be those tracks that have $E_{min}/p > 1.1$ and which are not too near the edge of a calorimeter module. The sensitive area defined by the latter requirement covers ≃ 64% of the 4π solid angle. This region will be referred to as the electron fiducial volume. The electron identification efficiency for tracks within the fiducial volume has been determined using sources of known electrons.

Electrons from bhabha events ($e^+e^- \rightarrow e^+e^-$) and from identified photon conversions ($\gamma + N \rightarrow e^+e^- + N$) were selected from both SPEAR and PEP data. Figure 3.3 shows the results of these measurements.

Table 3.2 gives the overall identification efficiency as a function of p and $p_\perp$. For a given momentum, the efficiency rises slightly at low $p_\perp$. This is due to the association of additional energy from nearby tracks in the core of a jet. The quoted efficiencies in the 1-2 GeV/c momentum bins are weighted averages of the rising efficiency and the falling electron momentum spectrum within the bins. In the other momentum bins the efficiency is slowly varying. A 2% inefficiency that results from prompt electrons being misclassified as coming from photon conversion pairs (see section 3.5) has been included. The systematic error on the detection efficiencies is estimated to be ± 5% in each bin.

3.4 Hadron misidentification

Charged hadrons are misidentified as electrons whenever the energy collected within the search region at each calorimeter layer is at least as much as would have been deposited by a real electron. This collected energy can either come from the energy actually deposited by the track

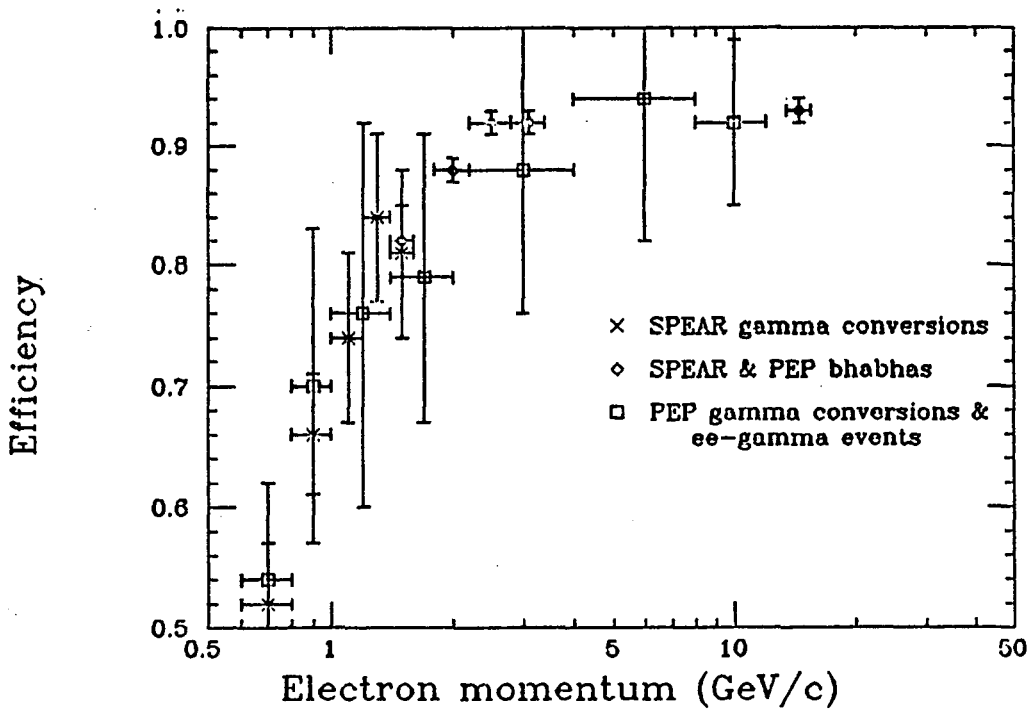

Figure 3.3: Electron identification efficiency vs. momentum

P\PT	0.00	0.50	1.00	1.50
1.0	0.80	0.78	0.76	0.76
2.0	0.90	0.88	0.87	0.87
3.0	0.91	0.91	0.90	0.90
4.0	0.91	0.91	0.90	0.90
5.0	0.91	0.91	0.91	0.91
6.0	0.91	0.91	0.91	0.91

Table 3.2: Prompt electron detection efficiency

of interest or from energy deposited by nearby photons and other charged tracks in the event. We will study these two contributions separately and then see how they combine to affect the overall misidentification probability.

Hadron interactions:

Hadron interactions in the LA calorimeters were studied using known pions from several sources. The results from each of these studies will be discussed below.

Pions from $\psi \rightarrow 2(\pi^+\pi^-)\pi^0$ at SPEAR:

The following selection criteria were used to select event candidates:

- 4 observed charged prongs
- Total charge zero
- Less than 10 unused drift chamber hits after track reconstruction
- No potential gamma conversion pairs
- Recoil mass^2 against 4 prongs within $\pm$ .06 (GeV/c^2)^2 of m_π^2
- Recoil momentum against 4 prongs $>$ 100 MeV/c

Figure 3.4 shows the momentum spectrum of the pions selected by these cuts. Figure 3.5 shows the distributions of E_{min}/p in three different momentum ranges. The misidentification probabilities for a electron selection criterion of $E_{min}/p > 1.1$ are shown in Table 3.3.

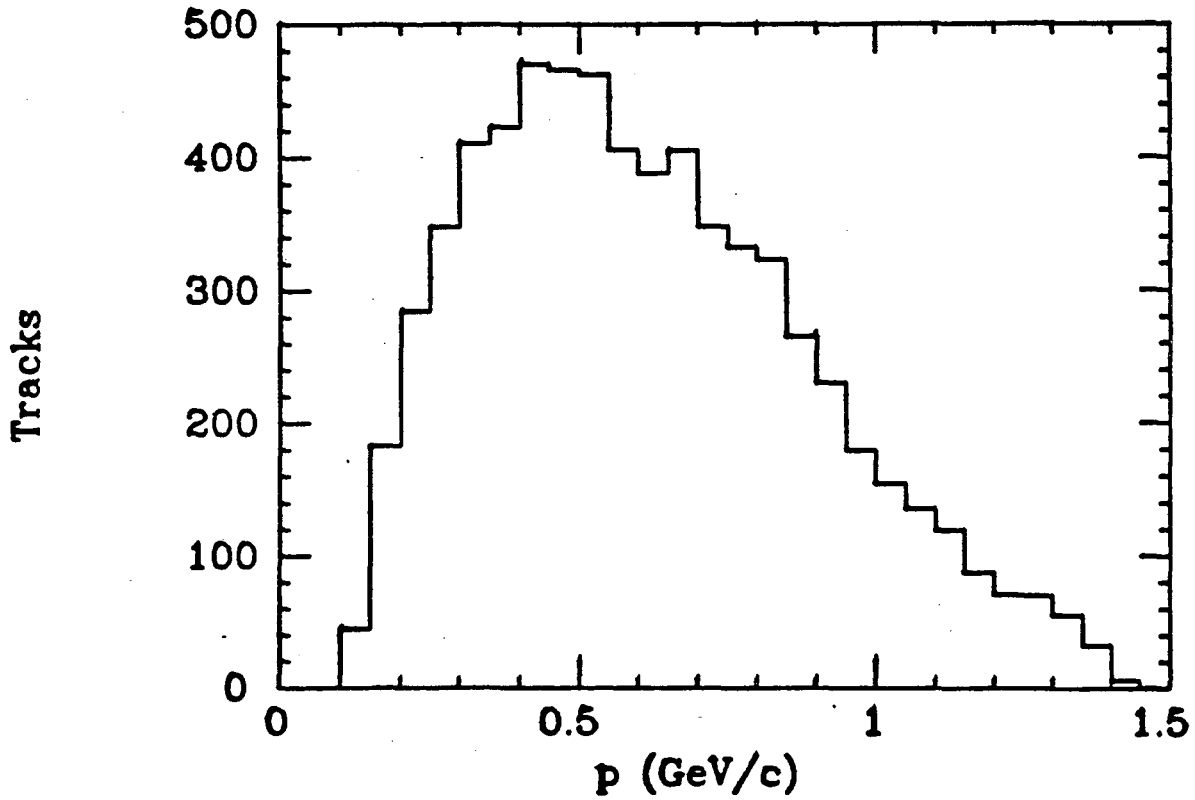

Figure 3.4: Pion momentum spectrum from $\psi \rightarrow 2(\pi^+\pi^-)\pi^0$

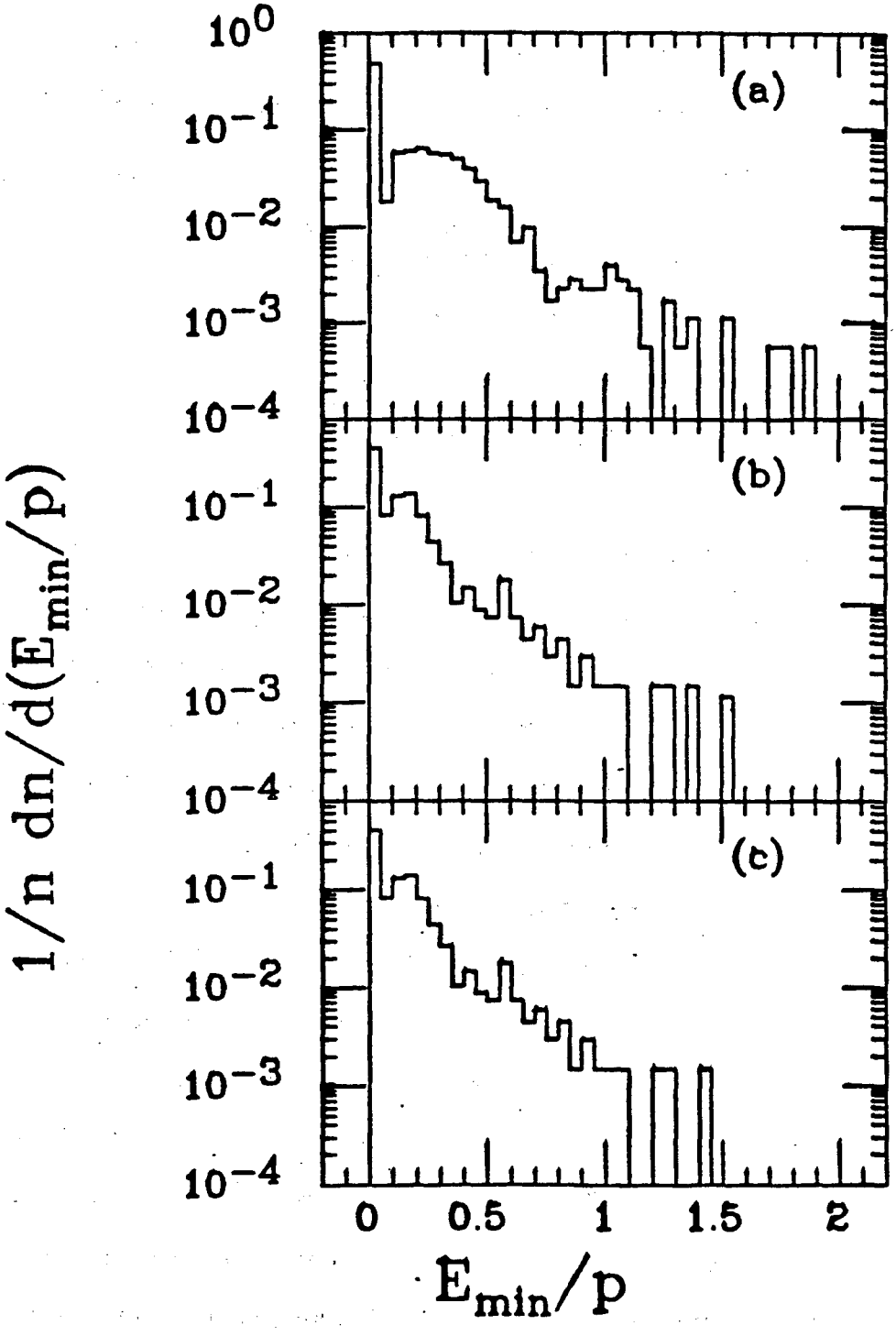

Figure 3.5: E_{min}/p for pions from $\psi \rightarrow 2(\pi^+\pi^-)\pi^0$
(a) $0.50 < p_\pi < 0.75$ GeV/c
(b) $0.75 < p_\pi < 1.00$ GeV/c
(c) $p_\pi > 1.00$ GeV/c

Pions from Beam Test Data:

In this data sample several thousand 2 and 4 GeV pion interactions were recorded in a partially instrumented LA calorimeter module. In order to apply the electron identification algorithm to this data sample it was necessary to:

1) Determine the position of the pion beam for each calorimeter coordinate (F,T,and U).

2) Adjust the layer to layer normalizations to correspond to those observed in the PEP data.

3) Determine the overall energy normalization to convert deposited to incident energy.

Step 1) was accomplished by plotting the energy weighted mean position in each layer. This mean value was then taken as the projected coordinate for each event, thus simulating the projection of the DC tracks into the LA module. Step 2) was accomplished by looking at the mean minimum ionizing energy deposited in each coordinate. The layer to layer corrections necessary to reproduce PEP data were of the order of 10%. Step 3) was accomplished by adjusting the minimum ionizing peak to agree with that observed in the PEP data.

A small correction to the pion misidentification probabilities must be applied to account for the different amount of material preceding the calorimeter module. The test beam data was taken with 1 X_0 of aluminum in front of the LA module. At PEP there is a 1.3 X_0 magnetic coil in front of the LA modules. Showers from charge exchange interactions which take place in the coil often look very electron-like, since the electromagnetic shower starts developing near the front of the LA module. Thus it is important to reproduce the effects of the coil in measuring the misidentification. Because of the way the layers are

ganged in depth and the way they are combined in the electron algorithm, it is not necessary for the charge exchange to occur in the coil in order for the shower to look electron-like. To be misidentified, it can occur anywhere within about the first few radiation lengths of the calorimeter. Thus the correction to the test beam data for having 0.3 X_0 less material in front of the calorimeter is on the order of 10%. Figure 3.6 shows the E_{min}/p distributions for the 2 and 4 GeV test beam data. The misidentification probabilities are shown in Table 3.3.

momentum	data sample	# tracks	# misid	misidentification probability
0.50 – 0.75	ψ data	1751	16	.009 ± .002
0.75 – 1.00	ψ data	1193	11	.009 ± .003
1.00 – 1.30	ψ data	680	3	.005 ± .003
2.0	beam test	3602	22	.006 ± .001
4.0	beam test	5181	19	.004 ± .001

Table 3.3: Pion misidentification probabilities.

Figure 3.7 summarizes the pion misidentification measurements from the beam test and SPEAR ψ data. The line on the plot is the best straight line fit to the data and is given by:

$$misid = .0075 - .0060 * \log_{10}(p_\pi)$$

Clearly, this is not the correct functional form of the misidentification probability. However, it serves as a guide to estimate the misidentification in the range of ≃ 500 MeV/c up to ≃ 5 GeV/c.

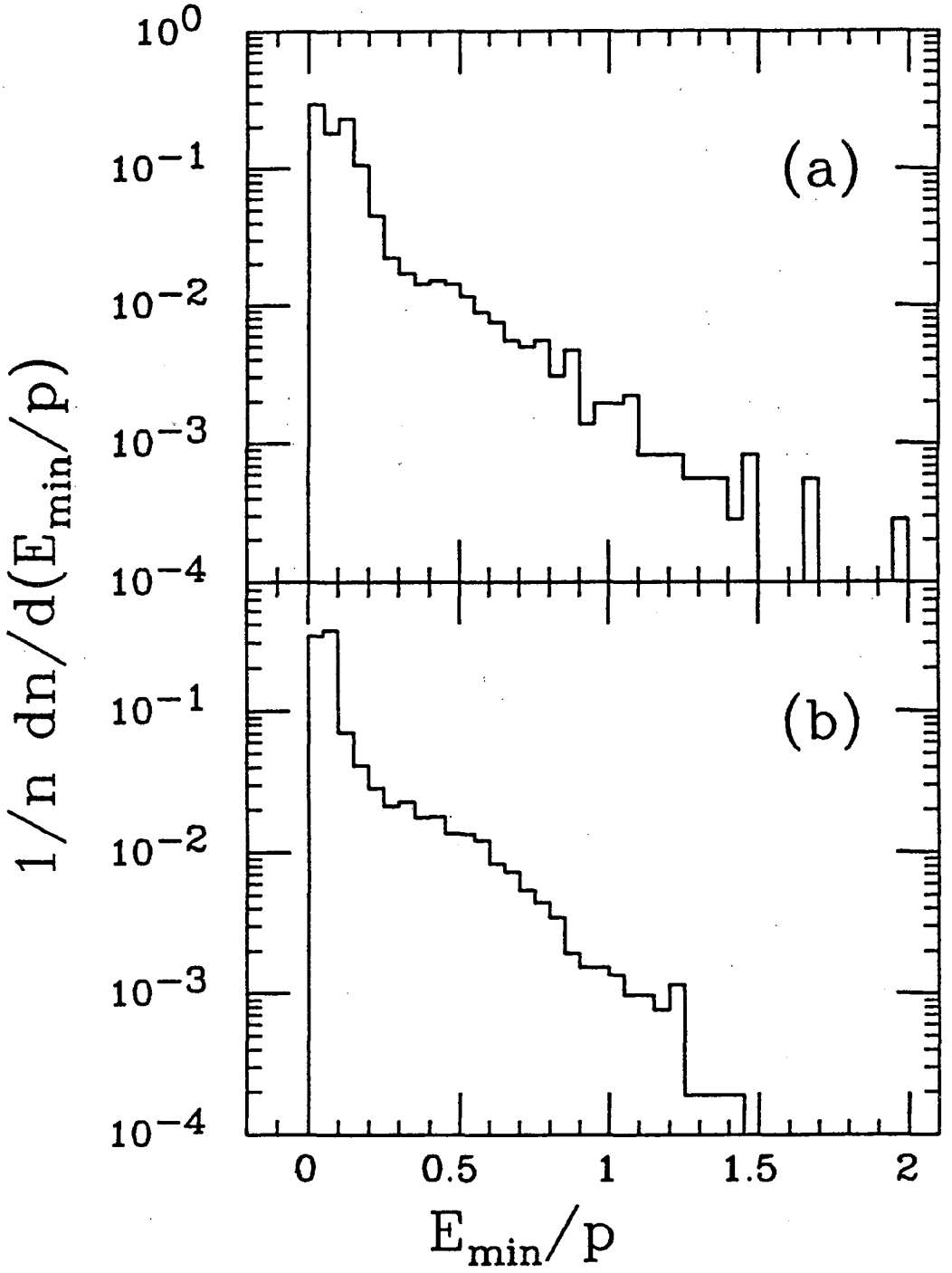

Figure 3.6: E_{min}/p for pions from the test beam data
(a) p_π = 2 GeV/c
(b) p_π = 4 GeV/c

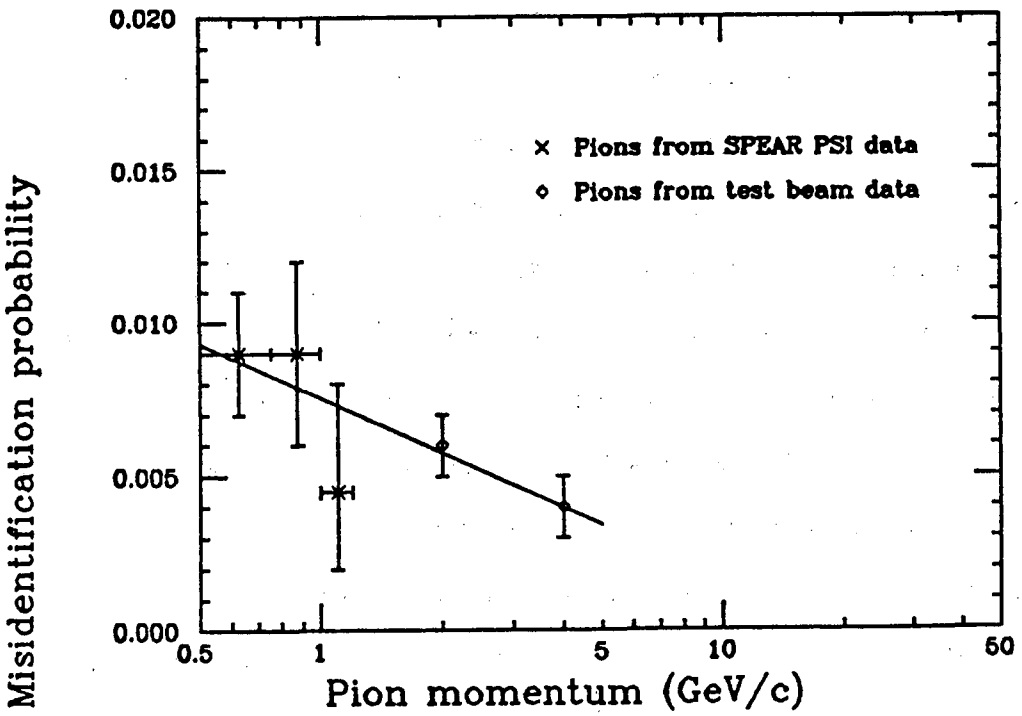

Figure 3.7: Pion misidentification vs. momentum

Pions from $K_s^0 \rightarrow \pi^+\pi^-$ at PEP.:

The K_s^0 data includes the effect of track overlap since the K_s^0's are produced in the middle of jets. K_s^0's were selected by constraining oppositely charged pairs of tracks to a vertex and requiring an invariant mass and flight path consistent with the K_s^0 hypothesis. The calculated misidentification probability is 0.022 ± 0.006. This value is three to four times larger those shown in Table 3.3 which were based on the ψ and pion test beam data. This is primarily due to the effects of track overlap mentioned above. Also, there is ≈ 10% background from non-K_s tracks in the resulting sample, which would mean a possible electron contamination on the order of ≈½%.

Pions from τ Pair Events at PEP.:

The τ pair events are interesting because the "$\tau \rightarrow$ 3 charge prongs" decay provides an easily identifiable source of multi-GeV pions in the PEP data. This topology is most easily recognized when the other τ in the event decays into a single charged prong resulting in a "1+3" event topology. Unfortunately there are not enough such events to measure the misidentification probability precisely. Furthermore, there is a relatively large systematic uncertainty in the measured probability which is due to differences in the neutral energy component (i.e. $\tau \rightarrow$ 3 prongs + neutrals) relative to hadronic events. This effect results in an absolute uncertainty in the misidentification probability that is on the order of 1%. Since this 1% limit is larger than the expected misidentification determined from the other methods, the τ data simply provides a consistency check for those results. The results from the first 15 pb^{-1} data show 3 out of 277 pions misidentified as electrons.

Of these 3, 2 appear to have overlapping photons because the LA energy is much greater than the momentum measured in the drift chamber. This leaves 1 out of 277 pion with an electron-like shower, giving a misidentification < 1.4% at the 90% C.L., ignoring systematic errors.

Track overlap:

The misidentification probability as a function of momentum in an uncrowded environment (i.e. no track overlap) was shown in Figure 3.7. The jet topology of PEP hadronic events however results in a much more crowded environment due to the large number of nearby photons and charged tracks. In this situation, the misidentification probability can be much larger than shown in Figure 3.7. Consider, for the moment, a hypothetical charged particle that conveniently stops losing energy as soon as it enters a calorimeter module. If this particle were in a jet event at PEP and the electron identification algorithm were applied, it is likely that some energy would be associated with the track, even though the track itself deposited no energy. The associated energy would come from other particles in the jet that deposited energy on the strips within the search region. Because of the strip geometry of the LA modules, the overlap only needs to occur in one coordinate (F,T or U) in order to contribute. If there were enough energy associated in every coordinate, it would be possible for this hypothetical particle that deposited no energy to be called an electron.

A scheme for simulating such a hypothetical particle was devised in order to study the overlap problem in the PEP events. The scheme relies on the fact that, in general, a hadronic event consists of two back-to-back jets. The orientation of the two jets can be characterized

by a single axis such as the thrust axis. The deposited energy density tends to be peaked along this axis and decreases farther away from the axis. Thus we can imagine that the average energy density is described by some function which depends only on the angle relative to the axis. If we consider taking a charged particle trajectory from one jet and "flipping" it 180°, the new trajectory will point into the opposite side jet. The new projection is into a region of the calorimeter which has the same relative angle with respect to the axis as before. This new region will have, on the average, the same energy density as the region the track originally came from. There will, of course, be no energy in the second jet corresponding to the energy lost by the original track. Thus the "flipped" track simulates the hypothetical one described above.

The statements just made about the equivalent average energy densities of the two jets are not rigorously correct. In particular, there is an effect which tends to give a higher energy density in the opposite side jet. This is simply due to the fact that the opposite jet has essentially the full beam energy available while the remainder of the same-side jet has the beam energy less the candidate track energy. This difference is not very important for a 1 GeV/c track in a 14.5 GeV jet, but the effect can be substantial for tracks of higher momentum. Fortunately, the high momentum region where this systematic effect is important is the region where the misidentification is dominated by the shower contribution and the overlap effect is almost negligible.

In order to study the effects of overlap on hadron misidentification, charged tracks from hadronic events were "flipped" as described above and the electron identification algorithm was applied to

the energy associated with the "flipped" track. The number of tracks in each $p,p_\perp$ bin that had $E_{min}/p > 1.1$, after the flip, was divided by the total number of tracks in that bin, to obtain a misidentification probability from overlap. To first order, the total misidentification probability is the sum of the misidentification probabilities from the overlap study and the "clean" pion shower studies. The first entry in each bin of Table 3.4 is the resulting sum as just described.

This procedure may underestimate the total misidentification probability. It is possible for the sum of the overlap energy plus the shower energy to be sufficient to make a hadron look electron-like, without the overlap or shower energy alone being sufficient to do so. In order to study the combined effect, a file was created which contained measured energy depositions from known pion interactions. A new overlap study was then made in which the track flipping scheme was used to obtain a sample overlap energy and the data file was used to obtain a sample pion shower. The overlap and shower energies were added together in each calorimeter coordinate. The electron identification algorithm was then applied to the summed energies. This method thus simulates the combined effect of overlap and shower contributions. The file of pion showers was created using known pions from the SPEAR ψ data. Since these pions have momenta less than about 1.3 GeV/c, a scheme for simulating pions of higher momenta had to be implemented. In order to do this, two simple scaling rules were used as explained below.

The deposited energy distributions for pion interactions consist of a minimum ionization region in which the energy deposited is independent of momentum, a charge exchange interaction region where the deposited

energy is roughly equivalent to the incident momentum, and an intermediate region which has a more complex momentum dependence. In order to carry out our study, two simple scaling schemes were used, neither of which correctly reproduced the full distribution. The first scheme took the pion showers from the file and did not rescale their energies before adding them to the overlap energies. This approach reproduced the contributions from the minimum ionizing part of the distribution, but underestimated the contributions from the momentum dependent tail. The results of this scheme are the second entries in each bin of Table 3.4. The second scheme was to rescale the deposited energies by the ratio of the momenta of the chosen track and the pion which actually created the interaction. This scheme reproduced the effects of the momentum dependent tail, but overestimated the effects from the minimum ionizing region. The results of this scheme are the third entries in each bin of Table 3.4.

We now have three different estimates of the misidentification probability, each of which we suspect is either systematically high or low. We must extract an overall probability for each bin, as well as an estimate of the systematic error on that probability. For the bins with $p_\perp > 1.0$, overlap plays a negligible role and the probabilities assigned for those bins are taken directly from Figure 3.7 . For the other bins a simple average of the results from the three methods is used and an estimate of the error is made based on the difference between the highest and lowest results obtained by the various methods. Finally, a few bins whose values do not seem to fit well with the general $p,p_\perp$ trends are adjusted slightly (by no more than .002) to give smooth

variations with p and $p_\perp$. The results of this procedure and the assigned errors are shown in Table 3.5

We can now calculate the expected background contribution from misidentified hadrons. Table 3.6 shows the number of charged tracks in the hadronic event sample that passed all of the necessary quality and fiducial cuts to be an electron candidate, but had $(E_{min}/p) < 1.1$. This sample is made up of about 65% pions, 20% kaons, 10% protons, 5% muons, and a few non-identified electrons. All non-electrons can potentially be misidentified as electrons. The different particle species have different hadronic interaction properties, but they are all equally effected by random energy overlap. We will compute the electron misidentification probability for these tracks as if they were all pions (i.e. using Table 3.5). In doing so we introduce a small systematic error that is proportional to the fraction of non-pion tracks times the percentage difference in the pion and non-pion misidentification probabilities. We have estimated that 35% of the tracks are non-pions. Since a large part of the misidentification arises from track overlap, we do not expect a large difference between pion and non-pion misidentification probabilities. Even if the difference were as large as 50%, it would only introduce an systematic error of $\simeq$ 18% which is small in comparison to the 50% systematic error we assigned to the pion misidentification probabilities themselves. Table 3.5 gave the probability $P(\pi \rightarrow e)$, as a function of p and $p_\perp$, that a pion would be misidentified as an electron. We obtain the expected background from misidentified hadrons by multiplying the number of observed hadrons in each bin of Table 3.6 by $P(\pi \rightarrow e)/[1-P(\pi \rightarrow e)]$. The result of this calculation is shown in Table 3.7

P\PT	0.00	0.50	1.00	1.50
1.0	.016 ± .003	.008 ± .003	.007 ± .003	.007 ± .003
–	.023 ± .002	.006 ± .001	.000 ± .002	.000 ± .020
2.0	.030 ± .002	.011 ± .002	.003 ± .002	.010 ± .020
2.0	.011 ± .003	.008 ± .003	.006 ± .003	.006 ± .003
–	.009 ± .002	.003 ± .001	.000 ± .004	.001 ± .004
3.0	.024 ± .003	.014 ± .003	.007 ± .004	.007 ± .003
3.0	.008 ± .003	.006 ± .003	.005 ± .003	.005 ± .003
–	.005 ± .002	.002 ± .002	.000 ± .006	.000 ± .006
4.0	.016 ± .004	.011 ± .004	.009 ± .006	.006 ± .006
>	.007 ± .003	.005 ± .003	.004 ± .003	.004 ± .003
4.0	.004 ± .002	.001 ± .002	.000 ± .005	.000 ± .007
	.016 ± .003	.014 ± .004	.000 ± .005	.016 ± .003

Table: 3.4 key

Sum of overlap misid + shower misid.

Result of "flipping" showers without rescaling energy.

Result of "flipping" showers and rescaling energy so energy ∝ momentum.

Table 3.4: Misidentification probability estimates including overlap.

P\PT	0.00	0.50	1.00	1.50
1.0	.023 ± .008	.010 ± .005	.007 ± .003	.007 ± .003
2.0	.015 ± .008	.008 ± .005	.007 ± .003	.007 ± .003
3.0	.010 ± .005	.006 ± .003	.005 ± .002	.005 ± .002
4.0	.007 ± .003	.005 ± .003	.004 ± .002	.004 ± .002
5.0	.007 ± .003	.005 ± .003	.004 ± .002	.004 ± .002
6.0	.006 ± .003	.004 ± .003	.003 ± .002	.003 ± .002

Table 3.5: Overall Pion misidentification probability

P\PT	0.00	0.50	1.00	1.50
1.0	10952.	5662.	1481.	169.
2.0	4104.	2633.	707.	445.
3.0	1911.	1329.	363.	269.
4.0	923.	696.	231.	176.
5.0	484.	369.	141.	95.
6.0	657.	565.	200.	228.

Table 3.6: Hadrons (non-electrons) in electron fiducial volume.

P\PT	0.00	0.50	1.00	1.50
1.0	241. ± 88.	57. ± 28	10. ± 4.4	1.2 ± 0.5
2.0	62. ± 33.	21. ± 13.	4.9 ± 2.1	3.1 ± 1.3
3.0	19. ± 10.	8.0 ± 4.0	1.8 ± 0.7	1.3 ± 0.5
4.0	6.5 ± 2.8	3.5 ± 2.1	0.9 ± 0.5	0.7 ± 0.4
5.0	3.4 ± 1.5	1.8 ± 1.1	0.6 ± 0.3	0.4 ± 0.2
6.0	3.9 ± 2.0	2.3 ± 1.7	0.6 ± 0.4	0.7 ± 0.5

Table 3.7: Expected electron background from misidentified hadrons. The errors shown reflect the systematic uncertainties in the misidentification probabilities quoted in Table 3.5.

3.5 Electrons from γ conversions and Dalitz decays

In addition to the background from misidentified pions, there is a smaller background contribution from non-prompt sources of real electrons. The major contribution to this background comes from photons which pair convert in the material between the interaction point and the tracking chamber. A smaller contribution comes from the Dalitz decay of π^0's (i.e. $\pi^0 \rightarrow \gamma e^+e^-$). The branching ratio for the Dalitz decay is $\simeq$ 1.15%. Since each non-Dalitz π^0 decay produces two photons and since the pair production rate per unit distance is $\simeq 0.8/L_{rad}$, the number of

e^+e^- pairs expected from Dalitz decays is about the same as would be expected from pair conversions in 0.7% X_0 of material. There was $\simeq$ 9.3% X_0 of material in the first 15 pb^{-1} of this data sample and $\simeq$ 3.7% X_0 in the remaining 20 pb^{-1}. Thus Dalitz decays account for about 11% of the produced pairs in the full data sample.

It is possible to substantially reduce this contribution to the background by removing pairs of oppositely charged tracks which are consistent with a photon conversion or Dalitz decay topology. Such a pair finding procedure should be implemented in such a way as to maintain a high efficiency for "real" pairs, while minimizing the probability of finding "fake" pairs. A fake pair occurs when a prompt electron is accidently combined with an unrelated oppositely charged track in the same jet to form a pair candidate. The pair finding algorithm that was actually implemented is described below.

The pair finding algorithm combines each identified electron candidate with every oppositely charged track in the same event. For each of these track pairs, the following quantities are calculated:

- Δ_{xy} is the gap distance between the tracks in the XY-plane, at the point where they have the same ϕ.
- R_{xy} is the radius from the interaction point to the minimum gap point in the XY-plane.
- ΔZ_0 is the absolute difference in Z between the two tracks at the origin.
- $\Delta\theta$ is the absolute difference in the dip angle θ.

The definitions of these variables are illustrated in Figure 3.8. The distributions of Δ_{xy}, ΔZ_0, and $\Delta\theta$ are shown in Figure 3.9. Note that Δ_{xy} can be either negative or positive depending on whether or not the two tracks intersect. Potential pair candidates must have the absolute value of Δ_{xy} less than 0.015m. We make this cut relatively broad in

order to maintain a high efficiency for Dalitz decays. The pairs from such decays have small negative gap distances because the finite invariant mass of the pair results in a finite opening angle. A useful property of the variable Δ_{xy} is that it is relatively insensitive to track mis-reconstruction in the dip angle θ. This is in contrast to a variable like the invariant mass which can be large for real conversion pairs if one of the tracks has an improperly reconstructed dip angle. This point is important since the most probable mis-reconstruction for these tracks is in the dip angle θ rather than the azimuthal angle ϕ. One way to check the integrity of the dip information is to look at ΔZ_0, the absolute difference in z of the two tracks, at the origin. If this difference is reasonably large (> 0.10m) we assume that the dip information is incorrect and we make no further geometrical cuts. If ΔZ_0 is acceptable then the variable $\Delta\theta$ is required to be less than 120 mrad for pair candidates. In making the cut on ΔZ_0, we make the cut generous enough to accommodate the expected difference in z for two tracks of different momenta which convert at a large radius. This expected difference arises because the two track helices only match in z at the point where the photon materialized.

If a pair of tracks meets all of the geometrical criteria for a conversion or Dalitz pair then further tests are made on the second member of the pair to check its consistency with the electron hypothesis. For tracks with momenta less than 2 GeV/c, a test is made on the particles time of flight information if available. To be consistent with the electron hypothesis, the time of flight must be no more than 3 standard deviations later than the expected time for an

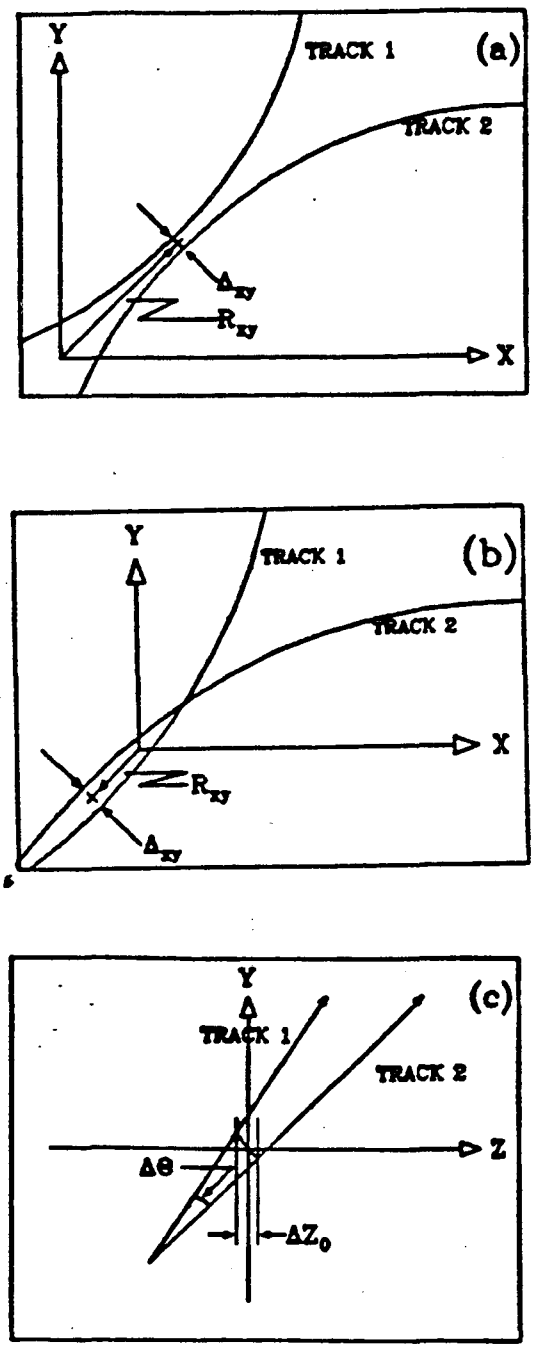

Figure 3.8: Definitions of pair finding variables
Examples illustrating (a) a positive gap distance (Δ_{xy}) and a positive radius of conversion (R_{xy}) and (b) a negative Δ_{xy} and a negative R_{xy}. Example (c) illustrates the dip angle difference ($\Delta\theta$) and Z difference at the origin (ΔZ_0).

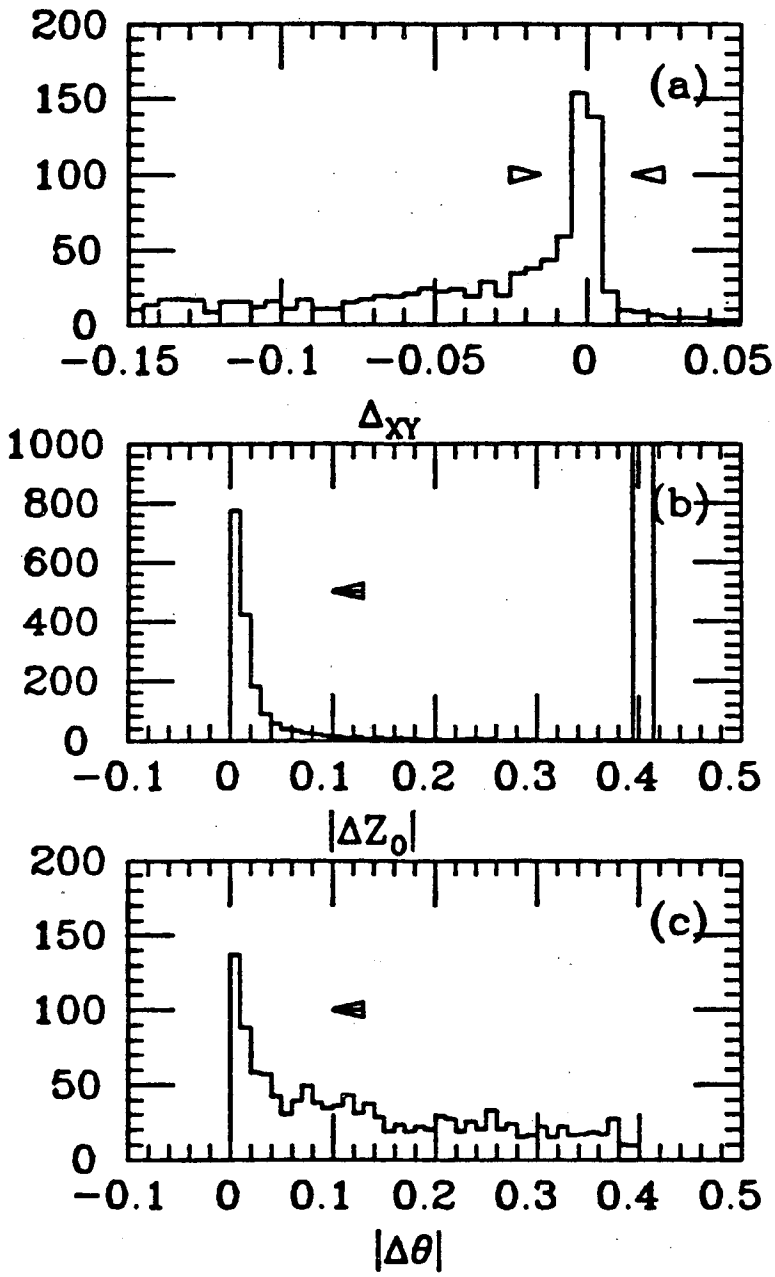

Figure 3.9: Distributions of pair finding variables
(a) Δ_{xy}; (b) $|\Delta Z_0|$; (c) $|\Delta\theta|$
The arrows illustrate the values of the cuts which select photon conversion pair candidates.

electron. For tracks of momenta greater than 0.7 GeV, a test is made based on the electron identification algorithm. To be consistent with the electron hypothesis, E_{min}/p must be greater than 0.5 if the track is within the electron fiducial volume. These cuts are > 98% efficient for electrons and reject a substantial fraction of hadrons. If the second track is inconsistent with the electron hypothesis, then the pair is considered to be "fake". Figure 3.10 shows the reconstructed radius of conversion for the real pair candidates. The structure of the material in the detector is clearly visible. Table 3.8 shows the number of electron candidates which are identified as belonging to real pairs in each p, $p_\perp$ bin.

P\PT	0.00	0.50	1.00	1.50
1.0	211.	46.	10.	0.
2.0	49.	22.	5.	1.
3.0	20.	6.	1.	4.
4.0	3.	4.	1.	0.
5.0	0.	3.	0.	2.
6.0	0.	3.	0.	1.

Table 3.8: Electrons belonging to real pairs.

The Monte Carlo was used to determine the efficiency for identifying real pairs as well as the probability for misidentifying a prompt electron by accidently forming a fake pair. The efficiency is determined as a function of the momentum of the observed electron candidate. For electrons in the range 1-2 GeV/c the algorithm finds 76% of the real pairs. The efficiency drops somewhat with increasing

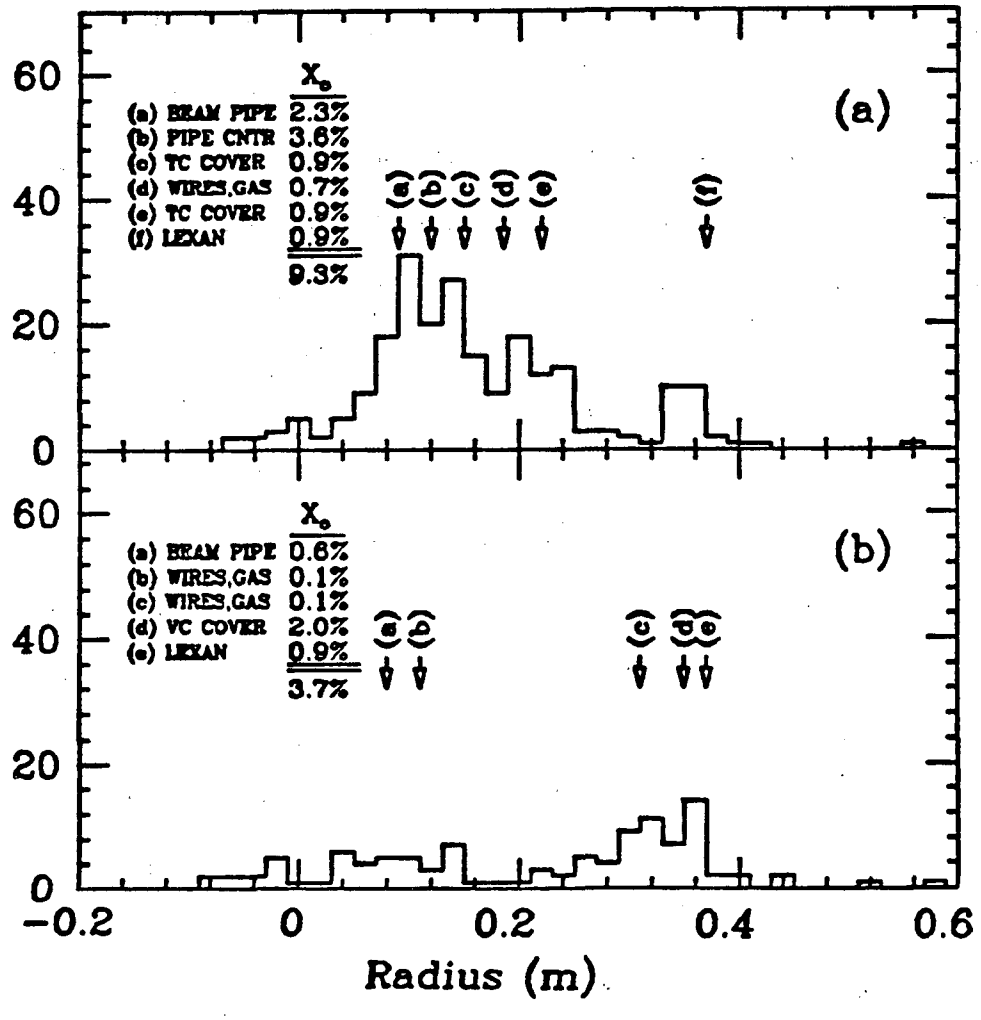

Figure 3.10: Radius of conversion (R_{xy})
(a) Data from 15 pb^{-1} with 9.3% X_0 total material.
(b) Data from 20 pb^{-1} with 3.7% X_0 total material.

observed electron momentum. For electrons above 6 GeV/c, the probability of correctly identifying a real pair is about 60%. The drop in efficiency occurs because high momentum photons often produce two high momentum electrons that share several cells in the innermost DC layers before the magnetic field can sweep them apart. These shared cells can result in one of the tracks being mis-reconstructed or unidentified by the track reconstruction algorithm. The probability that a prompt electron will form a fake pair with an unrelated track was determined to be ≈ 2%. The fact that the fake pair probability is so small is due in part to our ability to check the second track for consistency with the electron hypothesis.

There is another way to reject gamma conversions in th 20 pb^{-1} data sample taken with the vertex chamber. Electrons from photons which convert at the lexan or outer VC cover should have no associated signals in the vertex tracking chamber. In order to make use of this fact, all electron candidates that had signals in less that two out of seven possible vertex chamber layers were visually scanned to look for misreconstructed pairs or accompanying untracked low momentum tracks which curl tightly in the magnetic field and are missed by the track reconstruction algorithm. If there was no evidence of a potential second track that could form a pair with the original track, then the electron candidate was not removed from the sample. In practice ≈ 90% of the candidates without vertex chamber signals were actually removed. Table 3.9 below shows the number of candidates that were removed by this procedure in each $p,p_\perp$ bin. Since we know the number of pairs found by pair-finding algorithm and its efficiency, we can calculate the expected

P\PT	0.00	0.50	1.00	1.50
1.0	30. (28.)	9. (9.)	2. (1.)	0. (0.)
2.0	8. (7.)	5. (4.)	2. (1.)	0. (0.)
3.0	3. (3.)	1. (1.)	0. (0.)	0. (0.)
4.0	2. (0.)	1. (0.)	0. (0.)	0. (0.)
5.0	0. (0.)	0. (0.)	0. (0.)	0. (0.)
6.0	1. (0.)	0. (0.)	0. (0.)	1. (0.)

Table 3.9: Electrons removed with less than 2 VC cells. The leftmost number in each bin is the number actually removed. The numbers in parentheses show how many were expected to be removed.

P\PT	0.00	0.50	1.00	1.50
1.0	66.0	12.0	3.0	1.0
2.0	16.0	6.0	1.0	0.5
3.0	7.0	2.0	1.0	0.5
4.0	1.0	1.0	0.5	0.25
5.0	0.5	0.5	0.25	0.25
6.0	0.5	0.5	0.25	0.25

Table 3.10: Expected background electrons from unidentified pairs.

number of remaining unidentified pairs. Multiplying this number by the fraction of total material that occurs after the vertex chamber yields the expected number of pairs to be found in the hand-scan, assuming a 100% efficiency for the scan. The numbers in parenthesis in Table 3.9 are the results of that calculation. They agree quite well with the numbers of tracks actually removed.

After removing those electron candidates with missing vertex chamber hits, there is still a small residual contamination of electrons from unidentified gamma conversions and Dalitz decays. The expected remaining background can be calculated from the number of identified gamma conversions (Table 3.8) and the known efficiency of the pair finding algorithm. The results of the calculation are shown in Table 3.10.

4. MUON IDENTIFICATION

4.1 General philosophy

Muons can be distinguished from other stable charged particles by the nature of their interaction with matter. For muons with momenta greater than a few hundred MeV/c, this interaction is characterized by a relatively uniform rate of energy loss dE/dx due primarily to the ionization of atoms and molecules in the material. This pattern of energy loss is very different from the electromagnetic shower which characterizes an electron interaction. The difference arises because the relatively large muon mass suppresses the bremsstrahlung which initiates the electron-photon cascade process. Muon energy loss differs from that of pions, kaons, and protons because muons do not participate in the strong interaction. Although both muons and charged hadrons undergo the relatively uniform dE/dx energy loss, only the hadrons experience large localized energy loss due to nuclear interactions.

If a mixture of muons and other stable charged particles are incident on a sufficient amount of material, then almost all of the electrons and hadrons in the mixture will deposit their full energy in the material. Those muons which have incident energies greater than that which will be lost to dE/dx will penetrate the material. In a practical muon detector, the amount of material to be used as an absorber is therefore limited by the requirement that the muons of interest be able to penetrate the absorber. For a typical absorber like iron, the rate of energy loss dE/dx is about 200 MeV per interaction length. In the MARK II experiment we would like to have a low momentum cutoff in the 1 - 2 GeV/c range for incident muons. This implies that

we can only use ≈ 5 - 10 interaction lengths of absorber. With an absorber thickness in this range, a non-negligible fraction of incident hadrons will fail to interact strongly and will penetrate the muon system, thus simulating muons. In addition, some hadronic interactions in the absorber will create charged particle secondaries which penetrate the absorber, also simulating muons. Some rejection of these secondaries can be accomplished by obtaining spatial information about the penetrating tracks. Without this information, the occurrence of an hadronic interaction is not apparent until all of the charged secondaries have been absorbed. This limitation can be overcome by having sufficient spatial information to recognize the large-angle scatters and multi-prong topologies associated with hadronic interactions [35].

4.2 Implementation

The MARK II muon system, described in detail in chapter 2, consists of four walls located above, below, and on either side of the central detector. Each wall consists of four layers of alternating steel plates and planes of proportional tubes. Hits in the proportional tube planes signal the penetration of charged tracks through the absorber and provide spatial information about the location of the penetrating tracks. The total amount of material traversed by a charged particle at normal incidence is ≈ 2.6, 4.0, 5.8, and 7.4 interaction lengths for levels 1-4 respectively. The muon identification algorithm involves extrapolating a charged particle trajectory, as measured by the central drift chamber, through the absorbing walls and then looking for hits in the proportional tube planes that are consistent with the expected range

and multiple scattering for the incident track. In the extrapolation process, expected dE/dx losses, multiple Coulomb scattering, and bending in the magnetic field (some of the absorber serves as a flux return) are taken into account.

In practice, each drift chamber track in an event is extrapolated into the muon system and a search is made for proportional tube hits within 2σ of the non-scattered extrapolation. Here σ is the rms extrapolation error arising from multiple scattering and the drift chamber tracking resolution. A variable MUSTAT is formed which contains a bit pattern corresponding to the levels which had such hits. The lowest order bit of MUSTAT corresponds to a hit in the first level of the muon system. A track which had an associated hit only at the first level would thus have MUSTAT = $1 = 0001_2$. A track which had associated hits in all four levels would have MUSTAT = $15 = 1111_2$. Figure 4.1 shows the MUSTAT distribution for all tracks in the muon system fiducial volume (more on how this is defined in section 4.3).

Multiple Coulomb scattering:

The primary contribution to the extrapolation error σ comes from multiple Coulomb scattering in the magnetic coil ($\simeq 1.3\ X_0$), the calorimeter modules ($\simeq 16\ X_0$), and hadron absorbers ($\simeq 13\ X_0$ per level) which precede the proportional tube planes. The mean-squared radius distribution relative to the non-extrapolated trajectory, after passing through an absorber of thickness t_0 and a drift space of distance d_0 is given by [36]:

$$\sigma_r^2 = \theta_0^2(t_0^2/3 + t_0 d_0 + d_0^2) \qquad (4.1)$$

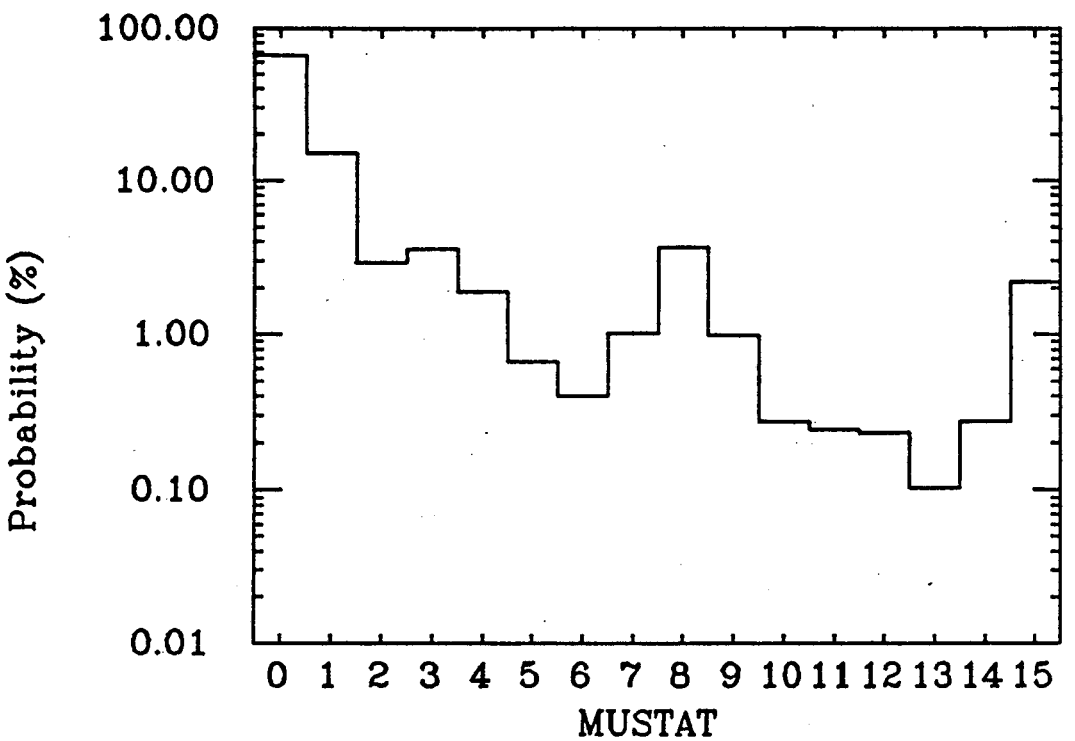

Figure 4.1: MUSTAT distribution for muon fiducial volume tracks MUSTAT contains a bit pattern which corresponds to the levels in which associated proportional tube hits were found. The populations are expressed in terms of the "per track probability."

where θ_0 is the rms scattering angle in the Gaussian approximation. In this approximation, θ_0 is given by [37]:

$$\theta_0 = \frac{21 \text{ MeV}}{p(\text{MeV})\ \beta} \left[\frac{t_0}{L_{rad}}\right]^{\frac{1}{2}} \tag{4.2}$$

where p and β are the momentum and velocity of the incident particle, t_0 is the amount of absorber traversed, and L_{rad} is the radiation length of the absorber.

A particle typically traverses several detector elements, each at different distances from the proportional tube planes. The effects of each element are independent and the contributions can be added in quadrature. Since the proportional tube wires in each layer measure only one coordinate, say x, we are really interested in σ_x which is equal to $\sigma_r/\sqrt{2}$. Therefore, for the coordinate of interest we have:

$$\sigma_x^2 = \tfrac{1}{2} \sum_i \theta_i^2(t_i^2/3 + t_i d_i + d_i^2) \tag{4.3}$$

where θ_i, d_i, and t_i are the rms multiple scattering angle, distance to the detector plane, and thickness of element i respectively.

This component of the extrapolation error is combined in quadrature with the extrapolated drift chamber tracking error (typically $\simeq$ 3 cm) to obtain the overall extrapolation error σ used in defining MUSTAT. Figure 4.2 shows a plot of the measured deviation of proportional tube hits from the extrapolated trajectory divided by the σ_x calculated from Eq.#(4.3). If σ_x is properly calculated and if the distribution of deviations were actually Gaussian, then the normalized distributions should be unit width Gaussians as illustrated by the solid curves in Figure 4.2. These curves fit the data fairly well, indicating that we understand the extrapolation errors.

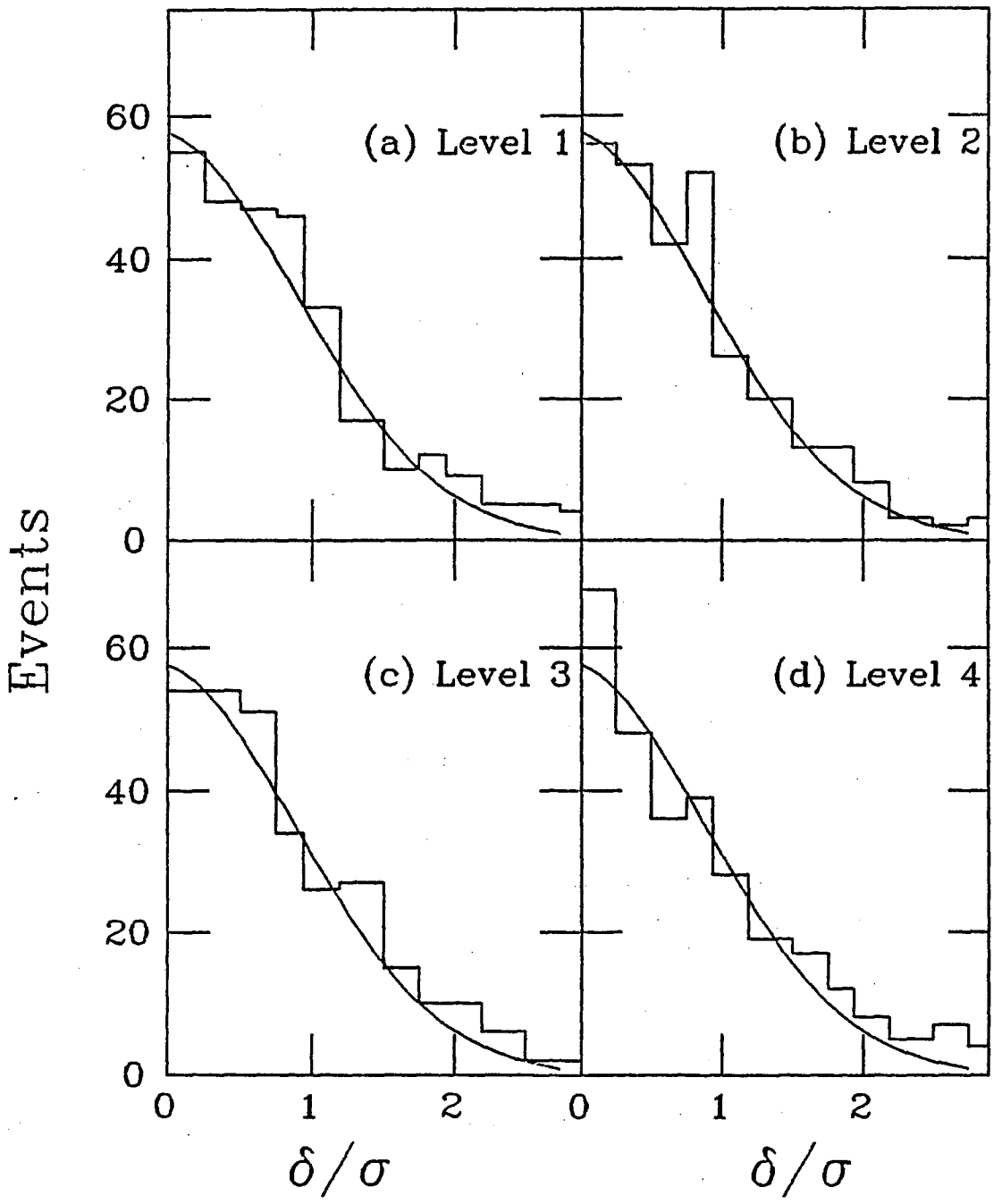

Figure 4.2: Measured deviation from extrapolated position divided by sigma

4.3 Muon identification efficiency

For the purposes of this analysis, muon candidates will be required to have MUSTAT=15 (i.e. to have a hit within 2σ of the extrapolation in all four levels of the muon wall). The possible sources of inefficiency include all those which could cause a real muon to be missing a hit in one or more levels. The various contributions will be discussed below.

Fiducial criteria:

Two obvious ways for a muon to fail the selection criteria are for it to have missed the geometrical acceptance of the muon system or for it to have had too little momentum to penetrate all four levels. In order to avoid the large inefficiency from these effects, we define fiducial criteria which eliminate most failures of this type. Muon candidates are required to have drift chamber track extrapolations which lie within the sensitive volume of the muon proportional tube planes. The solid angle subtended by the outermost proportional tube levels (the limiting case) corresponds to $\simeq$ 45% of 4π. Muon candidates are also required to have sufficient initial momenta to penetrate all four levels of the absorber. The calculation of the minimum momentum is based on the amount of expected dE/dx loss along the extrapolated trajectory. For a muon traversing the absorber planes at normal incidence, the minimum momentum required to penetrate all four levels is about 1.8 GeV/c. For other angles of incidence, more material is traversed, and correspondingly larger momenta are necessary to penetrate all levels. These two criteria, that the muon candidate extrapolate into the sensitive volume and that it have enough momentum to penetrate all four levels, are expressed in MARK II software notation as MULEVE=4. MULEVE

translates as "number of muon levels expected". In this analysis muon candidates must have MULEVE=4 and an incident momentum p > 2 GeV/c.

Multiple scattering losses:

Since real charged particles do not exactly follow the calculated extrapolations through the muon system, it is possible for actual muon trajectories to lie outside the 2σ search region. Multiple scattering near the edges of the fiducial volume can result in tracks being scattered out of the sensitive region. The inefficiency resulting from such scattering is greater for lower momentum tracks since they have a larger rms scattering angle. Muons can also scatter out of the 2σ search region while remaining within the sensitive volume. The inefficiency from this effect is momentum independent, since the differences in the rms scattering are included in the calculation of σ.

Range straggling losses:

Because of the statistical nature of the ionization energy loss process, variations in dE/dx result in fluctuations in range. A measure of this variability is the percentage range straggling which is defined as the ratio of the rms variation in range to the expected range. In the momentum range of interest (2-14.5 GeV/c) this percentage range straggling varies between ≃ 3 - 6%. For further details, see the numerical calculations presented by Sternheimer [38] and experimental measurements in the MARK II detector by Hayes [33]. Range straggling can result in fluctuations in energy loss which result in the muon ranging out before penetrating all layers, thus failing the muon selection criteria.

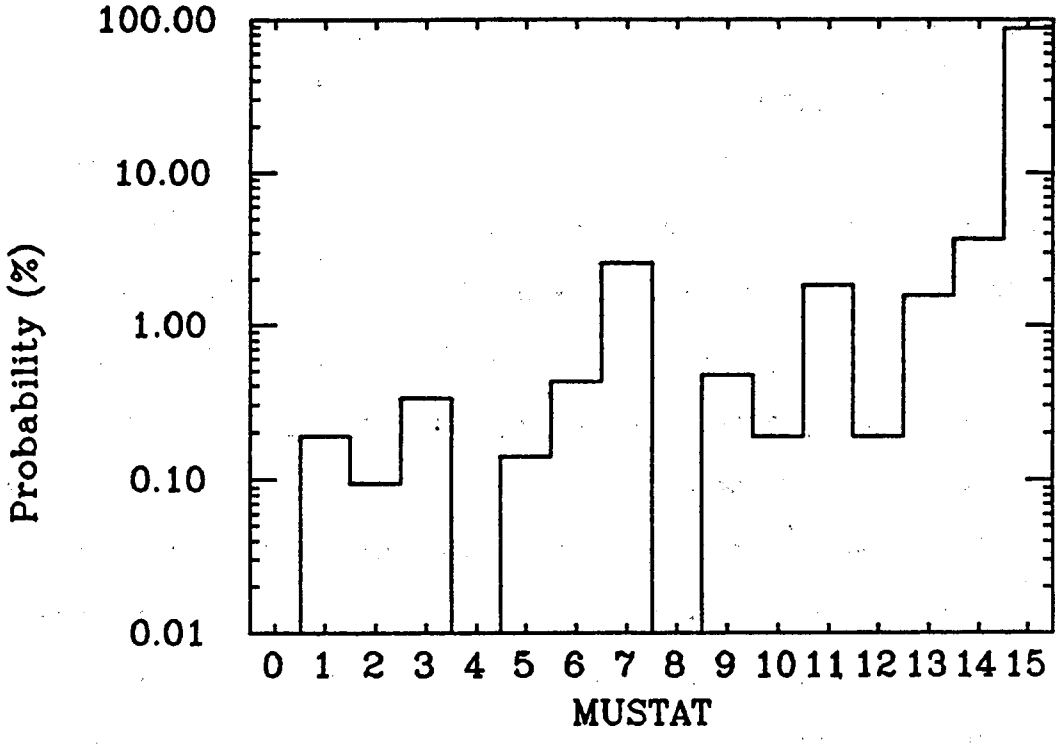

Figure 4.3: MUSTAT distribution for muons from $e^+e^- \rightarrow \mu^+\mu^-$
This distribution is used to determine the proportional tube efficiencies in the muon system. The populations are expressed in terms of the "per track probability."

Proportional tube efficiencies:

A muon track may be missing a hit at a particular proportional tube plane because of electronic inefficiency. In order to study this effect, a sample of $e^+e^- \rightarrow \mu^+\mu^-$ events ($p_\mu \simeq 14.5$ GeV/c) were studied. Figure 4.3 shows the MUSTAT distribution for such muons that were within the muon system fiducial volume. The populations at MUSTAT=14, 13, 11, and 7 correspond to single missing hits in levels 1-4 respectively. From these populations we estimate the inefficiency to be (3±1)% per track per level.

Extrapolation error:

A muon track that is improperly reconstructed in the central drift chamber can fail the identification criteria because the track extrapolation is more than 2σ away from the proportional tube hits left by the muon. It is more likely that a track will be mis-reconstructed in the polar angle θ rather than the azimuthal angle ϕ. This occurs because the polar angle is determined from the ± 3° stereo layers in the drift chamber, whereas the azimuthal angle is determined by the axial layers. The proportional tubes in level 1 of the muon system measure the polar angle θ while levels 2-4 measure the azimuthal angle ϕ. Therefore, mis-reconstructed muons will often not have an associated hit in the first level because the extrapolation misses in θ.

Monte Carlo determination of efficiency:

All of the effects described above have been incorporated into a detailed Monte Carlo simulation program. From this program, the acceptance and identification efficiencies for muons have been determined as a function of momentum. Table 4.1 below shows the

identification efficiency for muons in the muon fiducial volume. The momentum dependence is due to the multiple scattering losses near the edges of the fiducial volume and range straggling losses. Both effects tend to decrease the efficiency at lower momenta.

P\PT	0.00	0.50	1.00	1.50
2.0	0.78	0.78	0.78	0.78
3.0	0.82	0.82	0.82	0.82
4.0	0.86	0.86	0.86	0.86
5.0	0.90	0.90	0.90	0.90
6.0	0.92	0.92	0.92	0.92

Table 4.1: Muon identification efficiency

4.4 Hadron misidentification probability

Hadron misidentification can occur when a hadron fails to interact strongly in the absorber and penetrates all four levels of the muon system. Misidentification can also occur when a nuclear interaction in the absorber does take place if some of the interaction secondaries penetrate all four levels. It is also possible for misidentification to arise from hits which were actually caused by random noise or by the penetration of other nearby tracks.

Muon system noise:

Random hits in the muon system can arise from either purely electronics related noise ("hot channels") or actual physical processes (cosmic rays, synchrotron radiation) which fire the proportional tubes. The effects of random noise in the muon system were measured by combining muon system raw data from bhabha events ($e^+e^- \rightarrow e^+e^-$) with the central detector data from hadronic events. Since bhabha events contains no penetrating tracks, the corresponding muon system raw data contains only noise hits. Figure 4.4 shows the MUSTAT distribution obtained by combining charged tracks from hadronic events with the random muon hits. The fourth level has the most noise, as can seen by looking at the MUSTAT = 8 = 1000_2 bin. About 5% of all charged tracks in the muon fiducial volume have a random hit in this level. None of the "noise" tracks satisfy our muon criterion of MUSTAT=15, primarily because of the low noise levels in the inner levels. The noise can contribute to the hadron misidentification probability however, as in the case of a hadron which only penetrates to the third level but which also has a noise hit in the fourth.

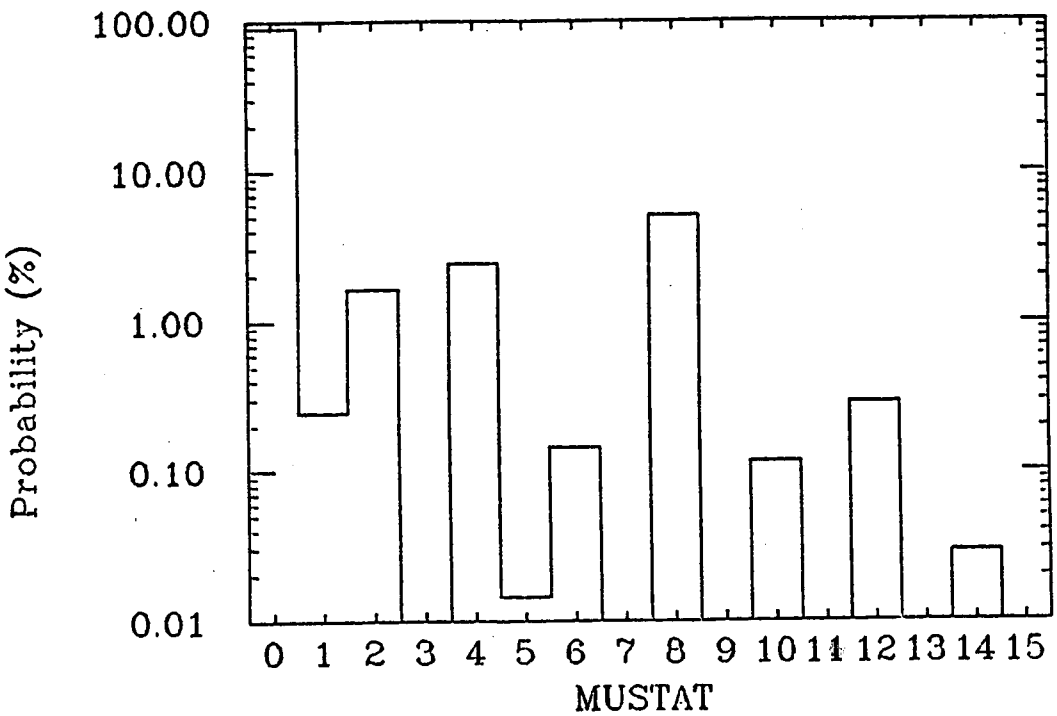

Figure 4.4: MUSTAT distribution from random background. This distribution is used to determine the proportional tube "noise" in the muon system. The populations are expressed in terms of the "per track probability."

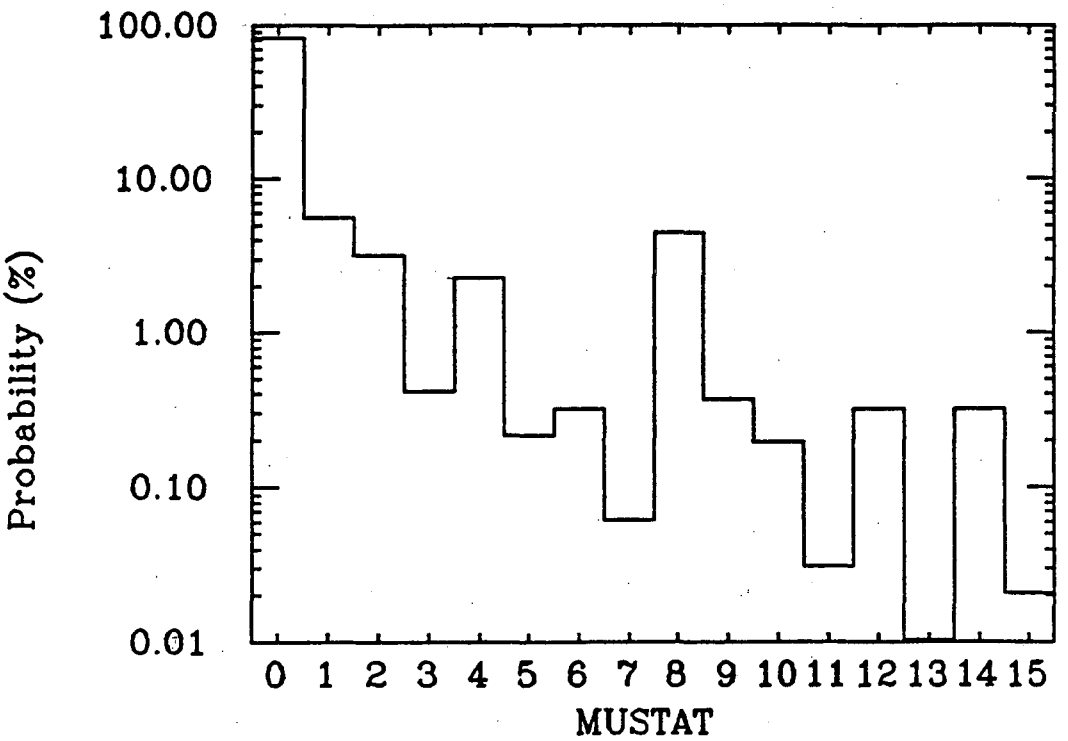

Figure 4.5: MUSTAT distribution for "flipped" tracks
This distribution is used to determine the combined effects of track overlap and noise. The populations are expressed in terms of the "per track probability."

Another source of random hits are those caused by other penetrating tracks in the event. These other tracks can be either muons or hadrons that have punched through into the muon system. Because of the jet topology of the hadronic events it is quite common for the 2σ search regions around the charged track trajectories in a jet to overlap. In order to study this effect, the following algorithm was used. Tracks in a hadronic event were reversed in direction and projected into the muon system on the opposite side of the event. The muon identification algorithm was then applied to the "flipped" track. The resulting MUSTAT distribution is shown in Figure 4.5. Note that in addition to the "noise" populations (cf. Figure 4.4) there are now substantially larger populations in the MUSTAT=1 and MUSTAT=14 bins. These values of MUSTAT correspond to track overlap in the θ and ϕ coordinates respectively. The fact the MUSTAT=1 represents a single associated hit and MUSTAT=14 represents three associated hits is a consequence of the wire orientation of the four proportional tube levels.

Hadron punchthrough:

Hadron punchthrough results when a hadron or a secondary from its nuclear interaction in the absorber penetrates into the muon detector. Figure 4.6 illustrates this effect with data from the SLAC 20 spectrometer [39] as reanalyzed by Harris et al.[35]. In this figure, the ordinate gives the fraction of incident pions that generate penetrating radiation. The momentum dependence of this fraction is due to the fact that the reaction secondaries penetrate deeper as the incident energy increases. The slopes for various incident momenta, however, are almost identical because the pion-nucleon cross section is

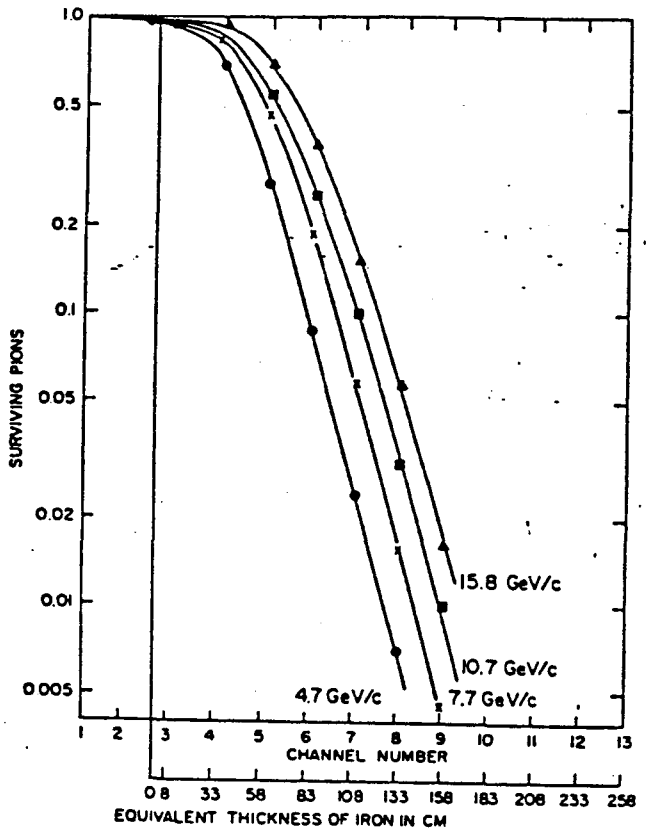

Pion range data from the SLAC 20 GeV spectrometer. The ordinate gives the fraction of the incident pions that generate penetrating radiation vs the absorber thickness in equivalent cm of iron. Because the reaction secondaries tend to penetrate deeper as the incident momentum increases, the curves shift to the right with increasing momentum. Ultimately, however, the slopes become similar for different incident momenta, a consequence of the fact that the original pion-nuclear reaction cross section is relatively constant over this momentum range.

Figure 4.6: Pion range data from the SLAC 20 GeV spectrometer This figure in taken from Reference [35].

relatively constant over this momentum range. In the 20 GeV spectrometer experiment, no spatial information on the penetrating tracks is provided, thus the occurance of a hadronic interaction is not apparent until all of the interaction secondaries have been absorbed.

A muon detection system which provides spatial information on the penetrating tracks can have better pion rejection than that illustrated in Figure 4.6. Figure 4.7 shows the fraction of incident pions surviving within a circle expected to contain 96% of the incident muons based on a multiple Coulomb scattering calculation. This data comes from Harris et al.[35] which, like the MARK II, uses multiwire proportional chambers and iron absorbers. The slope of the curve in Figure 4.7 corresponds to an attenuation length of 16.6 cm as compared to $\simeq$ 21 cm for the curves in Figure 4.6. The 16.6 cm attenuation length corresponds to an effective "cross section" of 710 mb, which can be compared to a calculated cross section for iron of 725 mb obtained from π^+ data on copper at 3 GeV/c [40] assuming the inelastic cross section goes as $A^{2/3}$. The inelastic cross section is assumed to be the dominant process in separating pions from muons. The elastic part of the cross section also contributes to a small degree since the typical scattering angle ($\simeq$ 20 mrad) combines in quadrature with the multiple Coulomb scattering to yield a slightly wider distribution for non-interacting pions relative to muons.

We can use the data from these two experiments to estimate the punchthrough probabilities for the MARKII muon system. The arrangement of detector elements in the MARK II system gives it a sensitivity to interaction secondaries that lies between those illustrated in Figures

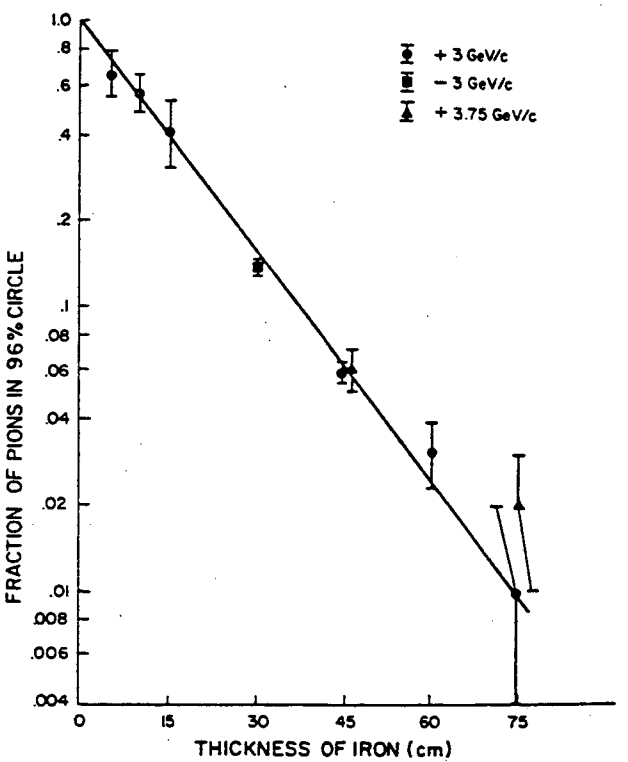

Fraction of the incident pions surviving within a multiple-Coulomb-scattering circle containing 96% of the incident muons, plotted as a function of the thickness of iron in cm.

Figure 4.7: Fraction of incident pions surviving within a circle containing 96% of incident muons.
This figure is taken from Reference [35].

4.6 and 4.7. Thus we expect that the pion attenuation length in the MARK II should lie between ≃ 17 and ≃ 21 cm of iron and that punchthrough to the fourth level of the muon system (≃ 130 cm Fe) should be less than ≃ 1%. With this information in hand we will now describe measurements of pion punchthrough using data from the MARK II detector.

MUSTAT distribution:

The MUSTAT distribution for all tracks in the muon fiducial volume was shown in Figure 4.1. Figure 4.5 showed the contributions to this distribution from random noise and overlapping tracks. In addition to the random and overlap hits, there should be contributions to the observed MUSTAT distribution from real muons and from hadron punchthrough. If we ignore electronic inefficiencies, multiple scattering outside of the search region, and range straggling then real muons will penetrate to the fourth level and have MUSTAT=15. Hadrons that penetrate the absorbers do not necessarily reach the fourth level, but are usually absorbed earlier. The populations of hadrons punching through to the various levels should have an attenuation length of 17-21 cm as we saw earlier. If we determine the number of tracks that penetrate to the first, second, and third levels, we can use the attenuation length to extrapolate to the fourth level. We cannot measure punchthrough to the fourth level directly because it is contaminated by the real muon signal, the magnitude of which is unknown.

Table 4.2 shows the contributions of three components (labelled "RAND", "MUON", and "PUNCHTHROUGH") to the observed MUSTAT distribution. The first component is due to random noise and overlapping hits. The MUSTAT distribution for this component, as measured by the "track

flipping" algorithm, is shown in the column labelled "RAND". The "OBSERVED" MUSTAT distribution (rightmost column of Table 4.2) differs from the "RAND" distribution because of the presence of penetrating tracks in the real data sample. Note, for example, the significant increases at MUSTAT=1,3,7, and 15 in the "OBSERVED" distribution relative to the "RAND" distribution. These values of MUSTAT primarily correspond to track penetration to levels 1-4 respectively. Since we select the tracks in our sample by requiring MULEVE=4 (i.e. the tracks are expected to penetrate all four level of the muon system under the muon hypothesis) we expect all real muons to penetrate all levels and thus have MUSTAT=15. This will not be rigorously true, however, since electronic inefficiency, multiple scattering, and range straggling can result in other values of MUSTAT. Muons from pion and kaon decays in flight can also contribute to the MUSTAT distribution. The expected contributions of both prompt and decay muons are shown in the column labelled "MUON". Since the total number of tracks must be conserved, the muon MUSTAT population must deplete other values of MUSTAT. For the most part ($\simeq$ 80% of the time) this depletion occurs at MUSTAT=0. Other values of MUSTAT are depleted in proportion to their frequency of occurance. This explains the existence of negative entries in column "MUON".

In determining the populations in column "MUON", the population at MUSTAT=15 is adjusted to be consistent with the "OBSERVED" MUSTAT=15 population, after including punchthrough effects. The "MUON" populations at other values of MUSTAT are based on Monte Carlo predictions which include the effects of hadron decay in flight,

MUSTAT	RAND	MUON	PUNCHTHROUGH 1	2	3	4	PREDICT	OBSERVED
0	7984.0	-193.6	-973.7	-254.0	-56.1	-15.9	6490.7	6444.0
1	541.0	-10.2	973.7	-9.3	-3.8	-1.1	1490.3	1469.0
2	310.0	-7.5	-37.8	-2.2	-2.2	-0.6	259.7	285.0
3	40.0	3.8	37.8	265.5	1.5	-0.1	348.5	349.0
4	222.0	-5.4	-27.1	-7.1	-1.6	-0.4	180.5	185.0
5	21.0	-0.4	27.1	-0.4	1.6	-0.0	48.8	65.0
6	31.0	-0.8	-3.8	-0.8	1.5	-0.1	27.1	39.0
7	6.0	22.5	3.8	8.3	59.1	0.5	100.1	98.0
8	432.0	-10.5	-52.7	-13.7	-3.0	-0.9	351.2	356.0
9	36.0	-0.7	52.7	-0.7	-0.3	-0.1	86.9	96.0
10	19.0	-0.5	-2.3	-0.2	-0.1	-0.0	15.9	27.0
11	3.0	5.6	2.3	14.6	0.1	0.5	26.2	24.0
12	31.0	-0.8	-3.8	-1.0	-0.2	-0.1	25.2	23.0
13	1.0	5.4	3.8	-0.0	0.1	0.5	10.7	10.0
14	31.0	8.6	-3.8	-0.9	-0.1	0.4	35.2	27.0
15	2.0	184.5	3.8	1.9	3.6	17.3	213.1	213.0
TOTAL	9710.0	0.0	0.0	0.0	0.0	0.0	9710.0	9710.0

Table 4.2: Determination of hadron punchthrough probabilities.

electronic inefficiency, multiple scattering, and range straggling. The magnitude in each bin is normalized with respect to the "MUON" MUSTAT=15 population.

Notice that the "MUON" population at MUSTAT=7 is non-negligible in comparison to the "OBSERVED" MUSTAT=7 population. The population at MUSTAT=7 is dominant in the determination of the punchthrough probability to level 3. If we had ignored the "MUON" component, we would have overestimated the level 3 punchthrough probability by about 20%.

The remaining contribution to the MUSTAT distribution comes from hadron punchthrough. The columns labelled "PUNCHTHROUGH" show the

corrections for punchthrough to levels 1-4. The corrections to the MUSTAT distribution for punchthrough to levels 1-3 were determined using a maximum likelihood fit to the "OBSERVED" distribution. The correction for level 4 was obtained from an extrapolation of the punchthrough probabilities from the first three levels. The fit procedure and correction algorithm are described below.

For each value of MUSTAT, a correction is applied based on the change that would occur if some fraction P_j of all incident tracks punched through to level j. For example if P_1 of all tracks punched through to the first level, then P_1 of the tracks that originally had MUSTAT=0 would move to MUSTAT=1. Similarly, P_1 of the tracks that had MUSTAT=2,4,6,... would move to MUSTAT=3,5,7,..., whereas those that originally had MUSTAT=1,3,5,... would not change, since they already contained a hit at level one. Similarly, if P_2 of all tracks punch through to the second level, then P_2 of the tracks that had MUSTAT=0,1,or 2 would move to MUSTAT=3. Those that originally had MUSTAT=3 would not change. Those that had MUSTAT=4, 5, or 6 would move to MUSTAT=7, etc.. The corrections that are shown in Table 4.2 were obtained by maximizing the likelihood for observing the "OBSERVED" populations for MUSTAT = 0 - 14. There were three free parameters in the fit, namely, the punchthrough probabilities P_j for levels 1, 2, and 3. The population at MUSTAT=15 was not included in the fit since it contains actual signal muons, whereas we only want to fit to hadron punchthrough. The fit results yield average hadron penetration probabilities P_j of (12.8±0.4)%, (3.3±0.2)%, and (0.9±0.1)% for levels 1 - 3 respectively. Extrapolating these values to the fourth level using

an attenuation length of ≃ 19 cm, predicts a punchthrough probability P_π ≃ (0.2±0.1)%.

This procedure reproduces the observed distribution quite well, as can be seen by comparing the columns labelled "PREDICT" and "OBSERVED". If we study the entries in the MUSTAT=15 row of Table 4.2, we will find that hadron punchthrough contributes about 29 tracks to the raw signal of 213. We will briefly discuss the various sources of these 29 background tracks. Starting with the column labelled "RAND" we see that random overlap and noise alone contribute 2 of the tracks. In the column labelled "PUNCHTHROUGH 1" there are 3.8 background tracks which are the result of punchthrough to level 1 combining with MUSTAT=14 noise hits to result in MUSTAT=15. In column "PUNCHTHROUGH 2" we see that punchthrough to level 2 combines with MUSTAT=12 and MUSTAT=14 to contribute 1.9 background tracks. Punchthrough to the third level combines with noise in the fourth level to contribute ≃ 3.6 tracks to the background (PUNCHTHROUGH 3). Finally we see that ≃ 17 of these 29 background tracks are actually due purely to punchthrough to the fourth level (PUNCHTHROUGH 4).

Pions from $K_S^0 \rightarrow \pi^+\pi^-$:

Figure 4.8(a) shows the momentum spectrum of charged pions from reconstructed $K_S^0 \rightarrow \pi^+\pi^-$ decays. Figure 4.8(b) show the MUSTAT distribution for those pions which satisfied the muon fiducial criteria. Table 4.3 shows the calculated punchthrough probabilities, based on a maximum likelihood fit similar to the one described above. The results are quite similar to those obtained from the MUSTAT analysis for all tracks.

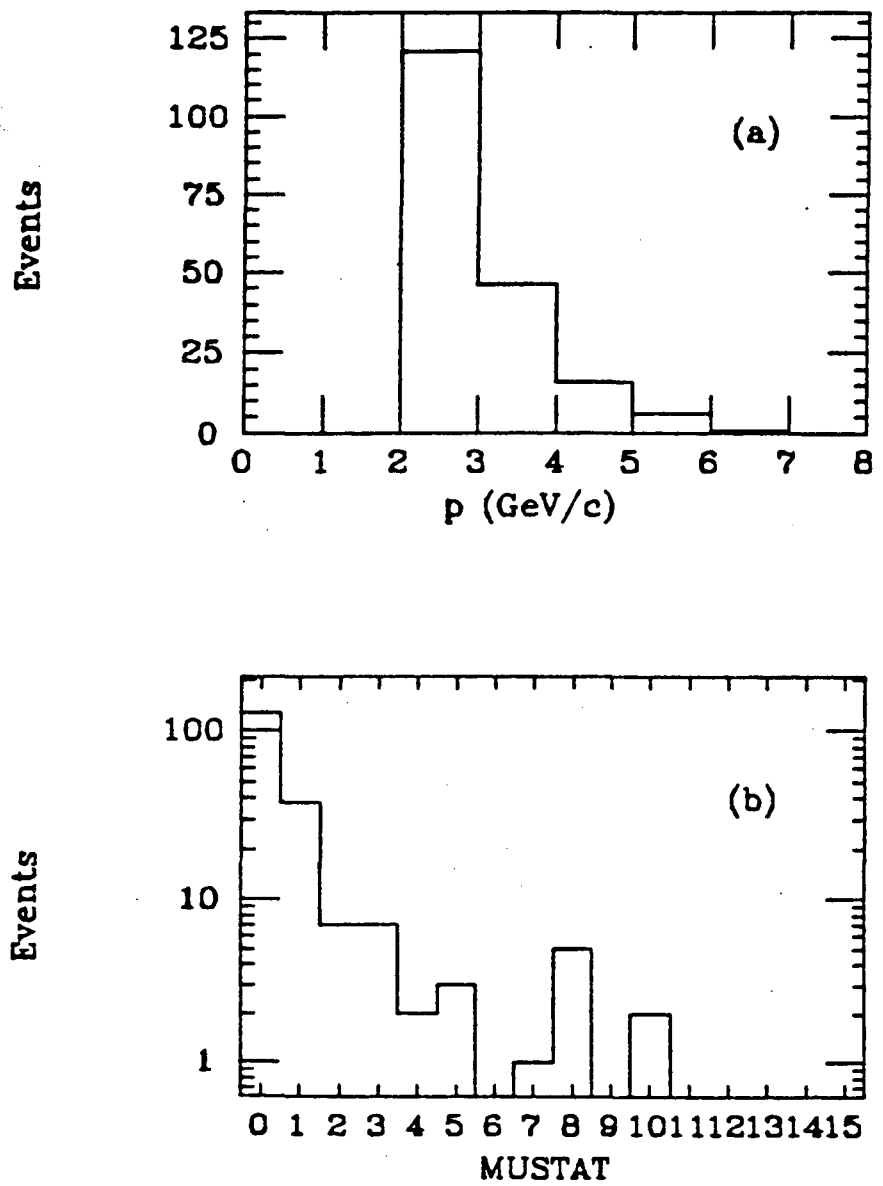

Figure 4.8: Pions from K_S^0 decay. (a) momentum (b) MUSTAT.

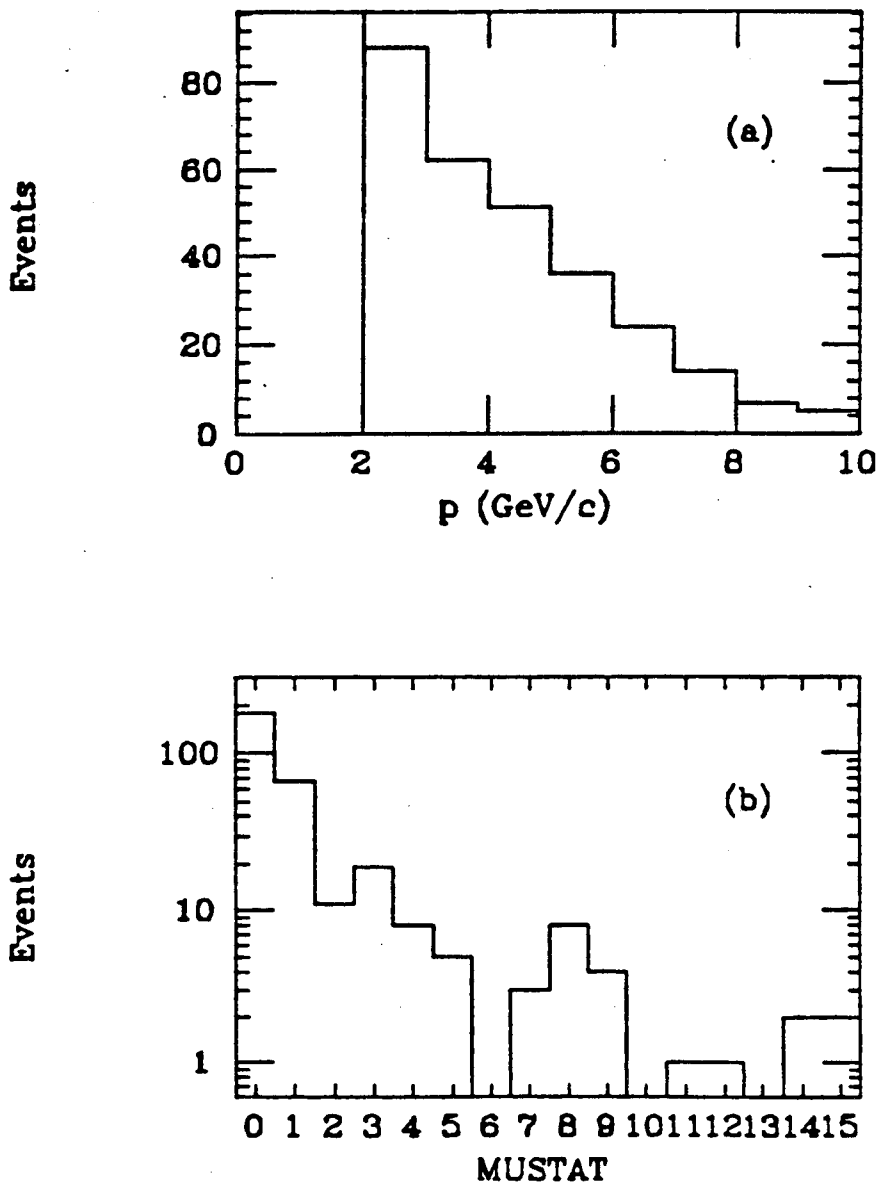

Figure 4.9: Pions from $\tau \rightarrow 3\pi\nu$ decay. (a) momentum (b) MUSTAT.

Pions from $\tau \rightarrow 3\pi\nu$:

Figure 4.9(a) shows the momentum spectrum of charged pions from reconstructed $\tau \rightarrow 3\pi\nu$ decays. Figure 4.9(b) show the MUSTAT distribution for those pions which satisfied the muon fiducial criteria. Table 4.3 shows the calculated punchthrough probabilities. The results give higher probabilities than those obtained from the fit to the MUSTAT distribution for all tracks. This probably arises from the harder momentum spectrum of this pion sample. In fact, the punchthrough probabilities are similar to those obtained by fitting the MUSTAT distribution for all tracks with $p > 6$ GeV/c.

Kaon punchthrough:

Although kaon cross sections are smaller that pion cross sections, the penetration probabilities for K's below a few GeV/c are smaller those for pions at the same momentum. This is due to the fact that the K's have less kinetic energy and thus range out sooner due to the heavier ionization loss. Kaons which do not range out are expected to have larger punchthrough probabilities because of the smaller interaction cross sections. The results on pions and kaons from D^0's described below indicates that this is indeed true. Our fit to the MUSTAT distribution of all tracks handles the mixture of pions, kaons and protons in a statistical sense, resulting in an weighted punchthrough probability for the mixture.

Pions and Kaons from $D^0 \rightarrow K\pi$:

A sample of identified D^0 candidates were obtained by utilizing the kinematic constraints in the decay $D^{*+} \rightarrow D^0\pi^+$ (+ c.c.). We then use the identified $D^0 \rightarrow K^-\pi^+$ to obtain a sample of identified charged pions and

kaons. The punchthrough results are shown in Table 4.3. The statistics are poor, but there is some indication that the kaon punchthrough probability is larger than that for pions.

source	momentum	PUNCHTHROUGH PROBABILITIES level 1 prob (%)	level 2 prob (%)	level 3 prob (%)
all tracks	$p > 2$	12.8±0.4	3.3±0.2	0.9±0.1
all tracks	$2 < p < 3$	10.5±0.6	2.4±0.3	0.8±0.2
all tracks	$3 < p < 4$	12.3±0.9	3.0±0.4	0.7±0.2
all tracks	$4 < p < 6$	17.4±1.1	4.6±0.6	1.0±0.3
all tracks	$p > 6$	17.0±1.5	5.4±0.8	2.0±0.5
$K_s^0 \rightarrow \pi^+\pi^-$	$2 < p < 6$	9.9±2.9	3.4±1.6	<1.1
$\tau \rightarrow 3\pi\nu$	$2 < p < 10$	21.5±2.9	6.6±1.6	0.8±0.7
π from D^0	$3 < p < 6$	6.8±5.0	5.4±3.3	<7.0
K from D^0	$3 < p < 6$	23.1±7.0	5.0±3.7	6.0±3.5

Table 4.3: Measured punchthrough probabilities from various sources.

Momentum dependence:

The fact that the pion-nucleon cross section is relatively constant over the momentum range of interest and the fact that the muon identification algorithm is able to detect hadronic interactions early in their development implies that the punchthrough probability should not be too sensitive to the incident energy. In order to investigate this assumption, the MUSTAT distributions can be analyzed for various bins of incident track momenta. Figure 4.10 shows the results and the resulting extrapolation to the fourth level of the muon system. The measured punchthrough values for levels 1-3 are tabulated in Table 4.3.

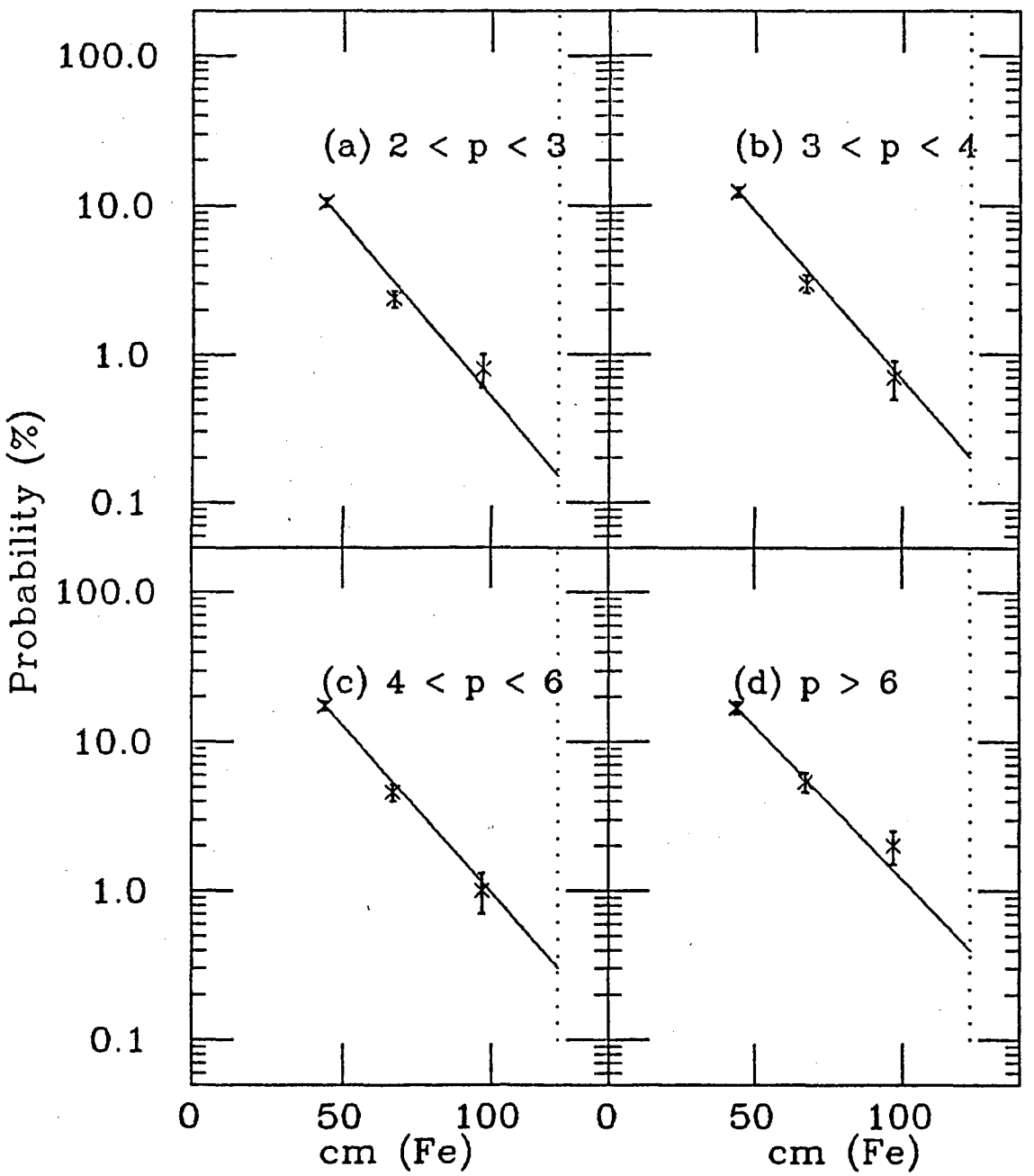

Figure 4.10: Hadron punchthrough probabilities in several momentum bins (a) 2 < p < 3; (b) 3 < p < 4; (c) 4 < p < 6; and (d) p > 6 (momenta in units of GeV/c). The data points are punchthrough probabilities to the first 3 levels. The vertical dotted line shows the thickness at level 4.

There is a distinct momentum dependence, however, it is not as large as that shown in Figure 4.6 for the 20 GeV spectrometer, where no rejection of secondaries was possible.

Transverse momentum dependence:

One might naively expect that the misidentification probabilities from punchthrough would not depend on transverse momentum. This would be true if it were not for the fact that the track overlap probability is dependent on transverse momentum. The probability of picking up a MUSTAT=1 or MUSTAT=14 contribution from overlap is larger at low $p_\perp$, and this reflects in the overall probability of obtaining MUSTAT=15 when combined with punchthrough.

Based on all the previous results, we can estimate the punchthrough probability as a function of p and $p_\perp$. The calculation is shown in Table 4.4. We divide the data into high ($p_\perp > 1$) and low ($p_\perp < 1$) transverse momentum regions for this analysis. We use the punchthrough probabilities shown in Table 4.3 to predict punchthrough probabilities to all levels as a function of momentum. The leftmost numbers in rows (b)-(e) of each $p,p_\perp$ bin of Figure 4.4 are, from top to bottom, the punchthrough probabilities to levels 1-4 respectively. For example, for $2 < p < 3$, we estimate probabilities of 11.0%, 3.0%, 0.6%, and 0.13%. In calculating these punchthrough probabilities, we include the effect of the $\simeq$ 3% proportional tube inefficiency at each level. In order to calculate the total misidentification probabilities we need to multiply these punchthrough probabilities by the probabilities that they will combine with "random" MUSTAT hits to form MUSTAT=15. Explicitly the contributions are:

P\PT	<1.0			>1.0			
2.00	1.0	*	.0003 = .0003	1.0	*	.0001 = .0001	(a)
	.1100	*	.0050 = .0005	.1100	*	.0025 = .0003	(b)
	.0300	*	.0100 = .0003	.0300	*	.0075 = .0002	(c)
	.0060	*	.0600 = .0004	.0060	*	.0600 = .0004	(d)
	.0013	*	1.000 = .0013	.0013	*	1.000 = .0013	(e)
			.0028			.0023	SUM
3.00	1.0	*	.0002 = .0002	1.0	*	.0001 = .0001	(a)
	.1300	*	.0033 = .0004	.1300	*	.0016 = .0002	(b)
	.0350	*	.0066 = .0002	.0350	*	.0049 = .0002	(c)
	.0080	*	.0400 = .0003	.0080	*	.0400 = .0003	(d)
	.0018	*	1.000 = .0018	.0018	*	1.000 = .0018	(e)
			.0029			.0026	SUM
4.00	1.0	*	.0002 = .0002	1.0	*	.0000 = .0000	(a)
	.1500	*	.0025 = .0004	.1500	*	.0012 = .0002	(b)
	.0400	*	.0050 = .0002	.0400	*	.0038 = .0002	(c)
	.0100	*	.0300 = .0003	.0100	*	.0300 = .0003	(d)
	.0022	*	1.000 = .0022	.0022	*	1.000 = .0022	(e)
			.0033			.0029	SUM
5.00	1.0	*	.0002 = .0002	1.0	*	.0000 = .0000	(a)
	.1700	*	.0020 = .0003	.1700	*	.0010 = .0002	(b)
	.0500	*	.0040 = .0002	.0500	*	.0030 = .0002	(c)
	.0120	*	.0240 = .0003	.0120	*	.0240 = .0003	(d)
	.0027	*	1.000 = .0027	.0027	*	1.000 = .0027	(e)
			.0037			.0034	SUM
6.00	1.0	*	.0001 = .0001	1.0	*	.0000 = .0000	(a)
	.2000	*	.0016 = .0003	.2000	*	.0008 = .0002	(b)
	.0600	*	.0033 = .0002	.0600	*	.0025 = .0002	(c)
	.0140	*	.0200 = .0003	.0140	*	.0200 = .0003	(d)
	.0036	*	1.000 = .0036	.0036	*	1.000 = .0036	(e)
			.0045			.0043	SUM

Table 4.4: Calculation of hadron punchthrough probabilities

(a) 1. × M(15)
(b) P_1 × M(14)
(c) P_2 × [M(12) + M(14)]
(d) P_3 × M(≥ 8)
(e) P_4 × M(≥ 0)

where P_i is the punchthrough probability to level i, and M(j) is the probability of having a random MUSTAT=j. The values of P_i are estimated from Table 4.3. The values of M(j) are calculated from Figure 4.5 assuming that the overlap probability (e.g. M(1), M(14)) is twice as large at low $p_\perp$ as high $p_\perp$ and that noise hits (e.g. M(8),M(12)) are independent of $p_\perp$. The assumption about the $p_\perp$ dependence of the overlap is based on studies of the $p,p_\perp$ distributions of MUSTAT=1 and 14 in the flipped track analysis.

Table 4.5 shows the population of charged tracks the passed the muon fiducial criteria. We combine Tables 4.6 and 4.5 to obtain the expected background population from punchthrough as a function of p and $p_\perp$. This result is shown in Table 4.7.

Hadron decay in flight:

Charged pions and kaons can decay in flight to produce final state muons which penetrate the absorber and give signals in the proportional tubes. The branching ratio for π^+ to $\mu^+\nu$ is nearly 100%, while the branching ratio for K^+ to $\mu^+\nu$ is ≃ 64%. The fraction of charged pions or kaons which actually decay into muons before reaching the muon system is, of course, much smaller than the branching ratio. The probability that a particle with mass m, momentum p, and proper lifetime τ_0 decays before it has traveled a distance ℓ is:

$$P(<\ell) = 1 - \exp[-m\ell/pc\tau_0] \qquad (4.4)$$

P\PT	0.00	0.50	1.00	1.50
2.0	2568.0	1655.0	432.0	257.0
3.0	1185.0	851.0	247.0	200.0
4.0	587.0	453.0	153.0	122.0
5.0	316.0	240.0	97.0	74.0
6.0	415.0	358.0	136.0	165.0

Table 4.5: Hadrons in muon fiducial volume

P\PT	0.00	0.50	1.00	1.50
2.0	0.0028	0.0028	0.0023	0.0023
3.0	0.0029	0.0029	0.0026	0.0026
4.0	0.0033	0.0033	0.0029	0.0029
5.0	0.0037	0.0037	0.0034	0.0034
6.0	0.0045	0.0045	0.0043	0.0043

Table 4.6: Hadron punchthrough probabilities

P\PT	0.00	0.50	1.00	1.50
2.0	7.2	4.6	1.0	0.6
3.0	3.4	2.5	0.6	0.5
4.0	1.9	1.5	0.4	0.4
5.0	1.1	0.9	0.3	0.3
6.0	1.8	1.6	0.6	0.7

Table 4.7: Background to muon signal from hadron punchthrough

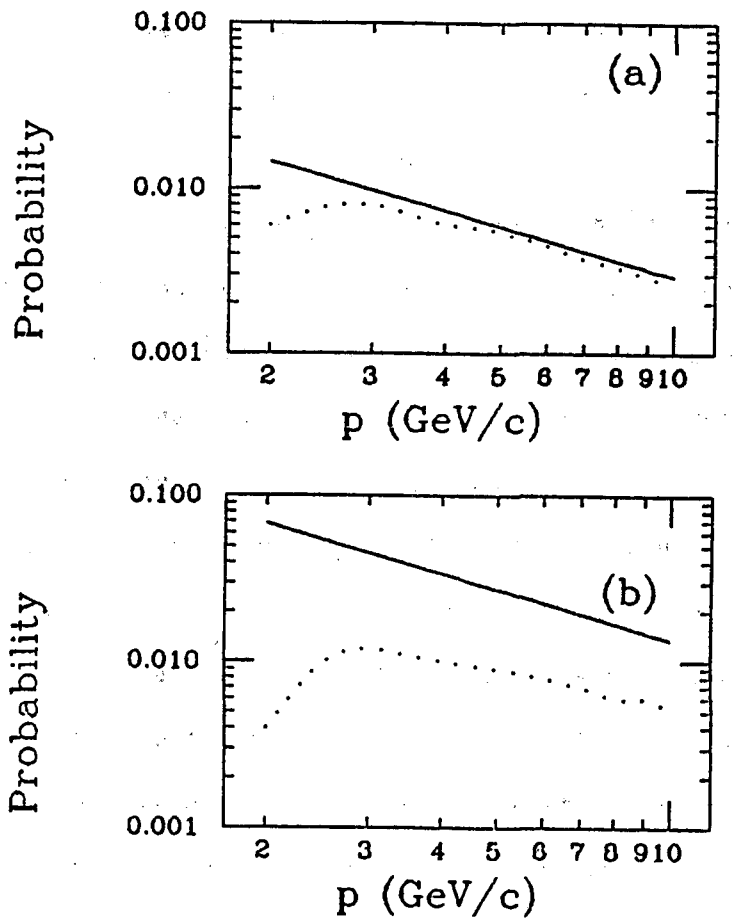

Figure 4.11: Pion and Kaon μ_2 decay probabilities
(a) pion decays and (b) kaon decays. The solid lines show the μ_2 decay probabilities. The dotted lines show the misidentification probabilities. The momentum is that of parent pion or kaon.

The values of $c\tau_0$ are 7.8m and 3.7m for pions and kaons, respectively. If we use a flight path ℓ of 1.6m, which is the average distance to the calorimeters, and include the branching fraction for kaons, we find:

$$\pi \rightarrow \mu\nu: \quad P(<1.6m) \simeq .029/p(GeV/c)$$
$$K \rightarrow \mu\nu: \quad P(<1.6m) \simeq .136/p(GeV/c)$$

The solid and dashed lines in Figure 4.11 show the decay probabilities based on this simple calculation.

Actually, only a fraction of these decays are identified as muon candidates by the muon identification criteria. This is due to the decay kinematics which can produce muons that are too low in momentum to penetrate the absorber or which can result in large decay angles causing the muon trajectory to lie more than 2σ away from the extrapolation. Both of these effects are more pronounced for K decays relative to π decays because of the larger Q^2 in the process.

Figure 4.12 shows a plot of the decay muon momentum versus parent hadron momentum for pions and kaons with $p > 2$ GeV/c. Those decays in which the muon momentum is less that $\simeq$ 1.8 GeV/c fail the muon identification criteria since they cannot penetrate all layers of the steel absorbers. Figure 4.13 shows the product of the decay angle and the parent hadron momentum for pions and kaons. For comparison, a solid line is shown at the value which represents a 2σ rms multiple scattering ($\simeq$ 17 rad GeV/c) from the $16X_0$ thick calorimeter modules (a major component to the extrapolation error). Many of the kaon decays result in a decay angle which is large in comparison to the typical multiple scattering angle. Therefore proportional tube hits from muons in these decays may often lie outside of the 2σ search region.

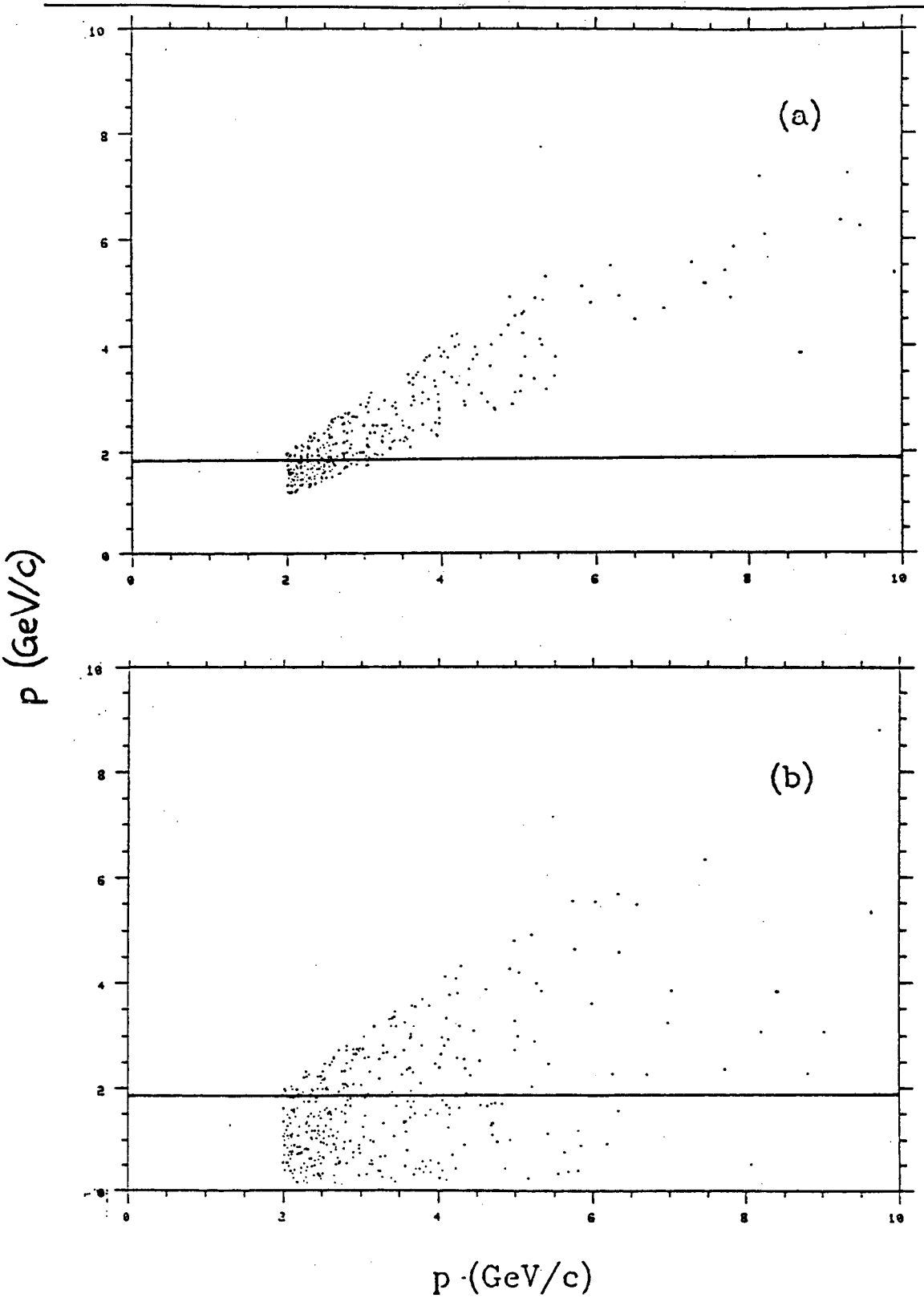

Figure 4.12: p_μ vs. p_{had} in π and K μ_2 decays
(a)pion decays; (b) kaon decays. The solid line shows the momentum necessary for penetration to the fourth muon detector level. Note that many of the decays result in daughter muons which are unable to penetrate that far.

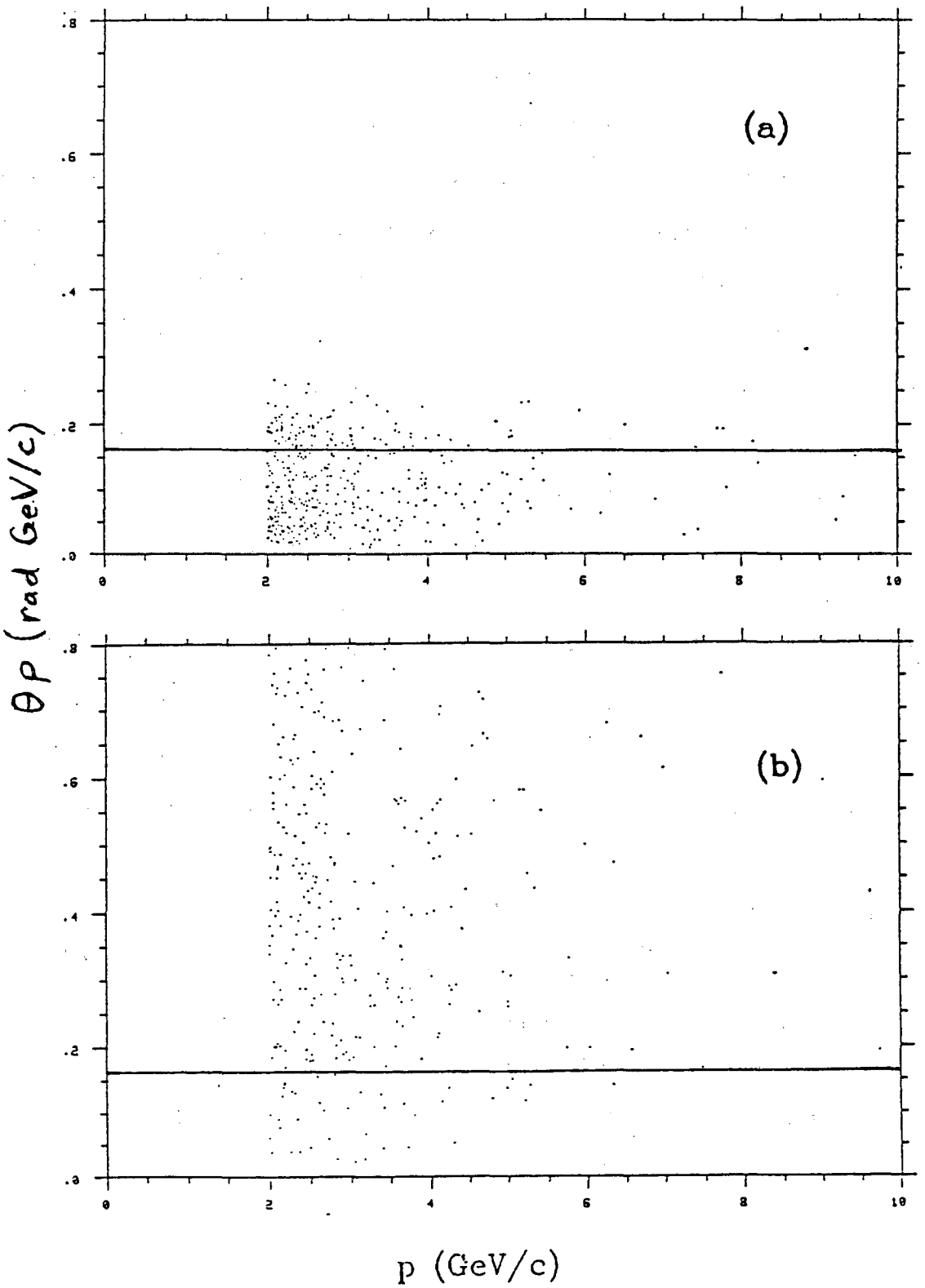

Figure 4.13: Decay angle times p_{had} for π and K μ_2 decays (a)pion decays; (b) kaon decays. The solid line illustrates a typical 2σ multiple scattering angle from the detector components. Note that most of the kaons decays result in larger decay angles.

A further complication arises from the two kinematic effects discussed above. When the decay point lies within the drift chamber volume, there will be two track segments with different momenta and with different slopes at the decay point. The charged track reconstruction algorithm does not attempt to distinguish the two segments, but rather tries to fit a single smooth track through the two kinked segments. If the decay occurs very early in the chamber, the fit momentum will tend to reflect the muon momentum. If the decay occurs very late, then the fit will more nearly reflect the parent hadron momentum. If the decay occurs at an intermediate point, then the detected momentum will have a more complicated relation to the produced momenta and will depend on the magnitude and orientation of the decay angle. In severe cases, the track finding algorithm may fail to find any acceptable trajectory through the two segments.

In order to properly handle all of these effects, we use a Monte Carlo simulation to calculate the expected misidentification contributions from π and K decay. Since a "decay" track (parent-daughter combination) with a given measured momentum can arise from a broad spectrum of produced parent momenta, it is necessary to reproduce the entire hadron spectra in order to calculate the number of expected decays at any given detected momentum. Figure 4.14(a) shows the observed charged particle spectrum in the data. Figure 4.14(b) shows the corresponding spectrum from the Monte Carlo. The fractions of π's, K's, and p's produced in the Monte Carlo are consistent with previous measurements [41]. Using this spectrum, we define a misidentification probability $P_{h\text{-}\mu}$ as:

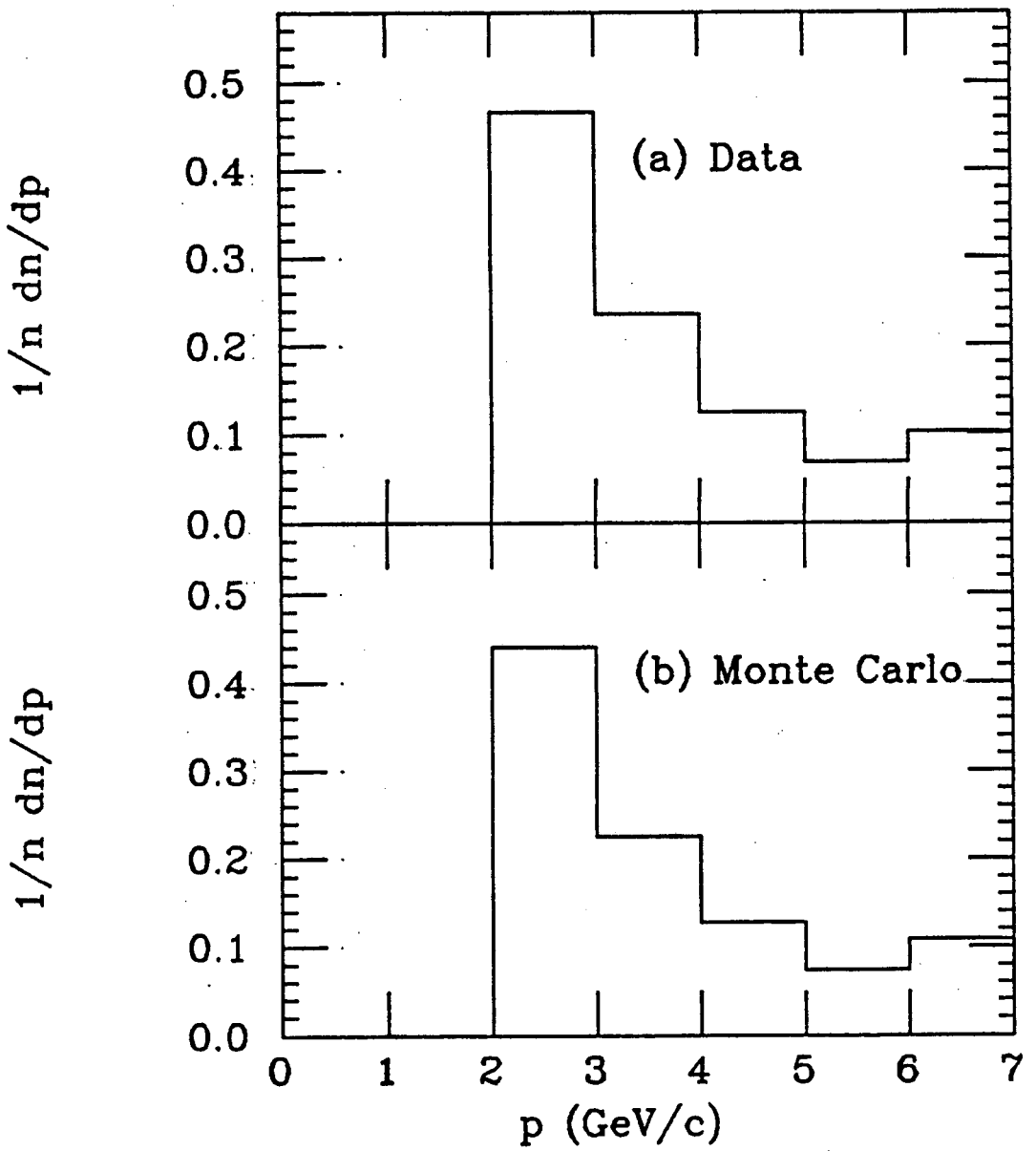

Figure 4.14: Charged particle spectra for (a) data and (b) Monte Carlo

$$P_{h\text{-}\mu}(p) = \frac{\#\ \mu s \text{ from h decays detected with momentum p}}{\#\ \text{charged hadrons h detected with momentum p}}$$

The hadrons h, that appear in the denominator, are required to pass the same fiducial criteria as the muon candidates. Figure 4.11 shows these misidentification probabilities as dotted lines. These probabilities are smaller than the decay probabilities (shown as solid lines) due to the decay kinematics discussed earlier.

We use the Monte Carlo prediction, normalized to the total number of observed charged tracks passing the muon fiducial criteria, to predict the $p,p_\perp$ population of muon candidates arising from decays in flight. The result is shown in Table 4.8.

P\PT	0.00	0.50	1.00	1.50
2.0	10.0	6.0	3.0	2.0
3.0	6.0	4.5	2.5	1.0
4.0	2.5	1.5	1.5	1.0
5.0	1.5	1.5	0.5	0.5
6.0	1.5	1.0	0.5	0.5

Table 4.8: Background to muon signal from decays in flight.

5. ANALYSIS PROCEDURE

5.1 Hadronic Event Selection

The total data sample corresponds to an integrated luminosity of approximately (32 ± 2) pb^{-1} taken at a c.m. energy of 29 GeV. The following criteria were used to select a sample of hadronic event candidates:

1) A reconstructed event vertex with a radial distance from the interaction point (projected in the xy-plane) < 0.04 m and a longitudinal distance (projected along the beamline) < 0.07 m.

2) At least five charged tracks satisfying the following criteria:

   2a) Radial distance of closest approach to interaction point < 0.04 m and a longitudinal distance < 0.08 m.
   2b) P_{xy} > 0.100 Gev/c and P_{tot} < 16.0 GeV/c
   2c) Not a member of an identified photon conversion or Dalitz decay pair.

3) A total visible energy $E_{vis} > 0.25\ E_{cm}$, where E_{cm} is the center of mass energy. The contribution from charged particles was calculated by summing the momenta of all tracks that satisfied requirements 2a) and 2b) above. Neutral energy was calculated by summing the energies from reconstructed photon candidates which satisfied:

   3a) The photon was reconstructed in a LA barrel module.
   3b) Reconstructed energy > 200 MeV.
   3c) < 50% of its energy shared with other reconstructed showers.
   3d) Distance of shower centroid from nearest charged track projection > 0.07 m.

4) $|\cos\theta_{thrust}| < 0.7$, where θ_{thrust} is the angle between the beamline and the reconstructed thrust axis. The event thrust axes is calculated using all charged tracks which satisfied 2a) and 2b) above. An extra "ghost" track is added by the algorithm to balance momentum.

A total of 10691 events passed these cuts.

5.2 Event backgrounds

Processes other than the single photon annihilation of e^+e^- into hadrons can produce event topologies which meet the above selection criteria. Altogether they constitute ≈ 2% of the events in the sample.

Each of the important background processes and its possible contribution to the lepton signal will be discussed below.

$e^+e^- \rightarrow \tau^+\tau^-$:

It is important to consider the background from τ pair production because the leptonic decay mode $\tau \rightarrow \ell\nu\nu$ can potentially contribute to the prompt lepton signal. Furthermore, since each τ is produced with the full beam energy of 14.5 GeV, the resulting decay lepton has a relatively large average momentum. If leptons from this background source did contribute to our sample, they could significantly increase the observed number of high momentum prompt leptons in our sample.

When a τ decays leptonically, it produces only one charged track in the final state. Thus in a τ pair event where one τ decays leptonically, the other decay must result in four or more observed charged tracks in order for the event to pass the multiplicity cut of five. The branching ratio for τ into five charged particles has been measured to be less than 0.5% [42]. From this limit we expect less than 4 events of this "1+5" topology in our sample. In a visual scan of all events containing a lepton with $p > 4$ GeV/c, no "1+5" event candidates were found. The only other topology that can contribute to the lepton signal occurs when the second τ decay contains one or more photon conversions or π^0 Dalitz decays. Note that our hadron selection criterion of five observed charged tracks excludes members of identified pairs (criterion 2c). This eliminates most of the τ pair background arising from events containing photon conversions or Dalitz decays. There is a small residual contribution from events where the conversion pair is not identified. In a visual scan of all events with lepton

candidates with p > 4 GeV/c, one event satisfied the "1+3+conversion" topology and was removed.

There is a τ pair topology which does contribute to the hadronic event sample, but which does not contribute to the prompt lepton signal. This topology occurs when both τ's in the event decay into three charged tracks. This "3+3" topology is expected to contribute on the order of 35±10 events to the hadronic sample.

$e^+e^- \rightarrow e^+e^-$ + hadrons:

The order α^4 diagrams which contribute to the total cross section for $e^+e^- \rightarrow e^+e^-$ + hadrons are shown in Figure 5.1(a)-(b). There is also an s-channel diagram, similar to Figure 5.1(b), which does not contribute significantly to the cross section. In the following discussion, events arising from the diagram in Figure 5.1(a) will be referred to as "two-photon" and those arising from Figure 5.1(b) as "inelastic Compton scatters". The dominant contribution to the total cross section comes from the two-photon diagram. The distribution of total produced hadron energy W from this process is peaked near zero and falls rapidly. Most events from this distribution fail the visible energy requirement ($E_{vis} > 0.25\ E_{cm}$) in our hadron selection criteria. We are able to estimate the total number of events remaining in our sample by using the data from the small angle tagging (SAT) system. This system detects electrons which are scattered between 21 and 82 mrad from the beamline. The probability that a two-photon event will result in an electron being observed in this region is 20±5%. In the hadronic sample of 10691 events, 32 such events were observed. This implies a background of about 160 ± 49 events.

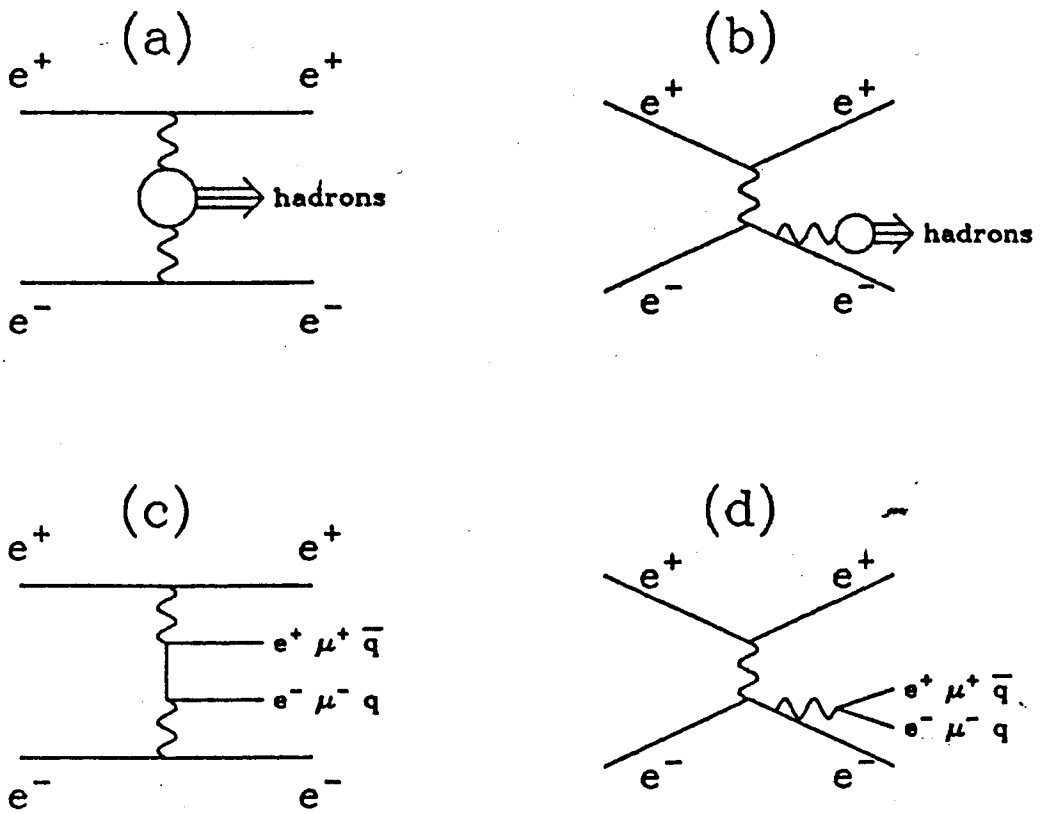

Figure 5.1: Order α^4 contributions to $e^+e^- \rightarrow e^+e^-$ + hadrons

There are particular event topologies resulting from the α^4 processes which can contribute substantially to the high momentum prompt electron signal. Fortunately these events are relatively easy to distinguish from the single photon hadronic events and the contamination can be removed. These events occur when one of the photons in Figure 5.1(a) or (b) has a momentum transfer Q large enough to deflect one of the electrons into the main detector. Usually the hadrons are also visible in the detector since they balance the transverse momentum (w.r.t. the beamline) of the electron. The electron itself usually has an energy greater than .25 E_{cm}. Thus if the hadronization results in four or more visible charged tracks, the event will satisfy our selection criteria.

In order to remove these background events a visual scan was made of all events containing an electron with momentum greater that 6 GeV/c. There were a total of 39 such events. Four of these events were classified as inelastic Compton scatters (see Figure 5.2) and three of them had two opposite sign electron candidates per event. Thus a total of 7 electron candidates were removed in this category. A total of 10 events were classified as two-photon (see Fig. 5.3) and each event contained a single electron candidate. Thus a total of 17 high momentum prompt electron candidates were removed. Figure 5.4 shows the momentum spectra for the 25 remaining signal candidates and for the 17 background candidates. Note that the momentum spectrum of the remaining signal is falling with increasing p while the background spectrum is rather flat with some peaking in the 8 - 10 GeV/c region.

In order to check that the number of events removed was reasonable, a comparison was made with a version of the Smith-Vermaseren [43] Monte Carlo. This Monte Carlo integrates the cross-section for $e^+e^- \rightarrow e^+e^-\mu^+\mu^-$ over a defined geometric and kinematic acceptance using the diagrams in Figure 5.1(c) and (d). The corresponding cross section for e^+e^- + hadrons, can be estimated in the context of the quark-parton model by replacing the muons with quarks. The ratio of hadrons to μ pairs for the two-photon diagram in the hard scattering approximation is about 34/27. This estimation comes from the q_f^4 coupling for u,d,s,and c quarks and a factor of 3 for color. A similar calculation for the ratio of hadrons to μ pairs from inelastic Compton scattering results in a ratio of 10/3. Here the cross section is proportional to q_f^2 and the color factor is the same. The Monte Carlo predicts a cross section of $\simeq$ 4×10^{-4} nb, or 13 events in 32 pb^{-1}, for $e^+e^-\mu^+\mu^-$, where at least one electron is within the electron fiducial volume and both muons are visible in the detector. The two-photon and inelastic Compton processes each contribute about equally. This translates into about 29 expected hadronic events in the hard scattering approximation. We expect the number actually observed to be somewhat lower than this because the hadron selection criteria require at least four visible charged tracks from the hadronic system in addition to the electron candidate. The mass of the hadronic system, especially in the inelastic Compton process, is such that it often produces a lower multiplicity final state. The prediction of 29 produced hadronic events is thus consistent with the observation of 14 events which pass our selection criteria.

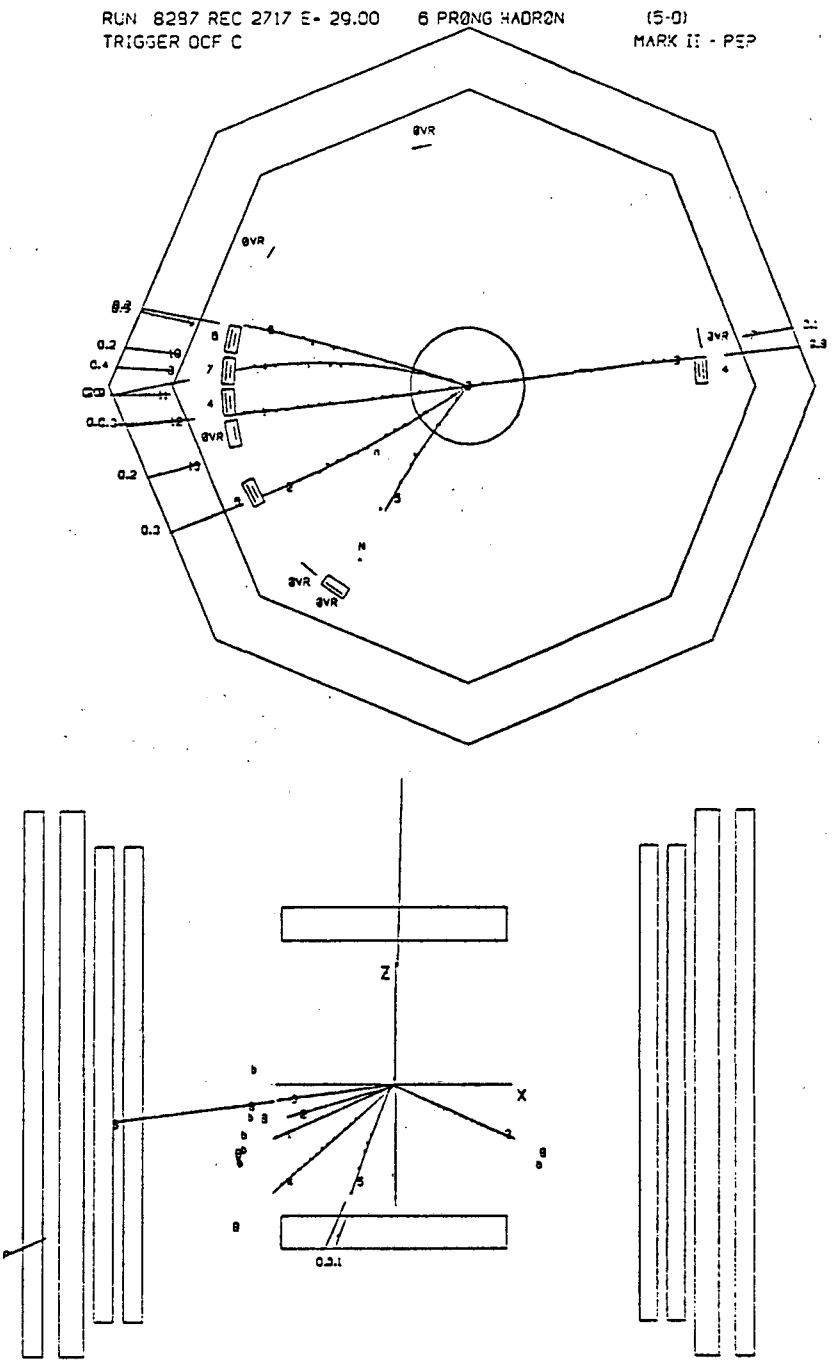

Figure 5.2: Large Q^2 two-photon background event.

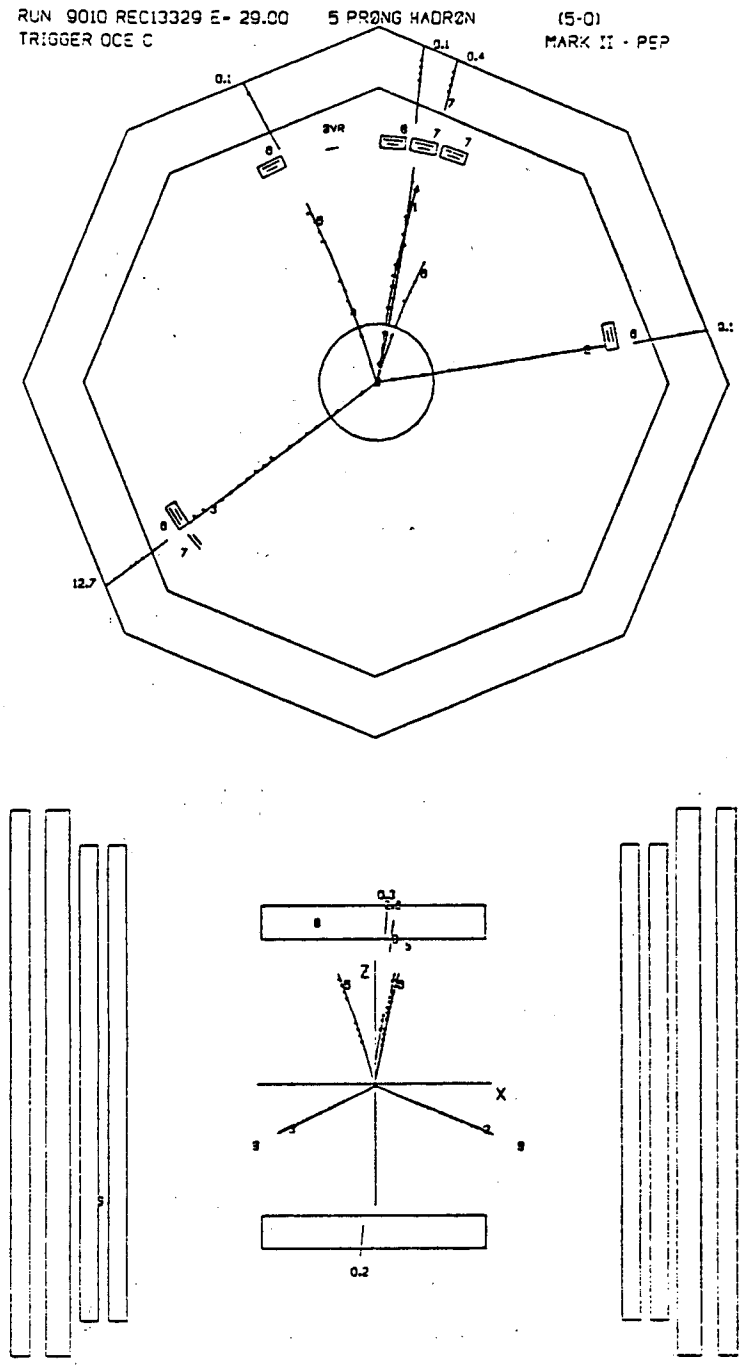

Figure 5.3: Inelastic Compton scatter background event.

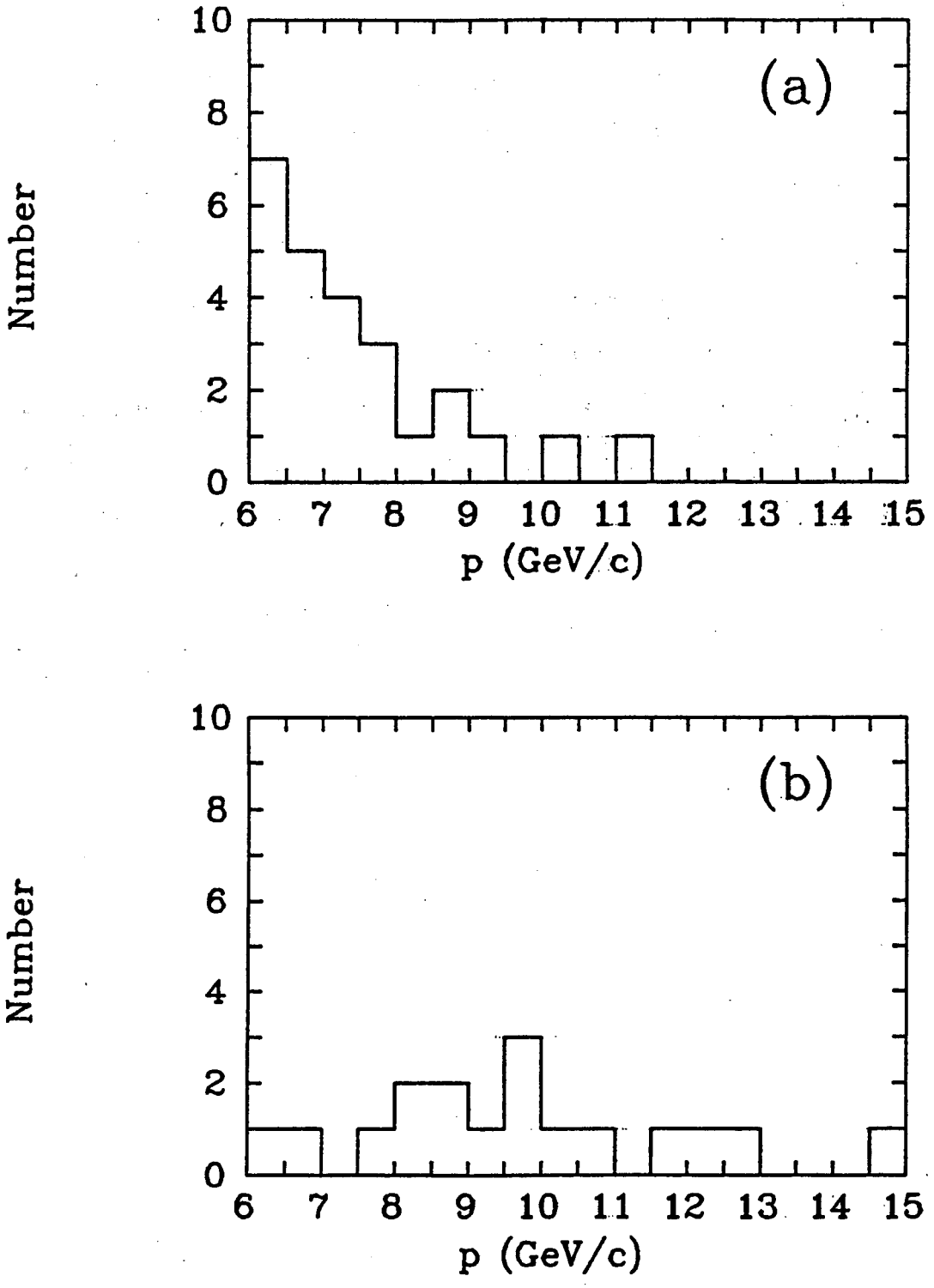

Figure 5.4: Comparison of of (a) prompt and (b) background momenta Only the high momentum part of the spectrum (p > 6 GeV/c) is shown.

Beam-gas events:

The beam-gas contamination can be estimated from the longitudinal event vertex distribution. From this distribution we estimate that less than 20 of the 10691 hadronic candidates arises from beam-gas interactions. This low rate is primarily due to the multiplicity and total visible energy cuts in our hadron selection. A background beam-gas event in which both the beam electron and the nuclear fragments were scattered into the detector would qualitatively look very much like the two-photon process described above. The event would have a large longitudinal momentum imbalance and the electron would tend to be scattered in the direction of the same-sign beam. Such an event would have been removed in the visual scan for two-photon events that was described above.

5.3 Electron results

The net prompt electron signal is obtained from the raw signal by subtracting the backgrounds from misidentified hadrons and from non-prompt electrons. This subtraction and the associated statistical and systematic errors are discussed below.

Raw signal:

The raw electron signal in the hadronic event sample consists of all electron candidates (as defined in Chapter 3) that are not associated with a photon conversion or Dalitz pair. Events that were determined to be two-photon or inelastic Compton scatters have been excluded from this sample. Table 5.1 shows the momentum and transverse momentum distribution for the raw electron signal. The backgrounds from misidentified hadrons and from non-prompt electrons will be subtracted bin-by-bin from this distribution.

Misidentified hadron subtraction:

The background from misidentified hadrons was calculated in Section 3.4 and summarized in Table 3.7. That table is reproduced in Table 5.2 below.

Pair subtraction:

In addition to the background from misidentified hadrons, there is a smaller background from non-prompt electrons. The dominant contribution comes from residual γ conversions and Dalitz decays that were not removed (see section 3.5). The expected background contribution from this source was shown in Table 3.10 and is reproduced in Table 5.3 below.

P\PT	0.00	0.50	1.00	1.50
1.0	363	112	28	3
2.0	115	54	21	13
3.0	46	31	12	9
4.0	29	23	10	6
5.0	7	11	5	8
6.0	9	9	4	3

Table 5.1: Raw prompt electron signal.
Electrons from identified photon conversions and Dalitz decays are not included.

P\PT	0.00	0.50	1.00	1.50
1.0	246. ± 88.	57. ± 28	10. ± 4.4	1.2 ± 0.5
2.0	63. ± 33.	21. ± 13.	4.9 ± 2.1	3.1 ± 1.3
3.0	19. ± 10.	8.0 ± 4.0	1.8 ± 0.7	1.3 ± 0.5
4.0	6.5 ± 2.8	3.5 ± 2.1	0.9 ± 0.5	0.7 ± 0.4
5.0	3.4 ± 1.5	1.9 ± 1.1	0.6 ± 0.3	0.4 ± 0.2
6.0	4.0 ± 2.0	2.3 ± 1.7	0.6 ± 0.4	0.7 ± 0.5

Table 5.2: Expected electron background from misidentified hadrons.
The errors shown reflect the systematic uncertainties in the misidentification probabilities.

P\PT	0.00	0.50	1.00	1.50
1.0	66.0	12.0	3.0	1.0
2.0	16.0	6.0	1.0	0.5
3.0	7.0	2.0	1.0	0.5
4.0	1.0	1.0	0.5	0.25
5.0	0.5	0.5	0.25	0.25
6.0	0.5	0.5	0.25	0.25

Table 5.3: Expected background from non-prompt electrons.

Net signal:

Table 5.4 shows the net prompt electron signal and the corresponding statistical and systematic errors in each bin. the systematic error is dominated by the uncertainties in the hadron misidentification probabilities. These uncertainties were given in Table 3.5 and are typically ± 50%. There is a much smaller contribution to the systematic error from uncertainties in the number of residual electrons from gamma conversions, Dalitz decays and non-hadronic event sources. This uncertainty is estimated to be ± 20%.

P\PT	0.0	0.50	1.00	1.50	
1.0	50.6	42.8	14.6	0.8	Signal
	26.0	13.5	6.4	2.3	Stat. Err.
	102.6	31.0	5.8	0.8	Syst. Err.
2.0	36.5	26.8	15.7	9.8	Signal
	13.9	9.0	5.1	4.0	Stat. Err.
	34.4	11.8	2.3	1.4	Syst. Err.
3.0	19.7	21.0	9.2	7.1	Signal
	8.5	6.4	3.9	3.3	Stat. Err.
	11.1	4.4	1.1	0.8	Syst. Err.
4.0	21.5	17.5	8.6	5.0	Signal
	6.0	5.1	3.4	2.6	Stat. Err.
	3.5	1.9	0.6	0.4	Syst. Err.
5.0	3.1	8.6	4.2	7.4	Signal
	3.3	3.7	2.4	2.9	Stat. Err.
	1.8	1.0	0.3	0.2	Syst. Err.
6.0	4.5	6.2	3.1	2.1	Signal
	3.7	3.4	2.2	2.0	Stat. Err.
	2.1	1.2	0.4	0.4	Syst. Err.

Table 5.4: Net prompt electron signal.

5.4 Muon results

The net prompt muon signal is obtained from the raw signal by subtracting the backgrounds from punchthrough hadrons and from hadron decays in flight. This subtraction and the associated statistical and systematic errors are discussed below.

Raw signal:

The raw muon signal in the hadronic event sample consists of all muon candidates (as defined in Chapter 4). Table 5.5 shows the momentum and transverse momentum distribution for the raw electron signal. The backgrounds from hadron punchthrough and decays in flight will be subtracted bin-by-bin from this distribution.

Hadron punchthrough subtraction:

The background from hadron punchthrough was calculated in Section 4.4 and summarized in Table 4.7. That table is reproduced in Table 5.6 below.

π and K decay subtraction:

The background from charged π and K μ_2 decays was discussed in Section 4.4 and summarized in Table 4.8. That table is reproduced in Table 5.7 below.

P\PT	0.00	0.50	1.00	1.50
2.0	34.0	31.0	16.0	6.0
3.0	18.0	23.0	10.0	6.0
4.0	20.0	10.0	5.0	2.0
5.0	8.0	6.0	3.0	3.0
6.0	8.0	7.0	3.0	3.0

Table 5.5: Raw prompt muon signal.

P\PT	0.00	0.50	1.00	1.50
2.0	7.2	4.6	1.0	0.6
3.0	3.4	2.5	0.6	0.5
4.0	1.9	1.5	0.4	0.4
5.0	1.1	0.9	0.3	0.3
6.0	1.8	1.6	0.6	0.7

Table 5.6: Background to muon signal from hadron punchthrough

P\PT	0.00	0.50	1.00	1.50
2.0	9.1	6.7	3.2	2.2
3.0	5.1	3.4	1.5	1.0
4.0	2.5	1.9	0.8	0.7
5.0	1.7	1.3	0.7	0.7
6.0	1.9	1.8	0.8	1.0

Table 5.7: Expected background contribution from π and K μ_2 decays.

Net signal:

Table 5.8 shows the net prompt muon signal and the corresponding statistical and systematic errors in each bin. The systematic error arises from an estimated ± 50% uncertainty in the hadron punchthrough probabilities and a ± 25% uncertainty in the π and K decay contributions.

P\PT	0.0	0.50	1.00	1.50	
2.0	17.7	19.7	11.8	3.2	Signal
	7.1	6.5	4.5	3.0	Stat. Err.
	5.9	4.0	1.3	0.8	Syst. Err.
3.0	9.5	17.1	7.9	4.5	Signal
	5.2	5.4	3.5	2.7	Stat. Err.
	3.0	2.1	0.7	0.5	Syst. Err.
4.0	15.6	6.6	3.8	0.9	Signal
	4.9	3.7	2.5	1.7	Stat. Err.
	1.6	1.2	0.4	0.4	Syst. Err.
5.0	5.1	3.8	2.0	2.0	Signal
	3.3	2.9	2.0	2.0	Stat. Err.
	1.0	0.8	0.3	0.3	Syst. Err.
6.0	4.2	3.6	1.6	1.3	Signal
	3.4	3.2	2.1	2.2	Stat. Err.
	1.4	1.3	0.5	0.6	Syst. Err.

Table 5.8: Net prompt muon signal.

6. PROMPT LEPTON CROSS SECTIONS

In order to extract inclusive prompt lepton cross sections from the net lepton signals (Tables 5.4 and 5.8) we must correct the data for fiducial acceptance and detection efficiencies.

6.1 Fiducial acceptance

The fiducial acceptance for prompt leptons in detected hadronic events is defined as:

$$\epsilon_{acc}(p) = \frac{\text{\# leptons with momentum p satisfying the fiducial criteria}}{\text{\# leptons produced with momentum p}} \quad (6.1)$$

The denominator only includes those leptons produced in the detected events. Thus the acceptance efficiency as defined above does not include the efficiency for detecting hadronic events. If the prompt leptons were produced isotropically and there was no bias from our hadronic event selection criteria, then this acceptance would be equivalent to the simple geometrical acceptance of the fiducial volume. The acceptance as defined in Eq. (6.1) is actually somewhat larger than the geometrical acceptance. This is due to the fact that the hadronic events are jet-like and that the leptons are correlated with the jet direction. Since the detected hadronic event must be fairly well contained in the detector ($E_{vis} > .25\ E_{cm}$ and $|\cos\theta_{thrust}| < 0.7$) we enhance the probability of observing the lepton. We determine the acceptance from a Monte Carlo detector simulation using definition Eq. (6.1) (For a description of the Monte Carlo see Section 7.1.) There is a slight model dependence arising from uncertainties in the bottom and charm quark fragmentation functions. Fragmentation functions which yield larger average energies for bottom and charm hadrons result in

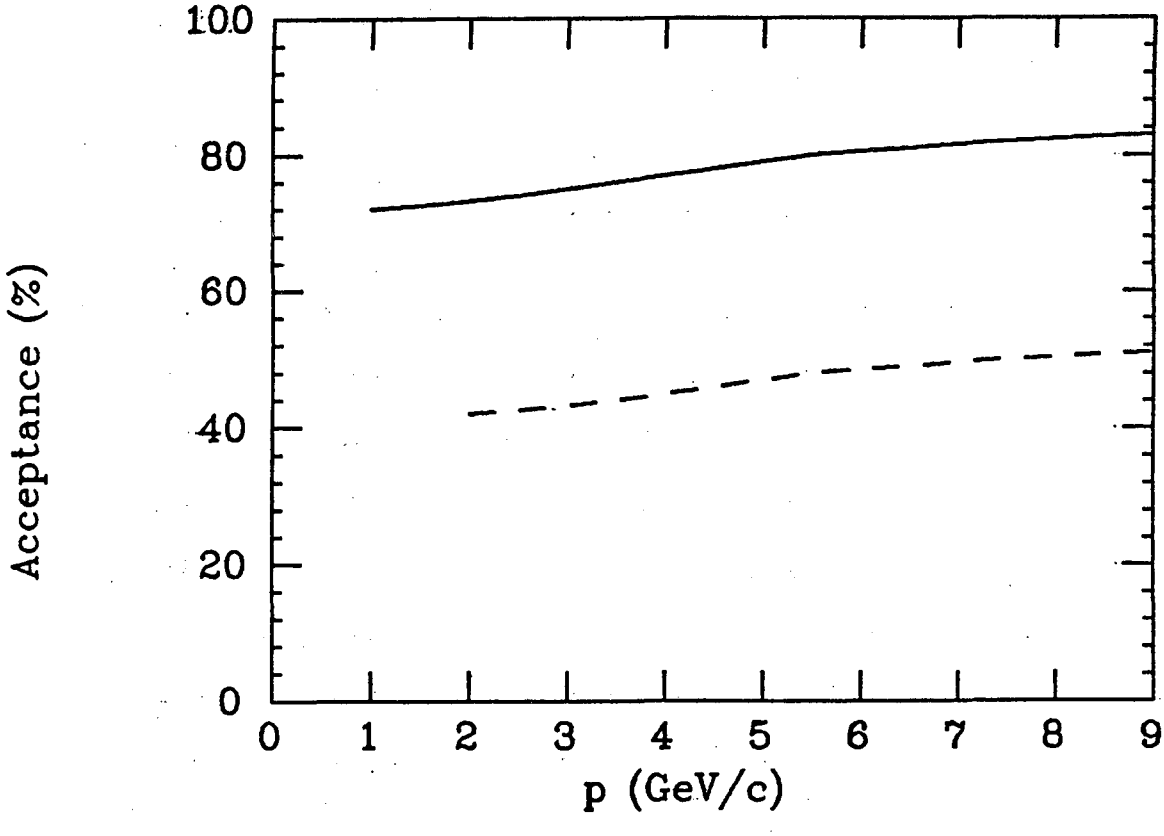

Figure 6.1: Fiducial acceptance for electrons and muons. Electrons (solid line); Muons (dashed line).

more collimated heavy quark jets and thus a larger prompt lepton acceptance. The acceptance also depends somewhat on the momentum of the detected lepton. This effect also arises from the effects of the event selection criteria. The fiducial acceptances for electrons and muons as determined from the Monte Carlo are shown in Figure 6.1. A systematic error of ±5% is assigned based on the model dependence of the determination.

6.2 Identification Efficiency

The identification efficiency for prompt leptons in a sample of detected hadronic events is defined as:

$$\epsilon_{id}(p,p_\perp) = \frac{\text{\# leptons with } (p,p_\perp) \text{ identified}}{\text{\# leptons with } (p,p_\perp) \text{ satisfying the fiducial criteria}} \quad (6.2)$$

These identification efficiencies were determined in Sections 3.3 and 4.3 for electrons and muons respectively. The $p,p_\perp$ dependence of these efficiencies were shown in Tables 3.2 and 4.1. These tables are reproduced in Tables 6.1 and 6.2 below.

6.3 Inclusive Cross Sections

The net prompt lepton signals (Tables 5.4 and 5.8) are corrected for the fiducial acceptance and identification efficiency to obtain the corrected signals shown in Tables 6.3 and 6.4. We can now extract inclusive rates per hadronic event and inclusive cross sections from these corrected signals. In calculating the rate per hadronic event, we make the assumption that our hadronic event selection criteria are unbiased, in the sense the efficiency for detecting a hadronic event which contains a semi-leptonic decay is the same as that for a hadronic event which does not contain such a decay. This assumption has been

P\PT	0.00	0.50	1.00	1.50
1.0	0.80	0.78	0.76	0.76
2.0	0.90	0.88	0.87	0.87
3.0	0.91	0.91	0.90	0.90
4.0	0.91	0.91	0.90	0.90
5.0	0.91	0.91	0.91	0.91
6.0	0.91	0.91	0.91	0.91

Table 6.1: Prompt electron detection efficiency.

P\PT	0.00	0.50	1.00	1.50
2.0	0.78	0.78	0.78	0.78
3.0	0.82	0.82	0.82	0.82
4.0	0.86	0.86	0.86	0.86
5.0	0.90	0.90	0.90	0.90
6.0	0.92	0.92	0.92	0.92

Table 6.2: Prompt muon identification efficiency.

checked using our standard Monte Carlo models. This was done by measuring the hadronic event detection efficiencies for both semi-leptonic and purely hadronic events. The detection efficiencies are the same within a few percent, being slightly lower for the semi-leptonic events due to the decrease in visible energy resulting from the undetected neutrinos. This result is model dependent however. If for example there were semileptonic event topologies which tended to result in final states with very low charged particle multiplicities, then our hadronic event selection criteria would be biased since we demand at least five visible charged tracks.

P\PT	0.0	0.50	1.00	1.50	
1.0	97.3	77.2	26.7	1.5	Signal
	44.9	23.9	11.8	4.2	Stat. Err.
	174.9	55.0	10.7	1.5	Syst. Err.
2.0	56.2	41.4	24.5	15.3	Signal
	20.8	13.8	8.0	6.2	Stat. Err.
	51.2	18.3	4.0	2.5	Syst. Err.
3.0	28.8	30.4	13.4	10.5	Signal
	12.3	9.3	5.6	4.8	Stat. Err.
	16.0	6.7	1.9	1.4	Syst. Err.
4.0	30.3	24.7	12.2	7.2	Signal
	8.5	7.2	4.8	3.8	Stat. Err.
	5.3	3.3	1.2	0.8	Syst. Err.
5.0	4.3	11.9	5.7	10.1	Signal
	4.5	5.0	3.3	4.0	Stat. Err.
	2.5	1.6	0.6	0.8	Syst. Err.
6.0	6.1	8.4	4.2	2.8	Signal
	4.9	4.6	3.0	2.7	Stat. Err.
	2.8	1.8	0.6	0.6	Syst. Err.

Table 6.3: Efficiency corrected prompt electron signal.

P\PT	0.0	0.50	1.00	1.50	
2.0	54.1	60.0	36.0	9.8	Signal
	21.6	19.9	13.7	9.1	Stat. Err.
	18.7	13.5	5.3	2.7	Syst. Err.
3.0	26.2	47.5	21.8	12.4	Signal
	14.3	14.9	9.7	7.6	Stat. Err.
	8.7	7.4	2.9	1.9	Syst. Err.
4.0	39.3	16.7	9.5	2.4	Signal
	12.5	9.3	6.3	4.4	Stat. Err.
	5.6	3.5	1.4	0.9	Syst. Err.
5.0	11.9	8.8	4.6	4.7	Signal
	7.6	6.6	4.6	4.6	Stat. Err.
	2.6	2.0	0.9	0.8	Syst. Err.
6.0	9.2	7.8	3.5	2.8	Signal
	7.5	7.0	4.6	4.7	Stat. Err.
	3.2	2.8	1.1	1.3	Syst. Err.

Table 6.4: Efficiency corrected prompt muon signal.

In the case of unbiased event selection, the prompt lepton rate per produced hadronic event is the same as the rate per detected hadronic event. Thus the inclusive rates can be extracted from Tables 6.3 and 6.4 by summing the corrected signals in the kinematic region of interest and dividing by the total number of detected hadronic events. The corresponding statistical errors are calculated by combining the statistical errors from each bin in quadrature. The systematic errors are assumed to be correlated and the contributions from each bin are simply summed. The corrected number of hadronic events after subtracting expected backgrounds is 10481 ± 104. There is also some systematic uncertainty (≃ ±3%) in the number of true hadronic events in the remaining sample. This introduces a small systematic error which is negligible when added in quadrature with the other systematic errors. The inclusive rates per hadronic event in two different $p,p_\perp$ regions are shown in Table 6.5.

The prompt lepton rate can also be expressed as a cross section σ_{lep} defined as:

$$\sigma_{lep} = r_{lep} \times R \times \sigma_{\mu\mu} \qquad (6.3)$$

where r_{lep} is the prompt lepton rate per hadronic event, R is the ratio $\sigma(e^+e^- \rightarrow \gamma \rightarrow \text{hadrons})/\sigma_{\mu\mu}$, and $\sigma_{\mu\mu}$ is the total cross section for $e^+e^- \rightarrow \gamma \rightarrow \mu^+\mu^-$. The value of R at 29 GeV has been determined [44] to be (3.90 ± .05 ± .25). The value of $\sigma_{\mu\mu}$ at 29 GeV is 103 picobarns (pb). We use these value to obtain a scaling factor of $R\times\sigma_{\mu\mu}$ = (402 ± 26)pb to convert rates per hadronic event into cross sections. The inclusive rates in Table 6.5 are expressed as inclusive cross sections in Table 6.6. The uncertainty in the scaling factor is reflected in the systematic errors.

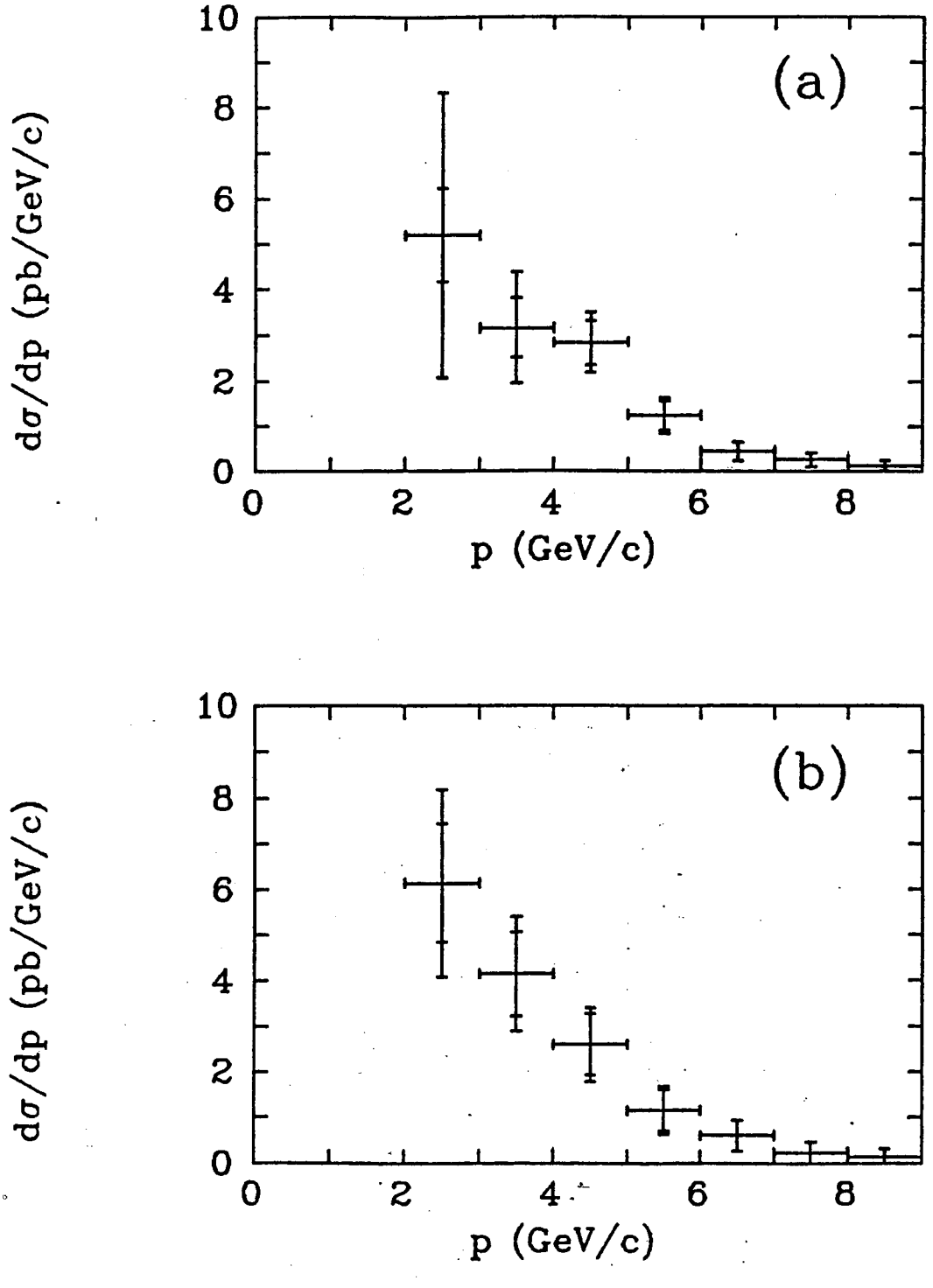

Figure 6.2: Differential total momentum cross sections. (a)Prompt electrons; (b)Prompt muons. Two sets of error bars are shown for each point. The smaller one is the statistical error; the larger one is the statistical and systematic errors added in quadrature.

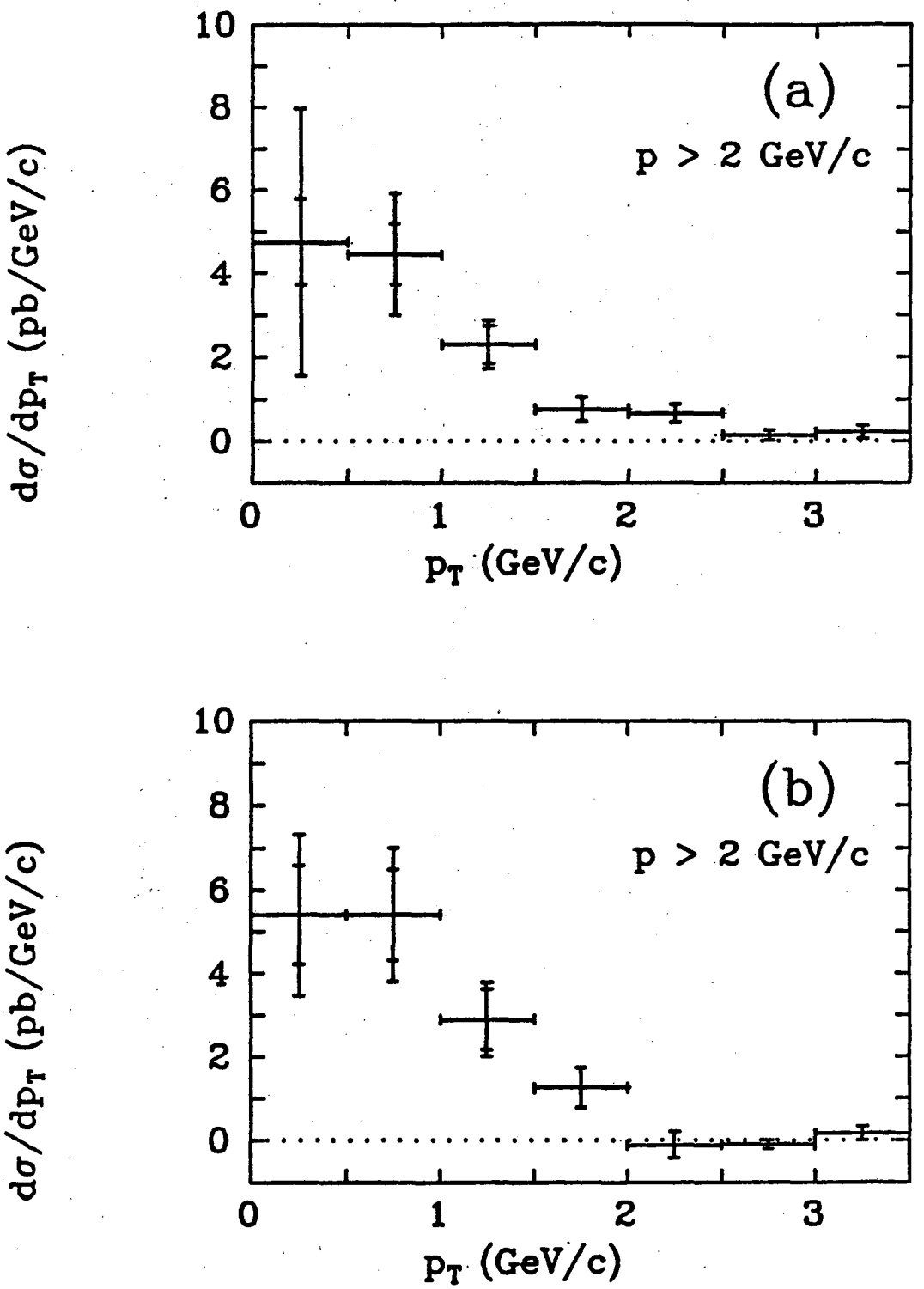

Figure 6.3: Differential transverse momentum cross sections. (a)Prompt electrons; (b)Prompt muons. There is a total momentum cut of p > 2 GeV/c.

We can also obtain differential momentum and transverse momentum cross sections from Tables 6.3 and 6.4. The results of such are shown in Figures 6.2 and 6.3 for prompt leptons with p > 2 GeV/c. In these figures we have extended the momentum and transverse momentum bins out to 8.0 and 3.5 GeV/c (from 6.0 and 1.5 GeV/c) respectively in order to better indicate the shape of the distributions.

Kinematic region	Prompt Electrons	Prompt Muons
$p > 2.0$ $p_\perp > 0.0$	$0.033 \pm 0.003 \pm 0.012$	$0.037 \pm 0.005 \pm 0.008$
$p > 2.0$ $p_\perp > 1.0$	$0.010 \pm 0.001 \pm 0.001$	$0.010 \pm 0.002 \pm 0.002$

Table 6.5: Prompt Lepton rates per hadronic event.
The first error quoted is statistical; the second is systematic.

Kinematic region	Prompt Electrons	Prompt Muons
$p > 2.0$ $p_\perp > 0.0$	$13.3 \pm 1.4 \pm 4.9$	$14.9 \pm 1.8 \pm 3.5$
$p > 2.0$ $p_\perp > 1.0$	$4.1 \pm 0.6 \pm 0.6$	$4.1 \pm 0.9 \pm 0.8$

Table 6.6: Prompt Lepton cross sections.
Cross sections are in picobarns (pb).
The first error quoted is statistical; the second is systematic.

7. PROPERTIES OF HEAVY QUARKS

7.1 Fit to the lepton $p,p_\perp$ spectra

If we assume that the hadronic event sample contains only events arising from the process $e^+e^- \rightarrow q\bar{q} \rightarrow$ hadrons (Figure 1.1), then the possible sources of lepton candidates are:

1) Background from misidentified hadrons
   (electrons - hadron showers and track overlap)
   (muons - hadron punchthrough)
2) Background from non-prompt leptons
   (electrons - unidentified γ conversions and Dalitz decays)
   (muons - π and K decays in flight)
3) Prompt leptons from charm decay in $c\bar{c}$ events (C primary)
4) Prompt leptons from charm decay in $b\bar{b}$ events (C secondary)
5) Prompt leptons from bottom decay in $b\bar{b}$ events (B primary)

The background contributions have been measured and were discussed in Chapters 3 and 4. If we subtract these backgrounds from the observed lepton signal, we are left with the prompt lepton signal. This prompt signal arises from the weak decays of heavy quarks. In order to determine the contributions from each of the processes 3) - 5) we must be able to predict the lepton p and $p_\perp$ distributions arising from each type of weak decay. To accomplish this we must specify a model for the production and semileptonic decay of charm and bottom quarks at 29 GeV in e^+e^- annihilation. This will be done by using a Monte Carlo simulation as described below.

Monte Carlo simulation:

The Monte Carlo simulation uses a Feynman-Field hadronization model [3] with gluon radiation as incorporated by Ali et al.[45]. In the Feynman-Field model, a quark fragments into a meson by combining with an antiquark from a secondary quark-antiquark pair (see Figure 1.2). This process leaves an unpaired secondary quark which can fragment into

another meson in a similar manner. This process is repeated until there is too little energy left to form a new meson. At each step in the process, the unpaired secondary quark is left with a fraction η of the original quark $(E + p_\eta)$. The pair-production of secondary charm and bottom quarks is greatly suppressed relative to light quarks. Thus all produced heavy quarks are taken to be primary quarks (ignoring those that arise from the weak decays of other heavy quarks). This results in a simple relationship between the heavy quark splitting function and fragmentation function, namely:

$$f(\eta) = D_Q^H(1-\eta)$$

In the case of secondary pair production of light quarks the probabilities for producing the various flavors are taken to be $p(u\bar{u})=p(d\bar{d})=0.45$ and $p(s\bar{s})=0.10$. Because of this secondary pair production, the relationship between the splitting function and fragmentation function is more complex for light quarks. In the Monte Carlo model, this light quark splitting function is parameterized as:

$$f(\eta) = 1 - a + 3a\eta^2$$

where we take $a = 1.00$.

For each meson generated in the Monte Carlo there is a choice of particle spin. Our model generates 60% pseudoscalar and 40% vector particles. Once the mesons have been created they are allowed to decay into stable particles via appropriate decay models.

Semileptonic decays in the Monte Carlo:

The momentum and transverse momentum distributions of leptons from semileptonic decays result from a boost of the rest-frame lepton momentum spectrum into the frame of the decaying parent hadron. Thus it

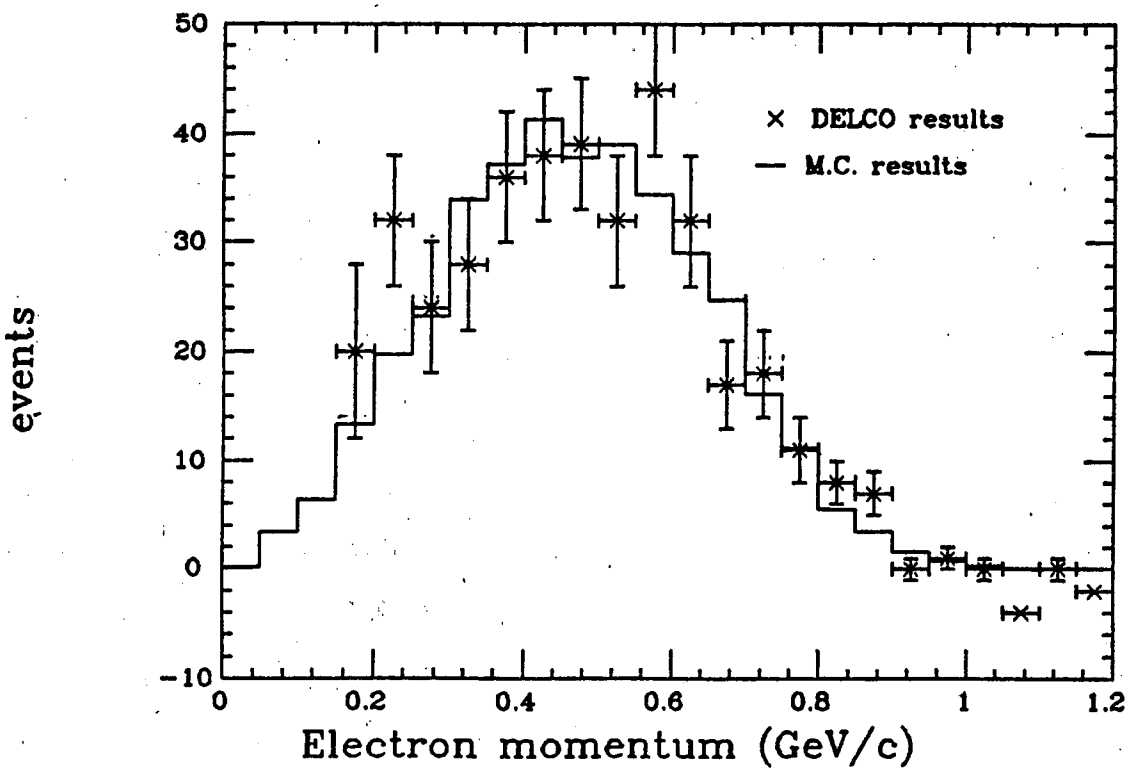

Figure 7.1: Comparison of DELCO data and MARK II Monte Carlo.

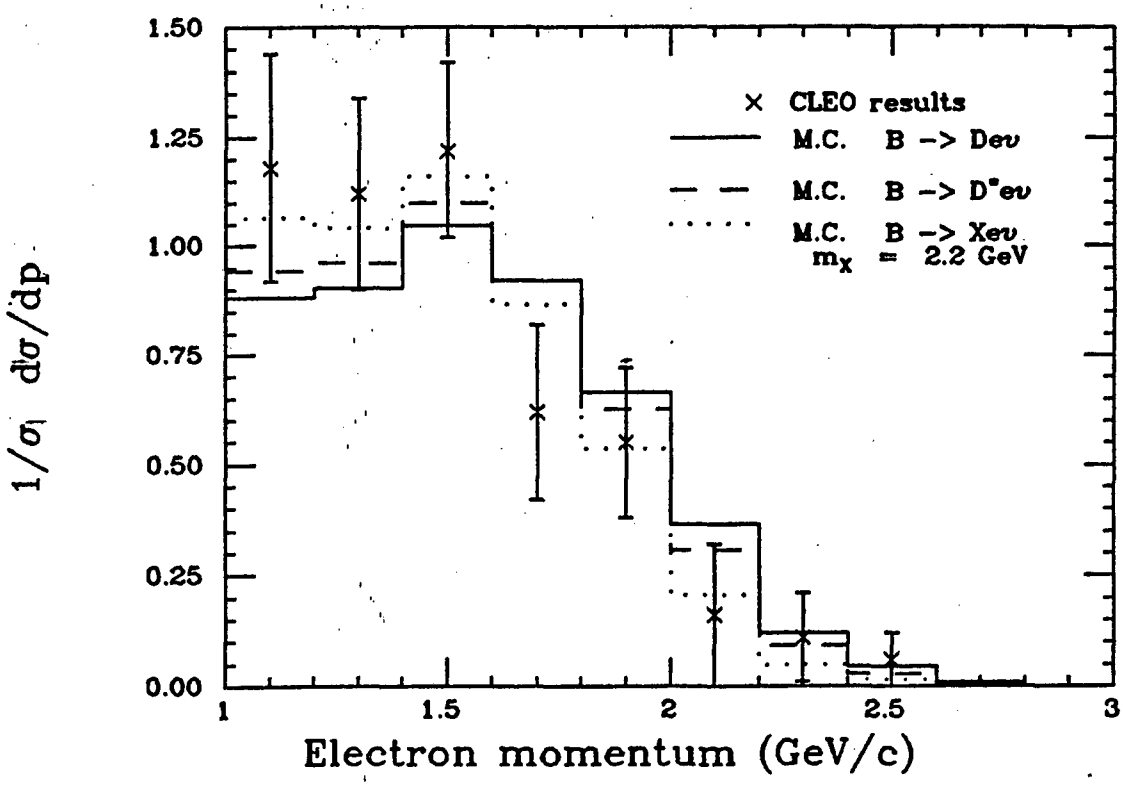

Figure 7.2: Comparison of CLEO data and MARK II Monte Carlo.

is very important for the Monte Carlo correctly reproduce the rest-frame decay spectra of charm and bottom hadrons. The Monte Carlo lepton spectra have been compared with experimental results and adjusted to fit the measured spectra. The electron spectrum from D's has been measured by DELCO at the ψ'' [18]. Figure 7.1 shows a comparison of those results and the results from our Monte Carlo. The Monte Carlo histogram was made by producing pairs of D's at E_{cm}=3.77, simulating the momentum resolution of the DELCO detector, and normalizing the results to the peak of the experimentally observed spectrum. The shapes agree quite well. The electron spectrum from B's has been measured by CLEO at the $\Upsilon(4S)$ [24]. Figure 7.2 shows a comparison of those results and our Monte Carlo. The solid histogram is for $B \rightarrow D\ell\nu$. The dashed line is for $B \rightarrow D^*\ell\nu$ and the dotted line is for $B \rightarrow X\ell\nu$ with $m_X = 2.2$ GeV/c^2. The prediction with $m_X = 2.2$ GeV/c^2 gives the best fit to the data and our Monte Carlo model was modified to produce a charm remnant of that mass.

Parameterization of the fit:

Recall that our model for predicting the observed lepton signal consisted of five components (misidentified hadrons, non-prompt leptons, primary charm decays, secondary charm decays, and bottom decays). Based on this model, we make the following prediction for the expected number of observed lepton candidates N_ℓ in any given $(p,p_\perp)$ bin:

$$N_\ell(p,p_\perp) = N_{pi}(p,p_\perp) + N_{np}(p,p_\perp) +$$
$$+ \epsilon_{fv}(p,p_\perp) \times \epsilon_{id}(p,p_\perp) \times$$
$$[2N(c\bar{c})\times(B_c \sum_j W_c(j)*P_{cpri}(j,p,p_\perp))$$
$$+2N(b\bar{b})\times(B_b \sum_j W_b(j)*P_{bpri}(j,p,p_\perp)+B_c \sum_j W_b(j)*P_{csec}(j,p,p_\perp))]$$

N_{pi} is the background from misidentified pions expected in each $(p,p_\perp)$ bin. These numbers come from Table 3.7 for electrons and Table 5.6 for muons. N_{np} is the background from non-prompt leptons expected in each $(p,p_\perp)$ bin. These numbers come from Table 5.3 for electrons and Table 5.7 for muons.

ϵ_{fv} and ϵ_{id} are the fiducial acceptance and identification efficiencies for prompt leptons as discussed in Section 6.1.

$N(c\bar{c})$ and $N(b\bar{b})$ are the expected number of $c\bar{c}$ and $b\bar{b}$ events in the total hadronic event sample. We assume that quark pairs are produced in e^+e^- annihilation in proportion to the quark charge squared. Thus we expect that roughly 4/11 (36.4%) of the observed hadronic events are from charm quark events and that 1/11 (9.1%) are from bottom quark events. In practice, there are slightly different efficiencies for detecting hadronic events arising from different quark flavors. We use the flavor dependent detection efficiencies derived from our Monte Carlo

to predict ≃ 3840 (36.6%) $c\bar{c}$ and ≃ 1140 (10.9%) $b\bar{b}$ events in the 10481 corrected hadronic events.

B_c and B_b are the semi-leptonic branching ratios for charm and bottom. These will be two of the parameters in the fit.

The weights $W_c(j)$ and $W_b(j)$ specify the shapes of the differential cross sections $d\sigma/dz$ for charm and bottom mesons. In this analysis the kinematically allowed regions of z ($m_Q/E_{beam} \leq z \leq 1.$) is divided into six equally sized regions. The index j (j=1,6) refers to a particular bin in z. This division is made independently for charm and bottom since the lower kinematic limits $z_{min} = m_Q/E_{beam}$ are different. The bins of z indexed by j will therefore be of different size and will have different boundaries for each flavor. For example, j=1 refers to the region z=.128-.273 for charm and .358-.465 for bottom. The differential cross-section for producing a heavy hadron H is taken to be proportional to β times the fragmentation function D(z). Here β is the velocity of the heavy hadron H. The beta factor arises from the kinematical factor β/s in the differential cross section for inclusive hadron production:

$$\frac{d\sigma}{dz} = \frac{2\pi\alpha^2\beta}{s} z \left(2mW_1 + \frac{1}{3}\beta^2 z\nu W_2\right)$$

This factor naturally forces the heavy hadron production cross-section to zero at z_{min}. Recall that the shape of the fragmentation function is taken to be:

$$D_Q^H(z) = \frac{A}{z[1 - 1/z - \epsilon_Q/(1-z)]^2}$$

In order to calculate the weights for the j'th bin of the fragmentation function, the product of β times the fragmentation function D_Q^H is

integrated over the range in z corresponding from the lower to the upper limit of the j'th bin:

$$W_Q(j) = \int_{z_{min}(j)}^{z_{max}(j)} dz\ \beta D_Q^H(z)$$

where Q = c or b.

The parameters ϵ_c and ϵ_b determine the the average value $\langle z \rangle$ for charm and bottom hadrons respectively. In our fit we will fix $\epsilon_c = 0.25$ in accordance with previous measurements of c-quark fragmentation (see Section 1.3). ϵ_b will be left as a free parameter in the fit.

The quantities $P_{cpri}(j,p,p_\perp)$, $P_{bpri}(j,p,p_\perp)$, and $P_{csec}(j,p,p_\perp)$ are the probabilities that the semi-leptonic decay of a heavy hadron (charm primary, charm secondary, or bottom primary) with a z in the j'th bin will produce a lepton in the $(p,p_\perp)$ bin. These probabilities were calculated from the Monte Carlo and are tabulated in Appendix A.

7.2 Fit results

Maximum likelihood fits to the observed electron and muon signals (Tables 5.1 and 5.5) were performed using the prediction discussed in the previous section. The results of these fits are shown in Table 7.1. The detailed results (asymmetric errors, covariance matrices, and correlation coefficients) can be found Tables B.1 and B.2 in Appendix B.

	Electron results	Muon results
B_c	$6.4 \pm 1.3 \pm 2.8$	$8.1 \pm 1.6 \pm 1.8$
B_b	$12.9 \pm 2.5 \pm 2.0$	$12.2 \pm 5.0 \pm 3.0$
ϵ_b	$0.015\ ^{+0.022\ +0.023}_{-0.010\ -0.011}$	$0.043\ ^{+0.202\ +0.120}_{-0.041\ -0.035}$
$\langle z \rangle_b$	$0.79 \pm 0.06 \pm 0.06$	$0.73 \pm 0.15 \pm 0.10$

Table 7.1: Results of the fit
B_c is the average charm semileptonic branching ratio.
B_b " " " bottom " " " .
ϵ_b is the parameter in Eq. (1.1) for bottom quark fragmentation.
$\langle z \rangle_b$ is the average fractional energy of bottom hadrons.

The systematic errors in Table 7.1 reflect our estimates of uncertainties in the overall magnitude and momentum dependence of the hadron misidentification probabilities, the average z of the charm fragmentation function, the rest-frame momentum spectra of leptons from b- and c-quark decays and the primordial $p_\perp$ distributions of bottom and charm hadrons. Tables B.6 - B.12 in Appendix B show the detailed results of some of the fits which were performed in order to estimate

the size of these systematic errors. A systematic check involving a different parameterization of the heavy quark fragmentation function is described in Section 7.5.

7.3 Quality of Fits

Before we can reliably interpret the fit parameters in Table 7.1 as actual properties of charm and bottom quarks, we should check that the lepton spectra predicted by our model are in reasonable agreement with the actual measured spectra. Tables 7.2 and 7.3 show the observed lepton signal and the prediction of the fit procedure in each $(p,p_\perp)$ bin. In order to judge the quality of the fit we have computed a χ^2 contribution for each bin:

$$\chi^2 = (\text{observed-expected})^2/(\text{expected})$$

(Note that the fit itself is maximum likelihood, not minimum χ^2.) We see that the χ^2's are reasonable throughout the $p,p_\perp$ plane indicating that our model provides a good representation of the data. Three of the low $p,p_\perp$ bins in Table 7.2 were excluded from the fit. As one can see, the χ^2 contribution from these bins would have been quite small and the results of a fit which included them would be almost identical. They were excluded from the fit, however, in order to decrease the sensitivity to the systematic uncertainty in the hadron-electron misidentification probability. The overall χ^2/DOF for the two fits are 13.4/18 for electrons and 10.1/17 for muons.

P\PT	0.0	0.50	1.00	1.50	
1.0	363.0	112.0	28.0	3.0	Observed
	376.1	115.6	29.9	3.8	Predicted
	excluded	excluded	0.1255	0.1681	χ^2
2.0	115.0	54.0	21.0	13.0	Observed
	112.0	59.9	20.7	12.5	Predicted
	excluded	0.5872	0.0031	0.0224	χ^2
3.0	46.0	31.0	12.0	9.0	Observed
	46.4	33.1	13.4	10.6	Predicted
	0.0037	0.1342	0.1457	0.2480	χ^2
4.0	29.0	22.0	10.0	6.0	Observed
	19.9	17.0	8.6	6.4	Predicted
	4.1737	1.4697	0.2245	0.0236	χ^2
5.0	7.0	11.0	5.0	8.0	Observed
	10.8	9.8	4.1	4.3	Predicted
	1.3588	0.1443	0.1885	3.1961	χ^2
6.0	9.0	9.0	4.0	3.0	Observed
	11.2	10.9	5.2	3.8	Predicted
	0.4364	0.3245	0.2690	0.1805	χ^2

Table 7.2: Electron fit – Fit prediction vs. Observed signal
The overall χ^2/DOF for this fit is 13.4/18.

P\PT	0.0	0.50	1.00	1.50	
2.0	34.0	31.0	16.0	6.0	Observed
	38.3	31.6	12.9	8.8	Predicted
	0.4921	0.0133	0.7241	0.8836	χ^2
3.0	18.0	23.0	10.0	6.0	Observed
	21.7	20.7	8.0	6.1	Predicted
	0.6307	0.2637	0.5236	0.0015	χ^2
4.0	20.0	10.0	5.0	2.0	Observed
	12.2	11.2	5.3	3.6	Predicted
	4.9400	0.1280	0.0130	0.7350	χ^2
5.0	8.0	6.0	3.0	3.0	Observed
	7.1	7.5	3.0	2.6	Predicted
	0.1094	0.2995	0.0004	0.0758	χ^2
6.0	8.0	7.0	3.0	3.0	Observed
	7.5	8.0	3.6	2.9	Predicted
	0.0380	0.1140	0.1005	0.0010	χ^2

Table 7.3: Muon fit – Fit prediction vs. Observed signal
The overall χ^2/DOF for this fit is 10.1/17.

7.4 Composition of the lepton signal

In the previous section we saw that our model provided a good description of the measured lepton $p,p_\perp$ spectra. We therefore have confidence that the various components of our model correctly describe their respective contributions to the lepton signal. These contributions were listed at the beginning of this chapter. They are 1) misidentified hadrons, 2) Non-prompt leptons, 3) primary charm decays, 4) secondary charm decays, and 5) bottom decays. Tables 7.5 and 7.6 show the bin by bin contributions of each of these sources to the electron and muon signals. The contributions from charm and bottom decays are shown graphically in Figures 7.3 and 7.4. These figures also show the corrected prompt lepton signal, which is well described by the fit. The signal in the low $p_\perp$ region (e.g. Fig. 7.3(a) and 7.4(a)) is dominated by primary charm decays while that in the high $p_\perp$ regions (e.g. Fig. 7.3(c)-(d) and 7.4(c)-(d)) is dominated by bottom.

We can use Tables 7.5 and 7.6 to explicitly calculate the signal and background contributions is such regions. As an example, the compositions of the low $p_\perp$ (c-enriched) and high $p_\perp$ (b-enriched) regions mentioned above are presented in Table 7.4 below.

	$p>2, p_\perp<0.5$ (c-enriched)		$p>2, p_\perp>1.0$ (b-enriched)	
Source	Electrons	Muons	Electrons	Muons
Bkgd(%)	60.2	41.4	20.9	31.8
C_{pri}(%)	28.5	45.9	11.2	13.3
C_{sec}(%)	2.8	3.6	5.6	6.1
B_{pri}(%)	8.5	9.1	62.3	48.9

Table 7.4: Background and heavy quark contributions

P\PT	0.0	0.5	1.0	1.5	
1.00	246.4	57.2	10.4	1.2	misid.
	66.0	12.0	3.0	1.0	non-prompt
	9.6 49.4	9.9 21.0	1.8 1.9	0.1 0.3	C_{sec} C_{pri}
	4.6	15.5	12.8	1.3	B_{pri}
2.00	62.5	21.2	4.3	2.7	misid.
	16.0	6.0	1.0	0.5	non-prompt
	3.6 25.6	4.2 19.4	1.9 2.2	0.5 1.4	C_{sec} C_{pri}
	4.3	9.1	11.4	7.4	B_{pri}
3.00	19.3	8.0	1.8	1.4	misid.
	7.0	2.0	1.0	0.5	non-prompt
	1.1 15.4	1.4 13.8	1.0 2.0	0.6 1.1	C_{sec} C_{pri}
	3.6	7.8	7.5	7.1	B_{pri}
4.00	6.5	3.5	0.9	0.7	misid.
	1.0	1.0	0.5	0.3	non-prompt
	0.5 8.5	0.7 6.1	0.4 1.4	0.2 0.6	C_{sec} C_{pri}
	3.4	5.6	5.4	4.7	B_{pri}
5.00	3.4	1.9	0.6	0.4	misid.
	0.5	0.5	0.3	0.3	non-prompt
	0.2 4.2	0.2 3.2	0.1 0.6	0.2 0.1	C_{sec} C_{pri}
	2.5	4.0	2.7	3.4	B_{pri}
6.00	4.0	2.3	0.6	0.7	misid.
	0.5	0.5	0.3	0.3	non-prompt
	0.1 3.3	0.2 2.7	0.2 0.6	0.0 0.2	C_{sec} C_{pri}
	3.4	5.2	3.6	2.7	B_{pri}

Table 7.5: Electron fit – Contributions to the observed signal.
misid. – Hadron showers and track overlap
non-prompt – Unidentified γ conversions and Dalitz decays
C_{pri} – Prompt leptons from charm decay in $c\bar{c}$ events
C_{sec} – Prompt leptons from charm decay in $b\bar{b}$ events
B_{pri} – Prompt leptons from bottom decay in $b\bar{b}$ events

P\PT	0.0	0.5	1.0	1.5	
2.00	7.2 9.1 2.1 17.6 2.3	4.6 6.7 2.3 13.0 5.0	1.0 3.2 1.3 1.4 6.0	0.6 2.2 0.3 1.5 4.2	misid. non-prompt C_{sec} C_{pri} B_{pri}
3.00	3.4 5.1 0.6 10.8 1.7	2.5 3.4 0.8 10.0 4.0	0.6 1.5 0.7 1.3 3.9	0.5 1.0 0.3 0.8 3.4	misid. non-prompt C_{sec} C_{pri} B_{pri}
4.00	1.9 2.5 0.3 5.9 1.6	1.5 1.9 0.3 4.8 2.7	0.4 0.8 0.3 1.0 2.8	0.4 0.7 0.1 0.2 2.2	misid. non-prompt C_{sec} C_{pri} B_{pri}
5.00	1.2 1.7 0.1 3.1 1.1	0.9 1.3 0.1 3.0 2.1	0.3 0.7 0.1 0.6 1.3	0.3 0.7 0.2 0.0 1.4	misid. non-prompt C_{sec} C_{pri} B_{pri}
6.00	1.9 1.9 0.0 2.4 1.2	1.6 1.8 0.1 2.4 2.0	0.6 0.8 0.2 0.5 1.5	0.7 1.0 0.0 0.2 1.0	misid. non-prompt C_{sec} C_{pri} B_{pri}

Table 7.6: Muon fit – Contributions to the observed signal.
misid. – Hadron punchthrough and track overlap
non-prompt – π and K decays in flight
C_{pri} – Prompt leptons from charm decay in $c\bar{c}$ events
C_{sec} – Prompt leptons from charm decay in $b\bar{b}$ events
B_{pri} – Prompt leptons from bottom decay in $b\bar{b}$ events

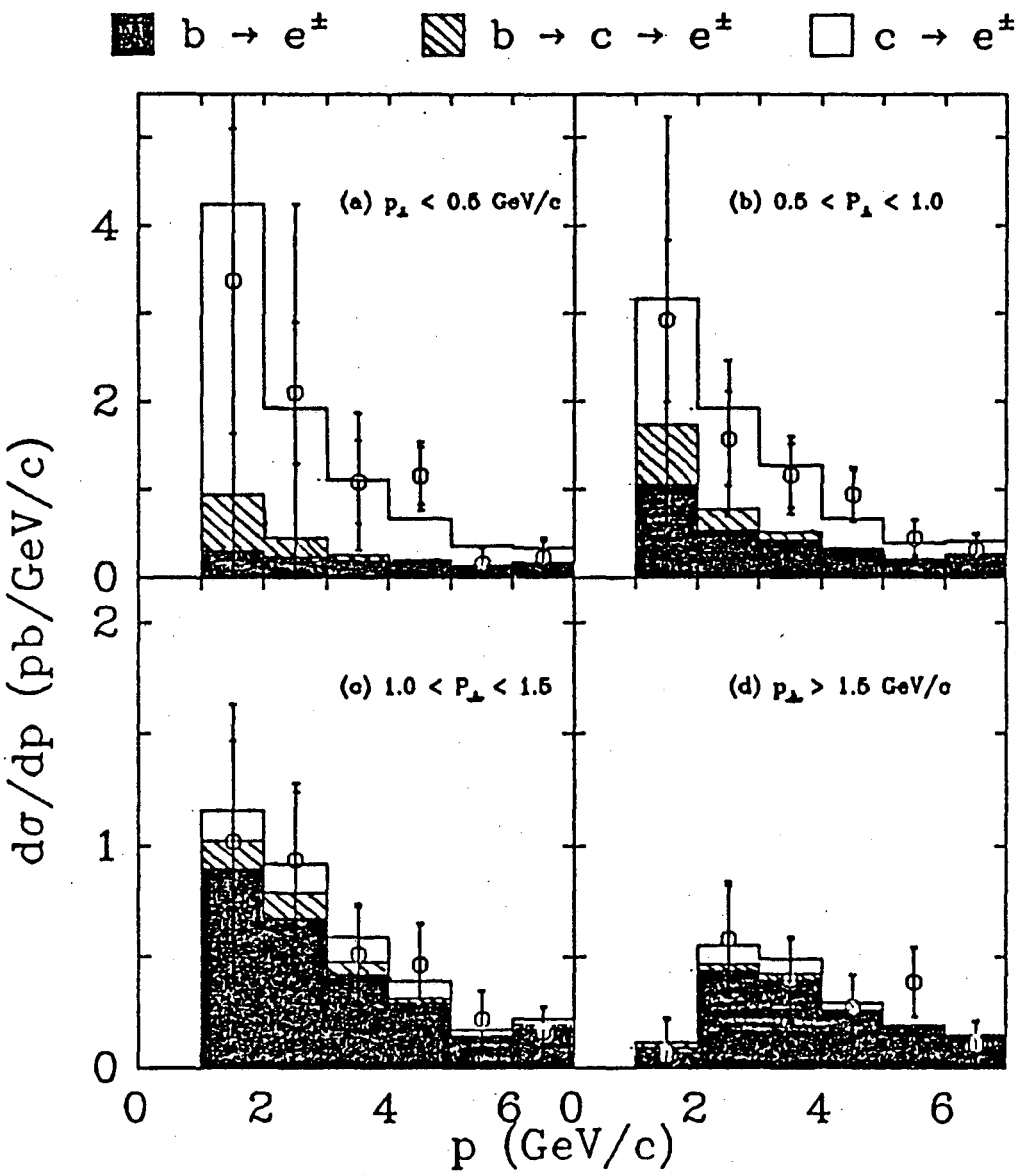

Figure 7.3: Prompt electron momentum spectra. Four regions of transverse momentum $p_\perp$ (GeV/c) are shown: (a) $p_\perp < 0.5$, (b) $0.5 < p_\perp < 1.0$, (c) $1.0 < p_\perp < 1.5$, and (d) $p_\perp > 1.5$. The histograms show the results of the fit.

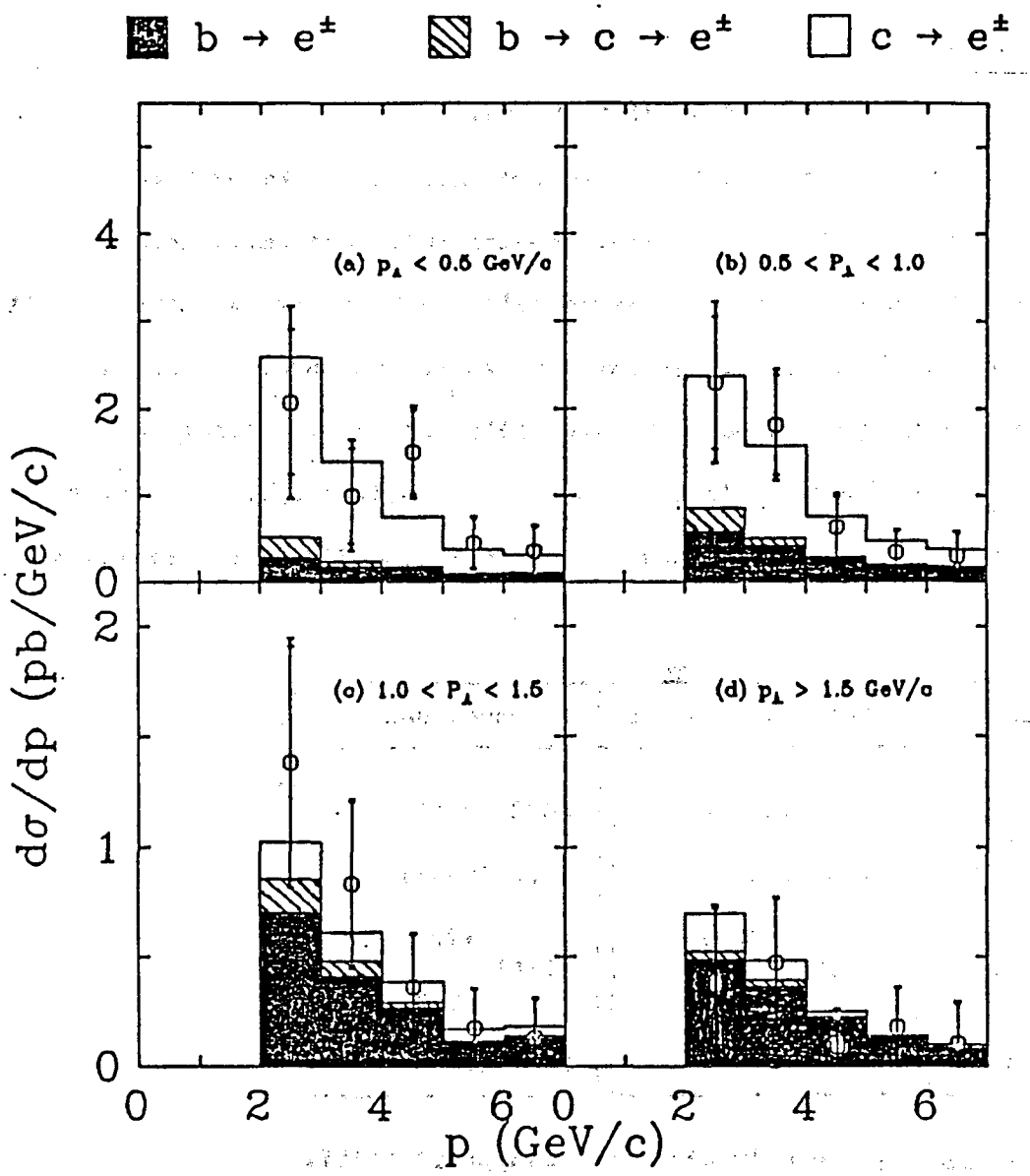

Figure 7.4: Prompt muon momentum spectra. Four regions of transverse momentum $p_\perp$ (GeV/c) are shown: (a) $p_\perp < 0.5$, (b) $0.5 < p_\perp < 1.0$, (c) $1.0 < p_\perp < 1.5$, and (d) $p_\perp > 1.5$. The histograms show the results of the fit.

7.5 Fit using another parameterization of D_Q^H

In order to check the sensitivity of our results to the detailed shape of the fragmentation function, we performed fits in which the following empirical parameterization of the fragmentation function was used:

$$D_Q^H(z) \propto z^{\alpha}(1-z)$$

The charm fragmentation function was taken to have $\alpha_c = 1.5$, which results in $\langle z \rangle_c \simeq .57$, in agreement with previous measurements of charm quark fragmentation. The results of these fits are shown in Table 7.7. The detailed fit results are in Tables B.3 and B.4 in Appendix B. The branching ratios and value for $\langle z \rangle_b$ are in excellent agreement with the nominal results quoted in Table 7.1, indicating that our results are not strongly dependent on the functional form of the fragmentation function.

	Electron results	Muon results
B_c	6.5 ± 1.4	8.3 ± 1.6
B_b	12.8 ± 2.5	12.5 ± 5.1
α_b	$7.29^{+4.45}_{-2.40}$	$3.83^{+7.36}_{-2.82}$
$\langle z \rangle_b$	0.80 ± 0.06	0.72 ± 0.14

Table 7.7: Results of a fit using $D(z) \propto z^{\alpha}(1-z)$

7.6 Conclusions

We have measured the total momentum and transverse momentum spectra for prompt electrons and muons in hadronic events in e^+e^- annihilation at 29 GeV. These spectra were shown in Figures 6.2 and 6.3 The inclusive rate per hadronic event for leptons with total momenta greater than 2 GeV/c was determined to be (0.033 ± 0.003 ± 0.012) for electrons and (0.037 ± 0.005 ± 0.008) for muons. We proceeded to interpret these spectra in terms of the production and decay properties of charm and bottom hadrons. We extracted information on c- and b- quark semileptonic branching ratios and the b-quark fragmentation function based on fits to the electron and muon p, $p_\perp$ spectra. The fit results were shown in Table 7.1 and are reproduced in Table 7.8 below for convenience.

	Electron results	Muon results
B_c	6.4 ± 1.3 ± 2.8	8.1 ± 1.6 ± 1.8
B_b	12.9 ± 2.5 ± 2.0	12.2 ± 5.0 ± 3.0
ϵ_b	$0.015\ ^{+0.022\ +0.023}_{-0.010\ -0.011}$	$0.043\ ^{+0.202\ +0.120}_{-0.041\ -0.035}$
$\langle z\rangle_b$	0.79 ± 0.06 ± 0.06	0.73 ± 0.15 ± 0.10

Table 7.8: Results of the fit
B_c is the average charm semileptonic branching ratio.
B_b " " " bottom " " "
ϵ_b is the parameter in Eq. (1.1) for bottom quark fragmentation.
$\langle z\rangle_b$ is the average fractional energy of bottom hadrons.

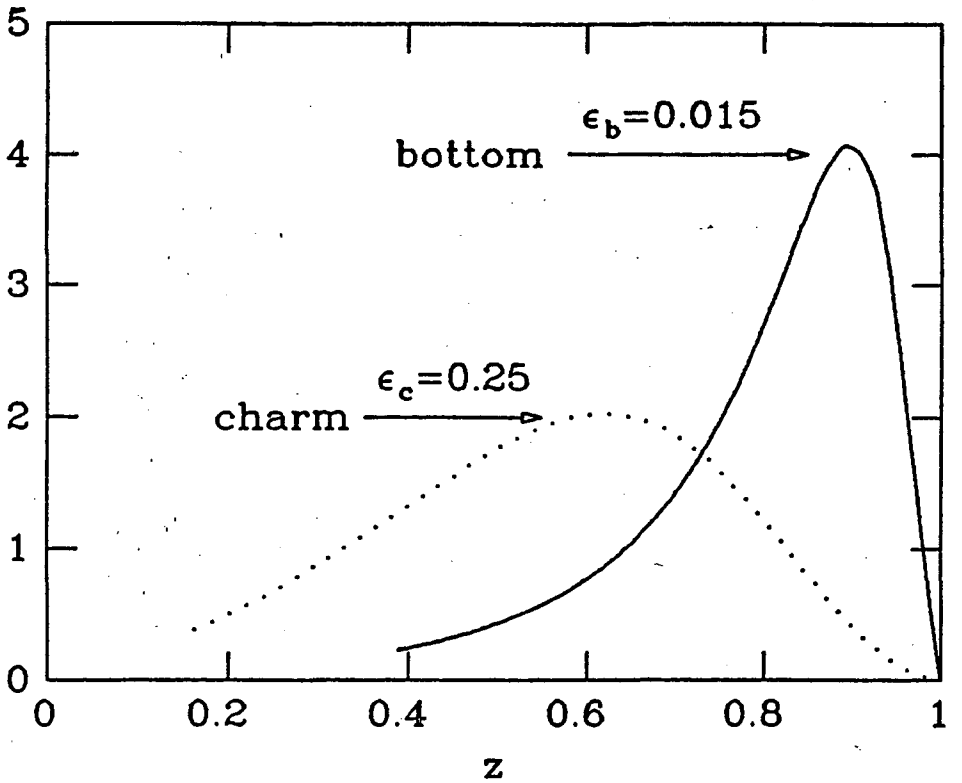

Figure 7.5: Comparison of charm and bottom fragmentation functions.

The values for both the charm and bottom average semileptonic branching ratios agree well with previous measurements (see Table 1.2). These branching ratios represent averages over all types of weakly decaying hadrons weighted by their relative populations. Most of the earlier measurements were made just above threshold (ψ'' for charm and $\Upsilon(4S)$ for bottom) so only the lowest lying mesons contributed to those measurements. Thus the agreement between the previous measurements and those in this analysis indicate that there is no copious production of other charm or bottom hadron types with substantially different semileptonic branching ratios. The measurement of the semileptonic branching ratio of charm into muons had not been done at the lower energies due to the difficulty in identifying the low momentum muons. In this thesis we have measured the charm semileptonic branching ratios for both electrons and muons. We find that they agree within errors, as expected from universality (neglecting phase space factors).

In this thesis we have also obtained the first experimental information on the b quark fragmentation function. Figure 7.5 shows a comparison of the charm and bottom fragmentation functions. We have assumed a parameterization of the heavy quark fragmentation function suggested by Peterson et al. [9]:

$$D_Q^H(z) \propto \frac{1}{z[1 - 1/z - \epsilon_Q/(1-z)]^2}$$

The values of ϵ_b that were obtained in the fits correspond to average values $\langle z \rangle_b$ of $\simeq 0.75$. This result strongly supports the theoretical expectations of a bottom quark fragmentation function which is peaked at large z.

It is interesting to note that in the derivation of the above parameterization (see section 1.3), the parameter ϵ_Q is related to the quark masses by $\epsilon_Q = (m_q/m_Q)^2$, where m_q is is the effective light quark mass in the hadronization process, and m_Q is the effective heavy quark mass. Since we already know that $\epsilon_c \simeq 0.25$ gives a reasonable fit to the charm quark fragmentation [10], we can use the above relationship for ϵ_Q to predict $\epsilon_b \simeq (m_c/m_b)^2 \epsilon_c$. Taking 1.7 GeV/$c^2$ for m_c, 5.0 GeV/c^2 for m_b, and $\epsilon_c = 0.25$, we predict $\epsilon_b \simeq 0.03$, which is reasonable agreement with the fit values shown in Table 7.1.

The fact that this particular model is in reasonable quantitative agreement with the data does not necessarily imply that the details of the model are to be taken too seriously. Other simpler models also give reasonable predictions. In his pioneering paper on the subject of heavy quark fragmentation [5], Bjorken proposed $\langle z \rangle \simeq 1-(1\ \mathrm{GeV}/c^2)/m_Q$, based on simple kinematic arguments. For $m_b = 5.0$ GeV/c^2, this results in a prediction of $\langle z \rangle_b \simeq 0.8$, which is also in reasonable agreement with the fit results of Table 7.1.

In addition to providing useful information on the semileptonic branching ratios and fragmentation properties of heavy quarks, this analysis can serve as a starting point for the investigation of many other properties of heavy quarks. By selecting leptons with large transverse momenta relative to the jet axis, the contributions from bottom quarks can be enhanced (e.g. see Table 7.4). This technique has already been employeed to measure the average lifetime of bottom hadrons [12] and to study the electroweak coupling of the b quark via the production angle asymmetry [46]. In principle, many other properties of

charm and bottom quarks (and someday perhaps the properties of the top quark), can be investigated by utilizing the prompt lepton signal.

Appendix A

Monte Carlo p,$p_\perp$ Distributions

The tables below give the probability that a lepton from a semileptonic decay of a D or B meson will be detected with a given p and $p_\perp$. This probability depends on the z value of the parent hadron. The following procedure was used to construct the tables from the Monte Carlo:

(a) The energy fraction z is defined as the energy of the heavy hadron E_H divided by the energy of the quark E_Q. Both E_H and E_Q are calculated in the e^+e^- center of mass after initial state radiation. In this frame, E_Q is calculated after the radiation of hard gluons (3 and 4 jet events).

(b) Flat heavy quark fragmentation functions (i.e. z=constant) were used as the input to the Monte Carlo.

(c) Events which satisfied the hadronic event selection criteria (see Section 5.1) were selected. This step was performed after a full detector simulation.

(d) A separate count was made of (i) the number of produced prompt leptons from heavy quark decays and (ii) the number of detected prompt leptons within the appropriate fiducial volume. (Part (ii) includes only the fiducial acceptance efficiency and not the identification efficiency of the electron or muon identification algorithm. There is a 100% identification efficiency in the Monte Carlo for tracks within the fiducial volume.)

(e) The momentum p and transverse momentum $p_\perp$ were calculated for each detected lepton. $p_\perp$ is calculated relative to the thrust axis, as in the real data sample.

(f) Each lepton was tabulated by p, $p_\perp$, z of the parent hadron, and origin of parent hadron (c primary, c secondary or b primary).

(g) After all Monte Carlo events had been tabulated, the numbers in each $p,p_\perp$ bin of a given table were divided by the total number of produced semileptonic decays (from step (d) part (i) above) from parent hadrons of the appropriate type and appropriate z.

For secondary charm decays (leptons from D decays arising from B decays), the results are tabulated as a function of the z of the B meson rather than of the parent D meson. This is because the energy distribution of the B mesons determines the energy distribution of the resulting D mesons.

P\PT	0.00	0.50	1.00	1.50
		$.128 < Z_c < .273$		
1.0	0.068	0.065	0.001	0.000
2.0	0.001	0.000	0.000	0.000
3.0	0.000	0.000	0.000	0.000
4.0	0.000	0.000	0.000	0.000
5.0	0.000	0.000	0.000	0.000
6.0	0.000	0.000	0.000	0.001
		$.273 < Z_c < .419$		
1.0	0.126	0.079	0.005	0.000
2.0	0.044	0.030	0.003	0.000
3.0	0.008	0.008	0.001	0.000
4.0	0.002	0.001	0.000	0.000
5.0	0.000	0.000	0.000	0.000
6.0	0.000	0.000	0.000	0.000
		$.419 < Z_c < .564$		
1.0	0.146	0.058	0.008	0.002
2.0	0.056	0.050	0.007	0.002
3.0	0.036	0.031	0.003	0.003
4.0	0.010	0.007	0.002	0.001
5.0	0.002	0.002	0.001	0.000
6.0	0.000	0.001	0.001	0.000
		$.564 < Z_c < .709$		
1.0	0.127	0.050	0.004	0.000
2.0	0.068	0.062	0.007	0.005
3.0	0.044	0.037	0.005	0.003
4.0	0.027	0.021	0.005	0.001
5.0	0.014	0.010	0.002	0.000
6.0	0.005	0.005	0.002	0.000
		$.709 < Z_c < .855$		
1.0	0.119	0.039	0.004	0.001
2.0	0.072	0.042	0.003	0.006
3.0	0.049	0.051	0.010	0.004
4.0	0.035	0.025	0.006	0.004
5.0	0.020	0.017	0.002	0.000
6.0	0.023	0.020	0.001	0.001
		$.855 < Z_c < 1.00$		
1.0	0.120	0.030	0.005	0.000
2.0	0.086	0.037	0.006	0.004
3.0	0.051	0.037	0.006	0.005
4.0	0.047	0.027	0.002	0.002
5.0	0.032	0.017	0.001	0.004
6.0	0.044	0.018	0.006	0.004

Table A.1: Electron $p,p_\perp$ distributions for $c \rightarrow eX$.

P\PT	0.00	0.50	1.00	1.50
		.358 < z_b < .465		
1.0	0.037	0.122	0.135	0.036
2.0	0.018	0.039	0.030	0.037
3.0	0.004	0.006	0.004	0.002
4.0	0.000	0.000	0.000	0.000
5.0	0.000	0.000	0.000	0.000
6.0	0.000	0.000	0.000	0.000
		.465 < z_b < .572		
1.0	0.033	0.097	0.098	0.015
2.0	0.021	0.044	0.055	0.041
3.0	0.007	0.020	0.019	0.015
4.0	0.005	0.006	0.008	0.003
5.0	0.002	0.000	0.000	0.001
6.0	0.000	0.001	0.000	0.001
		.572 < z_b < .679		
1.0	0.021	0.071	0.074	0.009
2.0	0.022	0.038	0.049	0.037
3.0	0.016	0.028	0.025	0.026
4.0	0.009	0.011	0.018	0.012
5.0	0.007	0.006	0.008	0.005
6.0	0.002	0.002	0.001	0.000
		.679 < z_b < .786		
1.0	0.019	0.075	0.062	0.003
2.0	0.018	0.037	0.044	0.029
3.0	0.014	0.028	0.028	0.027
4.0	0.014	0.020	0.018	0.017
5.0	0.008	0.013	0.009	0.010
6.0	0.007	0.010	0.007	0.007
		.786 < z_b < .893		
1.0	0.017	0.062	0.052	0.005
2.0	0.015	0.034	0.044	0.027
3.0	0.013	0.029	0.032	0.027
4.0	0.015	0.026	0.021	0.022
5.0	0.010	0.020	0.008	0.014
6.0	0.013	0.022	0.015	0.009
		.893 < z_b < 1.00		
1.0	0.020	0.060	0.042	0.004
2.0	0.013	0.032	0.043	0.026
3.0	0.015	0.034	0.028	0.030
4.0	0.011	0.022	0.026	0.017
5.0	0.012	0.016	0.017	0.019
6.0	0.024	0.034	0.024	0.021

Table A.2: Electron $p,p_\perp$ distributions for $b \rightarrow eX$.

P\PT	0.00	0.50	1.00	1.50
		.358 < z_b < .465		
1.0	0.024	0.068	0.029	0.002
2.0	0.000	0.005	0.003	0.000
3.0	0.001	0.000	0.000	0.001
4.0	0.000	0.000	0.000	0.000
5.0	0.000	0.000	0.000	0.000
6.0	0.000	0.000	0.000	0.000
		.465 < z_b < .572		
1.0	0.042	0.082	0.026	0.001
2.0	0.009	0.009	0.005	0.001
3.0	0.001	0.003	0.001	0.000
4.0	0.000	0.000	0.000	0.000
5.0	0.000	0.000	0.000	0.000
6.0	0.000	0.000	0.000	0.000
		.572 < z_b < .679		
1.0	0.059	0.068	0.014	0.001
2.0	0.014	0.029	0.015	0.005
3.0	0.004	0.005	0.006	0.002
4.0	0.002	0.002	0.000	0.000
5.0	0.000	0.000	0.000	0.001
6.0	0.000	0.000	0.000	0.000
		.679 < z_b < .786		
1.0	0.080	0.090	0.023	0.001
2.0	0.022	0.023	0.019	0.005
3.0	0.010	0.006	0.003	0.003
4.0	0.001	0.004	0.004	0.001
5.0	0.000	0.001	0.000	0.001
6.0	0.000	0.000	0.001	0.000
		.786 < z_b < .893		
1.0	0.080	0.095	0.017	0.000
2.0	0.029	0.034	0.014	0.004
3.0	0.008	0.013	0.011	0.002
4.0	0.003	0.006	0.004	0.001
5.0	0.004	0.001	0.001	0.003
6.0	0.000	0.003	0.003	0.000
		.893 < z_b < 1.00		
1.0	0.111	0.082	0.009	0.001
2.0	0.040	0.046	0.016	0.003
3.0	0.011	0.016	0.010	0.011
4.0	0.010	0.009	0.002	0.003
5.0	0.000	0.004	0.001	0.000
6.0	0.003	0.002	0.001	0.000

Table A.3: Electron $p,p_\perp$ distributions for $b \rightarrow c \rightarrow eX$.

P\PT	0.00	0.50	1.00	1.50
		.128 < z_c < .273		
1.0	0.000	0.000	0.000	0.000
2.0	0.000	0.000	0.000	0.000
3.0	0.000	0.000	0.000	0.000
4.0	0.000	0.000	0.000	0.000
5.0	0.000	0.000	0.000	0.000
6.0	0.000	0.000	0.000	0.001
		.273 < z_c < .419		
1.0	0.000	0.000	0.000	0.000
2.0	0.025	0.020	0.002	0.000
3.0	0.005	0.007	0.001	0.000
4.0	0.002	0.001	0.000	0.000
5.0	0.000	0.000	0.000	0.000
6.0	0.000	0.000	0.000	0.000
		.419 < z_c < .564		
1.0	0.000	0.000	0.000	0.000
2.0	0.037	0.027	0.004	0.002
3.0	0.025	0.023	0.002	0.002
4.0	0.008	0.005	0.001	0.000
5.0	0.002	0.002	0.001	0.000
6.0	0.000	0.001	0.001	0.000
		.564 < z_c < .709		
1.0	0.000	0.000	0.000	0.000
2.0	0.043	0.037	0.004	0.004
3.0	0.027	0.023	0.001	0.002
4.0	0.013	0.015	0.004	0.000
5.0	0.007	0.008	0.002	0.000
6.0	0.004	0.002	0.001	0.000
		.709 < z_c < .855		
1.0	0.000	0.000	0.000	0.000
2.0	0.043	0.025	0.001	0.007
3.0	0.026	0.025	0.007	0.002
4.0	0.020	0.014	0.002	0.002
5.0	0.012	0.011	0.001	0.000
6.0	0.012	0.015	0.001	0.001
		.855 < z_c < 1.00		
1.0	0.000	0.000	0.000	0.000
2.0	0.052	0.027	0.005	0.001
3.0	0.031	0.030	0.005	0.004
4.0	0.031	0.012	0.000	0.000
5.0	0.019	0.014	0.001	0.002
6.0	0.022	0.013	0.005	0.004

Table A.4: Muon $p,p_\perp$ distributions for $c \rightarrow \mu X$.

P\PT	0.00	0.50	1.00	1.50
		.358 < z_b < .465		
1.0	0.000	0.000	0.000	0.000
2.0	0.011	0.025	0.019	0.022
3.0	0.003	0.003	0.003	0.001
4.0	0.000	0.000	0.000	0.000
5.0	0.000	0.000	0.000	0.000
6.0	0.000	0.000	0.000	0.000
		.465 < z_b < .572		
1.0	0.000	0.000	0.000	0.000
2.0	0.012	0.030	0.032	0.024
3.0	0.005	0.012	0.010	0.010
4.0	0.003	0.002	0.006	0.002
5.0	0.002	0.000	0.000	0.000
6.0	0.000	0.001	0.000	0.000
		.572 < z_b < .679		
1.0	0.000	0.000	0.000	0.000
2.0	0.015	0.025	0.033	0.022
3.0	0.007	0.020	0.015	0.014
4.0	0.005	0.008	0.010	0.007
5.0	0.003	0.003	0.005	0.002
6.0	0.000	0.001	0.001	0.000
		.679 < z_b < .786		
1.0	0.000	0.000	0.000	0.000
2.0	0.011	0.024	0.026	0.019
3.0	0.009	0.017	0.016	0.014
4.0	0.007	0.010	0.013	0.010
5.0	0.003	0.009	0.004	0.006
6.0	0.003	0.006	0.005	0.004
		.786 < z_b < .893		
1.0	0.000	0.000	0.000	0.000
2.0	0.009	0.020	0.026	0.017
3.0	0.007	0.018	0.021	0.018
4.0	0.009	0.017	0.012	0.012
5.0	0.006	0.013	0.006	0.008
6.0	0.008	0.012	0.009	0.004
		.893 < z_b < 1.00		
1.0	0.000	0.000	0.000	0.000
2.0	0.007	0.020	0.028	0.016
3.0	0.008	0.021	0.021	0.019
4.0	0.006	0.014	0.018	0.012
5.0	0.007	0.012	0.011	0.010
6.0	0.014	0.020	0.014	0.015

Table A.5: Muon $p,p_\perp$ distributions for $b \rightarrow \mu X$.

P\PT	0.00	0.50	1.00	1.50
		.358 < z_b < .465		
1.0	0.000	0.000	0.000	0.000
2.0	0.000	0.003	0.001	0.000
3.0	0.000	0.000	0.000	0.001
4.0	0.000	0.000	0.000	0.000
5.0	0.000	0.000	0.000	0.000
6.0	0.000	0.000	0.000	0.000
		.465 < z_b < .572		
1.0	0.000	0.000	0.000	0.000
2.0	0.006	0.006	0.003	0.000
3.0	0.002	0.002	0.001	0.000
4.0	0.000	0.000	0.000	0.000
5.0	0.000	0.000	0.000	0.000
6.0	0.000	0.000	0.000	0.000
		.572 < z_b < .679		
1.0	0.000	0.000	0.000	0.000
2.0	0.009	0.021	0.007	0.002
3.0	0.001	0.005	0.002	0.000
4.0	0.000	0.001	0.000	0.000
5.0	0.000	0.000	0.000	0.000
6.0	0.000	0.000	0.000	0.000
		.679 < z_b < .786		
1.0	0.000	0.000	0.000	0.000
2.0	0.011	0.012	0.014	0.002
3.0	0.006	0.001	0.002	0.002
4.0	0.000	0.001	0.002	0.001
5.0	0.000	0.001	0.000	0.001
6.0	0.000	0.000	0.001	0.000
		.786 < z_b < .893		
1.0	0.000	0.000	0.000	0.000
2.0	0.020	0.017	0.008	0.004
3.0	0.004	0.010	0.008	0.002
4.0	0.003	0.004	0.003	0.002
5.0	0.002	0.001	0.001	0.002
6.0	0.000	0.002	0.002	0.000
		.893 < z_b < 1.00		
1.0	0.000	0.000	0.000	0.000
2.0	0.030	0.027	0.010	0.002
3.0	0.009	0.008	0.008	0.008
4.0	0.007	0.002	0.001	0.000
5.0	0.000	0.002	0.001	0.000
6.0	0.002	0.002	0.001	0.000

Table A.6: Muon $p,p_\perp$ distributions for $b \to c \to \mu X$.

Appendix B

Detailed Results of Fits

RESULTS OF FIT

PARAMETER	VALUE	POSITIVE ERROR	NEGATIVE ERROR
1 $B_e(c)$	6.37×10^{-2}	1.35×10^{-2}	-1.31×10^{-2}
2 $B_e(b)$	1.29×10^{-1}	2.53×10^{-2}	-2.38×10^{-2}
3 ϵ_b	1.46×10^{-2}	2.19×10^{-2}	-1.05×10^{-2}

COVARIANCE MATRIX

	1	2	3
1	1.77×10^{-4}		
2	-1.87×10^{-4}	6.02×10^{-4}	
3	1.99×10^{-6}	1.41×10^{-4}	2.21×10^{-4}

CORRELATION COEFFICIENTS

	1	2	3
1	1.00		
2	-0.57	1.00	
3	0.01	0.39	1.00

Table B.1: Electron fit – nominal results
This fit corresponds to the electron results presented in Table 7.1.
The charm fragmentation parameter ϵ_c was 0.25.
The background from misidentified hadrons was at its nominal value.

RESULTS OF FIT

PARAMETER	VALUE	POSITIVE ERROR	NEGATIVE ERROR
1 $B_\mu(c)$	8.12×10^{-2}	1.63×10^{-2}	-1.57×10^{-2}
2 $B_\mu(b)$	1.22×10^{-1}	5.14×10^{-2}	-4.75×10^{-2}
3 ϵ_b	4.25×10^{-2}	2.02×10^{-2}	-4.00×10^{-2}

COVARIANCE MATRIX

	1	2	3
1	2.55×10^{-4}		
2	-3.67×10^{-4}	2.47×10^{-3}	
3	-3.27×10^{-5}	4.38×10^{-3}	1.71×10^{-2}

CORRELATION COEFFICIENTS

	1	2	3
1	1.00		
2	-0.46	1.00	
3	-0.02	0.67	1.00

Table B.2: Muon fit – nominal results
This fit corresponds to the muon results presented in Table 7.1.
The charm fragmentation parameter ϵ_c was 0.25.
The background from misidentified hadrons was at its nominal value.

RESULTS OF FIT

PARAMETER		VALUE	POSITIVE ERROR	NEGATIVE ERROR
1	$B_e(c)$	6.45×10^{-2}	1.38×10^{-2}	-1.33×10^{-2}
2	$B_e(b)$	1.28×10^{-1}	2.50×10^{-2}	-2.36×10^{-2}
3	α_b	7.29	4.45	-2.40

COVARIANCE MATRIX

	1	2	3
1	1.84×10^{-4}		
2	-1.88×10^{-4}	5.96×10^{-4}	
3	-2.26×10^{-3}	-2.78×10^{-2}	9.67

CORRELATION COEFFICIENTS

	1	2	3
1	1.00		
2	-0.57	1.00	
3	-0.05	-0.37	1.00

Table B.3: Electron fit - systematic check - $z^{\alpha}(1-z)$ parameterization
This fit uses a $z^{\alpha}(1-z)$ parameterization, rather than the form of Peterson et al..
The charm fragmentation parameter α_c was 1.50.
The background from misidentified hadrons was at its nominal value.

RESULTS OF FIT

PARAMETER		VALUE	POSITIVE ERROR	NEGATIVE ERROR
1	$B_\mu(c)$	8.32×10^{-2}	1.65×10^{-2}	-1.59×10^{-2}
2	$B_\mu(b)$	1.25×10^{-1}	5.40×10^{-2}	-4.79×10^{-2}
3	ϵ_b	3.83	7.36	−2.82

COVARIANCE MATRIX

	1	2	3
1	2.62×10^{-4}		
2	-3.61×10^{-4}	2.58×10^{-3}	
3	-1.62×10^{-3}	-1.25×10^{-1}	1.37×10^{1}

CORRELATION COEFFICIENTS

	1	2	3
1	1.00		
2	−0.44	1.00	
3	−0.03	−0.67	1.00

Table B.4: Muon fit − systematic check − $z^\alpha(1-z)$ parameterization
This fit uses a $z^\alpha(1-z)$ parameterization, rather than the form of Peterson et al..
The charm fragmentation parameter α_c was 1.50.
The background from misidentified hadrons was at its nominal value.

RESULTS OF FIT

PARAMETER		VALUE	POSITIVE ERROR	NEGATIVE ERROR
1	$B_e(c)$	4.01×10^{-2}	1.35×10^{-2}	-1.31×10^{-2}
2	$B_e(b)$	1.21×10^{-1}	2.53×10^{-2}	-2.38×10^{-2}
3	ϵ_b	1.06×10^{-2}	1.79×10^{-2}	-8.03×10^{-3}

COVARIANCE MATRIX

	1	2	3
1	1.77×10^{-4}		
2	-1.96×10^{-4}	6.04×10^{-4}	
3	-1.17×10^{-5}	1.25×10^{-4}	1.43×10^{-4}

CORRELATION COEFFICIENTS

	1	2	3
1	1.00		
2	-0.60	1.00	
3	-0.07	0.42	1.00

Table B.5: Electron fit – systematic check – 50% more pion background
This fit tests the sensitivity of the results to the systematic uncertainties in the hadron misidentification probabilities.
The charm fragmentation parameter ϵ_c was 0.25.
The background from misidentified hadrons was assumed to be 50% larger than its nominal value.

RESULTS OF FIT

PARAMETER	VALUE	POSITIVE ERROR	NEGATIVE ERROR
1 $B_\mu(c)$	6.88×10^{-2}	1.65×10^{-2}	-1.59×10^{-2}
2 $B_\mu(b)$	1.26×10^{-1}	5.09×10^{-2}	-4.71×10^{-2}
3 ϵ_b	6.60×10^{-2}	2.90×10^{-2}	-5.00×10^{-2}

COVARIANCE MATRIX

	1	2	3
1	2.59×10^{-4}		
2	-3.82×10^{-4}	2.38×10^{-3}	
3	-2.52×10^{-6}	3.69×10^{-3}	1.52×10^{-2}

CORRELATION COEFFICIENTS

	1	2	3
1	1.00		
2	-0.49	1.00	
3	-0.00	0.61	1.00

Table B.6: Muon fit – systematic check – 50% more pion background
This fit tests the sensitivity of the results to the systematic uncertainties in the hadron misidentification probabilities.
The charm fragmentation parameter ϵ_c was 0.25.
The background from misidentified hadrons was assumed to be 50% larger than its nominal value.

RESULTS OF FIT

PARAMETER	VALUE	POSITIVE ERROR	NEGATIVE ERROR
1 $B_e(c)$	8.84×10^{-2}	1.36×10^{-2}	-1.32×10^{-2}
2 $B_e(b)$	1.38×10^{-1}	2.51×10^{-2}	-2.37×10^{-2}
3 ϵ_b	2.14×10^{-2}	2.76×10^{-2}	-1.34×10^{-2}

COVARIANCE MATRIX

	1	2	3
1	1.80×10^{-4}		
2	-1.82×10^{-4}	5.95×10^{-4}	
3	1.94×10^{-5}	1.58×10^{-4}	3.71×10^{-4}

CORRELATION COEFFICIENTS

	1	2	3
1	1.00		
2	−0.56	1.00	
3	0.08	0.34	1.00

Table B.7: Electron fit − systematic check − 50% less pion background
This fit tests the sensitivity of the results to the systematic uncertainties in the hadron misidentification probabilities.
The charm fragmentation parameter ϵ_c was 0.25.
The background from misidentified hadrons was assumed to be 50% smaller than its nominal value.

RESULTS OF FIT

PARAMETER		VALUE	POSITIVE ERROR	NEGATIVE ERROR
1	$B_\mu(c)$	9.35×10^{-2}	1.60×10^{-2}	-1.54×10^{-2}
2	$B_\mu(b)$	1.17×10^{-1}	5.22×10^{-2}	-4.64×10^{-2}
3	ϵ_b	2.37×10^{-2}	1.29×10^{-2}	-2.27×10^{-2}

COVARIANCE MATRIX

	1	2	3
1	2.52×10^{-4}		
2	-3.39×10^{-4}	2.54×10^{-3}	
3	-1.45×10^{-5}	3.28×10^{-3}	7.89×10^{-3}

CORRELATION COEFFICIENTS

	1	2	3
1	1.00		
2	-0.42	1.00	
3	-0.01	0.73	1.00

Table B.8: Muon fit – systematic check – 50% less pion background
This fit tests the sensitivity of the results to the systematic uncertainties in the hadron misidentification probabilities.
The charm fragmentation parameter ϵ_c was 0.25.
The background from misidentified hadrons was assumed to be 50% smaller than its nominal value.

RESULTS OF FIT

PARAMETER		VALUE	POSITIVE ERROR	NEGATIVE ERROR
1	$B_e(c)$	5.40×10^{-2}	1.15×10^{-2}	-1.11×10^{-2}
2	$B_e(b)$	1.31×10^{-1}	2.51×10^{-2}	-2.37×10^{-2}
3	ϵ_b	1.94×10^{-2}	2.81×10^{-2}	-1.34×10^{-2}

COVARIANCE MATRIX

	1	2	3
1	1.27×10^{-4}		
2	-1.56×10^{-4}	5.98×10^{-4}	
3	2894×10^{-5}	1.59×10^{-4}	3.62×10^{-4}

CORRELATION COEFFICIENTS

	1	2	3
1	1.00		
2	−0.56	1.00	
3	0.06	0.34	1.00

Table B.9: Electron fit − systematic check − harder charm fragmentation
This fit tests the sensitivity of the results to the systematic uncertainties in the charm fragmentation function.
The charm fragmentation parameter ϵ_c was 0.10.
The background from misidentified hadrons was at its nominal value.

RESULTS OF FIT

PARAMETER	VALUE	POSITIVE ERROR	NEGATIVE ERROR
1 $B_\mu(c)$	7.12×10^{-2}	1.43×10^{-2}	-1.53×10^{-2}
2 $B_\mu(b)$	1.34×10^{-1}	5.06×10^{-2}	-4.72×10^{-2}
3 ϵ_b	9.81×10^{-2}	4.17×10^{-2}	-8.00×10^{-2}

COVARIANCE MATRIX

	1	2	3
1	1.97×10^{-4}		
2	-3.16×10^{-4}	2.36×10^{-3}	
3	-1.57×10^{-4}	4.62×10^{-3}	2.76×10^{-2}

CORRELATION COEFFICIENTS

	1	2	3
1	1.00		
2	-0.46	1.00	
3	-0.07	0.57	1.00

Table B.10: Muon fit – systematic check – harder charm fragmentation
This fit tests the sensitivity of the results to the systematic uncertainties in the charm fragmentation function.
The charm fragmentation parameter ϵ_c was 0.10.
The background from misidentified hadrons was at its nominal value.

RESULTS OF FIT

PARAMETER	VALUE	POSITIVE ERROR	NEGATIVE ERROR
1 $B_e(c)$	7.32×10^{-2}	1.58×10^{-2}	-1.53×10^{-2}
2 $B_e(b)$	1.29×10^{-1}	2.54×10^{-2}	-2.39×10^{-2}
3 ϵ_b	1.19×10^{-2}	1.82×10^{-2}	-8.74×10^{-3}

COVARIANCE MATRIX

	1	2	3
1	2.41×10^{-4}		
2	-2.24×10^{-4}	6.10×10^{-4}	
3	-7.96×10^{-6}	1.29×10^{-4}	1.55×10^{-4}

CORRELATION COEFFICIENTS

	1	2	3
1	1.00		
2	-0.58	1.00	
3	-0.04	0.42	1.00

Table B.11: Electron fit – systematic check – softer charm fragmentation
This fit tests the sensitivity of the results to the systematic uncertainties in the charm fragmentation function.
The charm fragmentation parameter ϵ_c was 0.50.
The background from misidentified hadrons was at its nominal value.

RESULTS OF FIT

PARAMETER	VALUE	POSITIVE ERROR	NEGATIVE ERROR
1 $B_\mu(c)$	9.14×10^{-2}	1.82×10^{-2}	-1.76×10^{-2}
2 $B_\mu(b)$	1.16×10^{-1}	5.14×10^{-2}	-4.45×10^{-2}
3 ϵ_b	2.27×10^{-2}	1.15×10^{-1}	-2.10×10^{-2}

COVARIANCE MATRIX

	1	2	3
1	3.22×10^{-4}		
2	-4.15×10^{-4}	2.36×10^{-3}	
3	-1.06×10^{-4}	2.64×10^{-3}	5.89×10^{-3}

CORRELATION COEFFICIENTS

	1	2	3
1	1.00		
2	-0.48	1.00	
3	-0.08	0.71	1.00

Table B.12: Muon fit – systematic check – softer charm fragmentation
This fit tests the sensitivity of the results to the systematic uncertainties in the charm fragmentation function.
The charm fragmentation parameter ϵ_c was 0.50.
The background from misidentified hadrons was at its nominal value.

REFERENCES

1. J. J. Aubert et al., Phys. Rev. Lett., 33, 1404 (1974);
   J. E. Augustin et al., Phys. Rev. Lett., 33, 1406 (1974).
2. S. Herb et al., Phys. Rev. Lett., 39, 252 (1977).
3. R. D. Field and R. P. Feynman, Nucl. Phys. B136, 1 (1978).
4. A. Casher, H. Neuberger, and S. Nussinov, Phys. Rev. D20, 179 (1979).
5. J. D. Bjorken, Phys. Rev. D17, 171 (1978);
   M. Suzuki, Phys. Lett. 71B, 139 (1977).
6. J. M. Yelton et al., Phys. Rev. Lett. 49, 430 (1982).
7. N. Abramowicz et al., Z. Phys. C15, 19 (1982).
8. W. B. Atwood, SLAC-PUB-2980, (1982).
9. C. Peterson et al., Phys. Rev. D27, 105 (1983).
10. D. Schlatter, SLAC-PUB-2982, 1982 (unpublished).
11. K. Kleinknecht and B. Renk, Z. Phys. C17, 325 (1983).
12. For a review of charm particle lifetimes see G. Kalmus, Rapporteurs's talk at XXI International Conference on HEP, Paris, July 1982. Recent results on bottom particle lifetimes are: N. Lockyer et al., SLAC-PUB-3165, Submitted to Phys. Rev. Lett. 1983; and E. Fernandez et al., SLAC-PUB-3154, Submitted to Phys. Rev. Lett. 1983.
13. S. Weinberg, Phys. Rev. Lett. 19, 1264 (1967) ;
    A. Salam, Elementary Particle Theory, edited by N. Svartholm, p. 367 (1968).
14. M. Kobayashi and T. Maskawa, Prog. Theor. Phys. 49, 652 (1973).
15. S. L. Glashow, J. Iliopoulos and L. Maiani, Phys. Rev. D2, 1285 (1970).

16. C. Bebek et al., Phys. Rev. Lett. 46, 84 (1981)
K. Chadwick et al., Phys. Rev. Lett. 46, 88 (1981).

17. R. H. Schindler et al., Phys. Rev. D24, 78 (1981).

18. W. Bacino et al., Phys. Rev. Lett. 43, 1073 (1979).

19. J. M. Feller et al., Phys. Rev. Lett. 40, 274 (1978).

20. R. Brandelik et al., Phys. Lett. 70B, 387 (1977).

21. J. M. Feller et al., Phys. Rev. Lett. 40, 1677 (1978).

22. W. Bacino et al., Phys. Rev. Lett. 45, 329 (1980).

23. E. Vella et al., Phys. Rev. Lett. 48, 1515 (1982).

24. K. Chadwick et al., Phys. Rev. D27, 475 (1983).

25. L. J. Spencer et al., Phys. Rev. Lett. 47, 771 (1981).

26. J. P. Leveille, University of Michigan Report No. UMHE 81-18, 1981 (unpublished).

27. N. Cabibbo and L. Maiani, Phys. Lett. 79B, 109 (1978)
N. Cabibbo, G. Corbo, and L. Maiani, Nucl. Phys. B155, 93 (1979).

28. M. K. Gaillard and B. W. Lee, Phys. Rev. Lett. 33, 108 (1974) ;
G. Altarelli and L. Maiani, Phys Lett. 52B, 351 (1974).

29. V. Barger et al., Phys. Rev. D16, 746 (1978).

30. A. Ali, Z. Phys. C1, 25 (1979).

31. M. J. Puhala et al., Phys. Rev. D25, 695 (1982).

32. G. S. Abrams et al., IEEE Trans. Nucl. Sci., NS-25, 309, (1978);
G. S. Abrams et al., IEEE Trans. Nucl. Sci., NS-27, 59, (1980).

33. K. G. Hayes, SLAC-237, 1981, Ph.D. Thesis (unpublished).

34. T. Himel, SLAC-223, (1979), Ph.D. Thesis (unpublished).
H. Brafman et al., IEEE Trans. Nuclear Science, NS-25, 692, (1978).

35. F. A. Harris, et al., Nucl. Instr. and Meth. 103, 345 (1972).

36. R. M. Sternheimer, Rev. Sci. Instr. 25, 1070 (1954).

37. B. Rossi, High Energy Particles (Prentice - Hall, Englewood Cliffs, N.J., 1961).

38. R. M. Sternheimer, Phys. ReV. 117, 485 (1960).

39. A. Boyarski, SLAC-PUB-559 (1969).

40. M. J. Longo and B. J. Moyer, Phys. Rev. 125, 701 (1961).

41. M. Althoff et al., Z. Phys. C17, 5 (1983).

42. C. A. Blocker et al., Phys. Rev. Lett. 49, 1369 (1982).

43. J. A. M. Vermaseren, J. Smith, and G. Grammer, Jr., Phys. Rev. D19, 137 (1979)

J. Smith, J. A. M. Vermaseren, and G. Grammer, Jr., Phys. Rev. D15, 3280 (1977)

R. Bhattacharya, J. Smith, and G. Grammer, Jr., Phys. Rev. D15, 3267 (1977).

44. J.F. Patrick, LBL - 14585, (1982) Ph.D. Thesis (unpublished).

45. A. Ali et al., Phys. Lett. 93B, 155 (1980).

46. B. Naroska, presented at International Symposium on Lepton and Photon Interactions at High Energies, Ithaca, NY, 1983.

TECHNICAL INFORMATION DEPARTMENT
LAWRENCE BERKELEY LABORATORY
UNIVERSITY OF CALIFORNIA
BERKELEY, CALIFORNIA 94720